Warming does not delay the start of autumnal leaf coloration but slows its progress rate

Warming does not delay the start of autumnal leaf coloration but slows its progress rate

Running title: Leaf coloration onset insensitive to warming

ABSTRACT

Aim: Initiation of autumnal leaf senescence is critical for plant overwintering and ecosystem dynamics. Previous studies focused on the advanced stages of autumnal leaf senescence and reported that climatic warming delayed senescence, despite the fundamental differences among the stages of senescence. However, the timing of onset of leaf coloration (D_{LCO}), the earliest visual sign of senescence, has been rarely studied. Here, we assessed the response of D_{LCO} to temperature.

Location: 30–75°N in the Northern Hemisphere.

Time period: 2000–2018.

Major taxa studied: Deciduous vegetation.

Methods: We retrieved D_{LCO} from high temporal-resolution satellite data, which was then validated by PhenoCam observations, and investigated the temporal changes in D_{LCO} and the relationship between D_{LCO} and temperature by using satellite and ground observations.

Results: D_{LCO} was not significantly ($P > 0.05$) delayed between 2000 and 2018 in 94% of the area. D_{LCO} was positively ($P < 0.05$) correlated with pre-D_{LCO} mean daily minimum temperature (T_{min}) in only 9% of the area, whereas the end of leaf coloration (D_{LCE}) was positively correlated with pre-D_{LCE} mean T_{min} over a larger area (34%). Further analyses showed that warming slowed the progress of leaf coloration. Interestingly, D_{LCO} was less responsive to pre-D_{LCO} mean T_{min} in areas where daylength was longer across the Northern Hemisphere, particularly for woody vegetation.

Main conclusions: The coloration progress rate is more sensitive than its start date to temperature, resulting in an extension of the duration of leaf senescence under warming. The dependence of D_{LCO} response to temperature on daylength indicates stronger photoperiodic control on initiation of leaf senescence in areas with longer daylength (i.e., shorter nights), possibly because plants respond to the length of uninterrupted darkness rather than daylength. This study indicates that

the leaf coloration onset was not responsive to climate warming and provides observational evidence of photoperiod control of autumnal leaf senescence at biome and continental scales.

Keywords: autumnal leaf senescence, global warming, leaf coloration onset, Northern Hemisphere, photoperiod

1 | INTRODUCTION

In contrast to the leaves of evergreen conifers, those of northern deciduous plants are not sufficiently tolerant of freezing to survive cold periods and, therefore, are shed before the onset of winter. This autumnal senescence process is controlled by changes in gene expression and metabolic adjustments that include the degradation of macromolecules (e.g., chlorophyll), a decrease in photosynthesis, and, importantly, the recycling and reallocation of nutrients (Gan & Amasino, 1997; Thomas & Stoddart, 1980). In parallel to leaf senescence, carbon sink activity ceases progressively, and plants switch to nutrient recovery and resorption processes (Estiarte & Peñuelas, 2015; Keskitalo, Bergquist, Gardeström, & Jansson, 2005). Without timely leaf senescence and abscission, early frost would reduce nutrient resorption, leading to a loss of leaf resources. Changes in the timing of key steps of leaf senescence extensively influence ecosystem structure and functions such as vegetation activity, trophic interaction, carbon and nutrient cycling, land-atmosphere moisture, and energy fluxes (Keenan et al., 2014; Morisette et al., 2009), which could further affect the climate system (Peñuelas, Rutishauser, & Filella, 2009; Richardson et al., 2013).

Senescence starts as a cryptic phenological process before any visible symptoms become apparent (Körner & Basler, 2010). The timing of the start of the leaf coloration following senescence varies, depending on the rate of the senescence process, which is related to environmental conditions (e.g., temperature) (Fracheboud et al., 2009). Hence, the process of autumnal leaf senescence has two phases (Fig. 1a): (1) a visually indistinguishable ontogenetic stage that precedes (2) a visible change in leaf color (Tang et al., 2016). The timings of the middle and end of leaf coloration are the focus of *in situ* phenological observations and have been the main concern of most autumnal phenological studies to date.

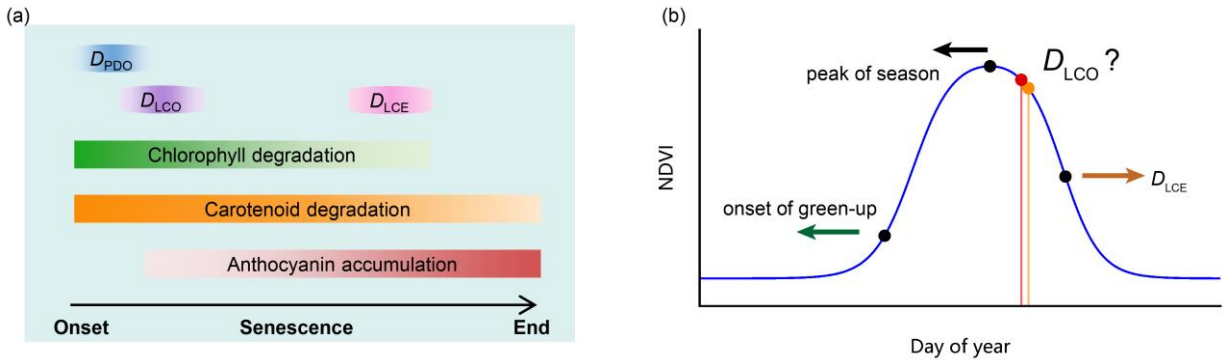

Fig. 1 Conceptual graphs illustrating (a) the developmental processes in pigments during leaf senescence that are related to photosynthetic capacity and leaf color; and (b) phenological changes retrieved from normalized difference vegetation index (NDVI) in the last few decades. In (a), D_{PDO} and D_{LCO} are the timings of the onsets of the decrease in maximum canopy photosynthetic capacity and leaf coloration in autumn, respectively; D_{LCE} is the timing of the end of leaf coloration. In (b), the onset of green-up corresponds to a 20% increase in NDVI in spring, the peak of the season corresponds to the maximum NDVI, and D_{LCE} corresponds to a 50% decrease in NDVI in autumn. D_{LCO} was defined by two methods, corresponding to a 10% decrease in NDVI (orange point) and the inflection point at which NDVI begins to decline (red point), respectively (See materials and methods for details). The leftward and rightward arrows indicate advances of onset of green-up and peak of season and delay of D_{LCE}, respectively, over the past few decades. The question mark indicates a research gap regarding temporal changes in D_{LCO} and their drivers.

Satellite and ground-based observations indicate that climate warming in the last several decades has substantially advanced the onset of spring green-up and the peak of the growing season, and it has slightly delayed the timing of the end of leaf coloration (D_{LCE}, the time when the normalized difference vegetation index [NDVI] decreases by 50% of its annual amplitude in the second half of a year in satellite-based studies (Ganguly, Friedl, Tan, Zhang, & Verma, 2010; Lukasová, Bucha, Škvareninová, & Škvarenina, 2019; Melaas, Friedl, & Zhu, 2013; Nagai, Nasahara, Muraoka, Akiyama, & Tsuchida, 2010; White, Thornton, & Running, 1997; Yu, Luedeling, & Xu, 2010)) in the Northern Hemisphere (Fig. 1b) (Fu et al., 2019; Fu et al., 2015;

Gill et al., 2015; Jeganathan, Dash, & Atkinson, 2014; Menzel et al., 2020; Xu, Liu, Williams, Yin, & Wu, 2016). In addition to temperature, an increase in precipitation also delays D_{LCE} in temperate dry grasslands in the northern middle latitudes (Liu et al., 2016). Besides these abiotic factors, temporal changes in D_{LCE} are also associated with the onset of green-up in some temperate tree species (Keenan & Richardson, 2015) and in boreal ecosystems (Liu et al., 2016). In contrast to D_{LCE}, the timing of onset of leaf coloration (D_{LCO}; Fig. 1b) has been inadequately studied. In particular, it is not known whether D_{LCO} is sensitive to climate and whether it has been responsive to recent climate change. D_{LCO} is of key importance because it indicates when leaf senescence becomes detectable from NDVI and its progress accelerates (Fig. 1b). As shown by experiments on young trees, some temperate and boreal woody species use the shortening of the photoperiod as a signal for the onset of leaf senescence (Table S1), but many *in situ* and satellite observations indicate that increased temperature induces delays in the advanced stages of senescence such as D_{LCE} (Delpierre et al., 2009; Estrella & Menzel, 2006; Ge, Wang, Rutishauser, & Dai, 2015; Gill et al., 2015; Jeong, Ho, Gim, & Brown, 2011; Liu et al., 2016).

A dominant photoperiodic control of early senescence implies that D_{LCO} should not be delayed, even if the temperature increases, because its timing is controlled only by daylength (Hypothesis 1). Moreover, because D_{LCE} delays with warmer temperature, we may further hypothesize that earlier stages of leaf senescence are less sensitive to temperature than are more advanced stages and expect an extension of the period between D_{LCE} and D_{LCO} under warming. On the other hand, without photoperiodic control, shifts in D_{LCO} are expected in the case of climatic warming (Hypothesis 2). Alternatively, if D_{LCO} is influenced by both photoperiod and temperature, the relationships between D_{LCO} and temperature should vary among different areas because the strength of the photoperiod signal varies (Hypothesis 3).

To test these hypotheses, we first investigated the temporal changes in D_{LCO} and the interannual relationships between D_{LCO} and pre-D_{LCO} T_{min} (the mean of monthly average daily minimum temperature for an optimized period preceding D_{LCO}) for northern vegetation (30°N–75°N, cropland pixels excluded) during the period 2000–2018. We then examined whether the timings of earlier stages of leaf coloration are less responsive to temperature and show fewer

delays and assessed the impacts of temperature on the progress of leaf coloration. Since only a few *in situ* observational programs or networks have monitored D_{LCO}, we determined D_{LCO} from a 5-day composite time series of the NDVI derived from daily surface spectral reflectance (MOD09CMG) at a spatial resolution of 0.05°, provided by the spaceborne Moderate Resolution Imaging Spectroradiometer (MODIS) (Vermote, 2015). To complement the NDVI data, we also used 332 time series of D_{LCO} observed by professional observers according to standard observation guidelines (China Meteorological Administration, 1993) in the field in China (Fig. S1a; Table S2) and the timing of onset of autumnal decline in maximum canopy photosynthetic capacity (D_{PDO}) derived from eddy covariance CO_2 flux observations (Gu et al., 2009; Shen, Tang, Desai, Gough, & Chen, 2014) at 36 sites from in the FLUXNET2015 dataset (Pastorello et al., 2017) (Fig. S1b and Table S3).

2 | MATERIALS AND METHODS

2.1 | Estimating timings of stages of leaf coloration from satellite observations of NDVI time series

2.1.1 | Dataset and preprocessing

The NDVI is a proxy for vegetation greenness and has been widely used for phenological studies at large spatial scales (Buitenwerf, Rose, & Higgins, 2015; Gao et al., 2019; Keenan et al., 2014; Myneni, Keeling, Tucker, Asrar, & Nemani, 1997; Wu et al., 2018). NDVI has also been proved capable of detecting the onset of leaf coloration (Mariën et al., 2019; Soudani, Delpierre, Berveiller, Hmimina, & Dufrêne, 2021; Soudani et al., 2012; Yang, Tang, & Mustard, 2014; Zhao, Donnelly, & Schwartz, 2020). Previous studies have usually used half-month/16-day composite NDVI time series to retrieve phenological metrics. However, because the duration of leaf coloration could be as short as 4 weeks in some areas (Ye & Zhang, 2021), NDVI time-series data with higher temporal resolution are required. We estimated phenological metrics (i.e., the timings of the onset and the advanced stages of leaf coloration and the onset of green-up) for 2000–2018 from a 5-day composite NDVI time series produced from the MODIS reflectance product (MOD09CMG Collection 6, available at https://ladsweb.modaps.eosdis.nasa.gov, accessed on 29 January 2019) (Vermote, 2015). MOD09CMG provides an estimate of daily surface spectral reflectance at a spatial resolution of 0.05°. The quality of the daily surface reflectance data from

MOD09CMG is unsatisfactory owing to cloud and snow contamination (Vermote, 2015), so we used the 5-day maximum value composite approach (Zhang, 2015), combined with a Savitzky-Golay filter (Cao et al., 2018), to produce a high-quality NDVI time series before determining D_{LCO}. First, NDVI values that were lower than the uncontaminated winter (December–February) mean NDVI were replaced by the latter (Beck, Atzberger, Høgda, Johansen, & Skidmore, 2006; Zhang, Tarpley, & Sullivan, 2007). After that, cloud-contaminated and irregularly high and low NDVI values were identified and reconstructed by using a Savitzky-Golay filter (Cao et al., 2018). Details for preparing the high-quality NDVI time series are given in Section 1 of the Supplementary Methods.

We focused on natural vegetation by excluding pixels dominated by cropland, artificial surfaces, permanent snow or ice, and water bodies on the basis of the MODIS land-cover map (MCD12C1 Version 6, https://ladsweb.modaps.eosdis.nasa.gov, accessed on 20 August 2018) (Friedl & Sulla-Menashe, 2015) for the middle year of the time series (2009). Some pixels were also excluded from analysis because of sparse vegetation coverage, weak seasonality, or NDVI peaking in October–April. We adopted three criteria for pixel inclusion: mean annual NDVI must be > 0.10 (Jeong et al., 2011), NDVI should peak between May and September in the multiyear mean NDVI time series (Shen et al., 2020), and mean NDVI for July and August must be >1.15 times the mean NDVI for December and for January–February in every year (Shen, Zhang, et al., 2014).

2.1.2 | Estimating timings of leaf coloration

Two methods can generally be used to estimate the parameters of vegetation phenology (Chen et al., 2016; Shang et al., 2017), including D_{LCO} from annual NDVI profiles. One is based on thresholds (White et al., 1997), whereas the other is based on inflection points (Zhang et al., 2003). We applied the threshold-based method by first using a generalized sigmoid function to fit the NDVI annual profile [Equation (7) in Klosterman et al. (2014)] and then determined D_{LCO} as the first date when NDVI decreased by 10% of its annual amplitude in the descending period (Leblans et al., 2017; Richardson, Hufkens, Milliman, & Frolking, 2018). Though a smaller decrease in NDVI corresponds to an earlier stage of leaf coloration, consideration of it would

167 introduce more uncertainty. We also determined D_{LCO} by using the algorithm based on inflection
168 point. In this method, D_{LCO} was defined as the date when the rate of change of the curvature of a
169 double logistic function (Beck et al., 2006; Elmore, Guinn, Minsley, & Richardson, 2012) fitted
170 to the NDVI time series reached its first local minimum in the descending period (Zhang et al.,
171 2003). Theoretically, the D_{LCO} defined by the inflection method is close to the date when NDVI
172 drops by about 9% of its annual magnitude (Shang et al., 2017).

173 The advanced stages of leaf coloration were determined as the dates when NDVI decreases
174 by 20%, 30%, 40%, and 50% (corresponding to the timing of the end of leaf coloration, D_{LCE}) of
175 its annual amplitude, respectively. In addition, since in a few studies (Berman et al., 2020; Ren,
176 Campbell, & Shao, 2017), the end of leaf coloration was defined as the dates when NDVI drops
177 by 60% or 90% of its annual amplitude, we also included these definitions in analysis. We defined
178 the timing of the onset of green-up as the date when NDVI increased by 20% (Yu et al., 2010).

179 2.1.3 | Evaluation of satellite D_{LCO} using PhenoCam

180 It is unreasonable to validate the satellite-derived D_{LCO} by comparing it with the D_{LCO} of a
181 few plant individuals from ground observation because of mismatch in spatial coverage, different
182 definitions of phenological metrics, and the spatial heterogeneity in phenological phases among
183 individuals for a pixel. Fortunately, pairs of field observations of NDVI and leaf coloration
184 showed good consistency between the start of NDVI decrease and leaf coloration onset (Soudani
185 et al., 2021; Soudani et al., 2012). Moreover, the comparison between start of autumn from
186 satellite observed NDVI and field observations of leaf coloration onset for the entire area covered
187 by the pixel also showed little difference between them (Zhao et al., 2020). Those studies suggest
188 that NDVI is capable to detect the onset of leaf coloration if the observed leaves or individuals
189 are identical between ground and satellite observations. However, there are very limited pairs of
190 compatible observations of NDVI and leaf coloration that can be used for validation.

191 Considering the high capability of PhenoCam in capturing the variations in leaf coloration
192 onset at the landscape scale (Klosterman & Richardson, 2017; Klosterman et al., 2014; Nezval,
193 Krejza, Světlík, Šigut, & Horáček, 2020; Wingate et al., 2015), we used the PhenoCam Dataset
194 V2.0 (Richardson et al., 2018; Seyednasrollah, Young, et al., 2019; SeyednasrollahYoung, et al.,

2019) to assess the relationships between satellite D_{LCO} and the D_{LCO} derived from time series of GCC (green chromatic coordinate) and VCI (vegetation contrast index) observed by PhenoCam. The GCC and VCI were determined from the digital numbers (*DN*) in red (R), green (G), and blue (B) channels. Specifically, GCC and VCI were calculated as $DN_G/(DN_R+DN_G+DN_B)$ and $DN_G/(DN_R+DN_B)$, respectively. Details for the determinations of D_{LCO} from time series of GCC and VCI are given in Section 2 of the Supplementary Methods.

2.2 | D_{LCO} from *in situ* phenological observations

D_{LCO} was extracted at the species level from datasets of *in situ* phenological observations in China provided by the Chinese Academy of Sciences (CAS). The CAS dataset uses the date of first leaf coloring as D_{LCO}. For a given species at a given site, the date of first leaf coloring was identified as the day when the first batch (about 5%) of leaves on more than half of three to five marked individuals started to change color (China Meteorological Administration, 1993). The *in situ* phenological observations were performed visually according to standard observation guidelines (China Meteorological Administration, 1993) every other day by professional observers trained well by CAS. The CAS dataset is available from National Earth System Science Data Sharing Infrastructure, National Science and Technology Infrastructure of China (http://www.geodata.cn, accessed on 25 July 2018).

2.3 | D_{PDO} estimated from maximum canopy photosynthetic capacity

The timing of the onset of the decrease in maximum canopy photosynthetic capacity in autumn (in day of year, D_{PDO}) is defined as the date when the capacity decreases by 10% of its annual amplitude after the data have been fitted to a generalized sigmoid function [Equation (7) in Klosterman et al. (2014)]. The capacity was calculated from half-hourly or hourly gross primary productivity (GPP_NT_CUT_MEAN) based on eddy covariance measurements in the FLUXNET2015 dataset (http://fluxnet.fluxdata.org/data/fluxnet2015-dataset/, accessed on 10 March 2018) (Pastorello et al., 2017). We followed the procedure of Shen, Tang, et al. (2014) to estimate daily canopy photosynthetic capacity, except that the parameters in the rectangular hyperbolic function were estimated by using half-hourly/hourly GPP and incident shortwave radiation calculated by using 15-day moving windows throughout a year. We used data from the

sites in non-Mediterranean (Köppen-Geiger climate classification) and non-cultivated (International Geosphere–Biosphere Programme classification) regions at middle and high northern latitudes (30°N–75°N). In a similar way to the pixel exclusion process that was applied to the satellite retrievals, we discarded sites where weak seasonality (i.e., the mean maximum canopy photosynthesis for June–August was <1.15 times that for December or for January and February) was detected in any year and sites where capacity did not peak in May–September.

2.4 | Analyses

2.4.1 | Temporal changes

Temporal changes of D_{LCO} over the study period were assessed using temporal trends in D_{LCO}, which were quantified as the slopes of linear regressions between D_{LCO} and year by using ordinary least squares regression (OLSR) and *t*-tests. To complement the temporal changes assessed by using OLSR, a non-parametric approach (the Theil-Sen estimator and Mann-Kendall test (Sen, 1968; Theil, 1992)) was also used to calculate the trends in D_{LCO}. Temporal changes of timings of advanced stages of leaf coloration were assessed in the same way.

The temporal trend was calculated for each time series for the ground-based observations and for each pixel for the satellite observations. We focused only on the temporal trends for the pixels and time series of *in situ* phenological observations with a multiyear mean of D_{LCO} occurring after the summer solstice. Phenological records were not available for some of the years of the time series for calculating more trends, because the time series may have had missing values owing to a lack of observation. However, the time series used for the regressions contained at least 10 years of observational records and at least one record for any 3 consecutive years. If two or more parts of the time series met these criteria, the most recent part was used.

2.4.2 | Partial correlation between D_{LCO} and temperature or precipitation

T_{min} has long been recognized as the indicator of the thermal condition that induces autumnal leaf coloration (Tang et al., 2016), and the length of period preceding D_{LCO} in which T_{min} has the largest influence on D_{LCO} could vary among different locations because of differential vegetation characteristics and climate conditions (Gao et al., 2019; Jeong et al., 2011; Matsumoto, Ohta, Irasawa, & Nakamura, 2003; Wu et al., 2018). In addition, precipitation might also regulate

leaf coloration in dry climates (Liu et al., 2016). We thus first determined the length of this period preceding D_{LCO} (referred as pre-D_{LCO} period). Taking satellite-derived D_{LCO} for example, we investigated the impacts of temperature on the D_{LCO} by calculating the partial correlation coefficient (R_{TN}) values between D_{LCO} and the mean of monthly average daily minimum temperature (T_{min}) for the pre-D_{LCO} period, with concurrent total precipitation as the control variable for 2000–2018. The pre-D_{LCO} period for T_{min} (Fig. S2) was defined as the period preceding the multiyear mean D_{LCO} for which T_{min} had the strongest interannual partial correlation with D_{LCO}, with concurrent total precipitation as a control variable (Jeong et al., 2011; Wu et al., 2018). In detail, we first determined several candidate periods that ended at the multiyear mean D_{LCO}, and had a length starting from 1 month, with a step of 1 month. For each of the candidate periods, we calculated the partial correlation coefficient between D_{LCO} and mean T_{min} in each of these periods, and then selected the candidate with the highest absolute value of correlation coefficient. If the multiyear mean D_{LCO} was in the first half of a month, then the pre-D_{LCO} period ended at the month preceding the multiyear mean D_{LCO}. Otherwise, the pre-D_{LCO} period ended at the month of the multiyear mean D_{LCO}. The impacts of T_{min} on the advanced stages of leaf coloration were investigated similarly. A few studies have suggested that the date of onset of green-up may affect leaf coloration through carry-over effects (Cong, Shen, & Piao, 2017; Fu et al., 2014; Keenan & Richardson, 2015; Liu et al., 2016), so we also considered the case in which the onset of green-up was included as an extra control variable in the partial correlation between D_{LCO} and T_{min}. The pre-D_{LCO} period for precipitation and the impacts of precipitation on D_{LCO} were assessed similarly.

The data for T_{min} and precipitation were extracted from the Climatic Research Unit (CRU) Time-Series (TS) 4.03 dataset (http://data.ceda.ac.uk, accessed on 11 June 2019), which provided monthly data at a spatial resolution of 0.5° × 0.5° until 2018. It should be noted that T_{min} in the dataset is an approximation of the mean of daily minimum temperature for a calendar month, which is arithmetically calculated from gridded monthly mean temperature and the diurnal temperature range (Harris, Jones, Osborn, & Lister, 2014) and does not exactly reflect the interannual variations in the absolute minimum temperature (Körner & Hiltbrunner, 2018) experienced by plants before D_{LCO}. The CRU data were resampled at 0.05° × 0.05° by replication

to match the D_{LCO} data.

Complementary to the pre-D_{LCO} period in which T_{min} had the strongest interannual partial correlation with D_{LCO}, we also used fixed lengths (1 month and 15 days preceding multiyear mean D_{LCO}, respectively) as the pre-D_{LCO} periods. We calculated the partial correlation between D_{LCO} and pre-D_{LCO} T_{min} with concurrent total precipitation as the control variable. Moreover, we investigated the partial correlation coefficient between D_{LCO} and the lowest T_{min} during the 15 days before the multiyear mean D_{LCO}, with the concurrent mean T_{min} (mean of the remaining 14 T_{min} values after removal of the lowest T_{min} during the period) and total precipitation as control variables. Note that when the pre-D_{LCO} period was defined as the 15 days preceding D_{LCO} and when we analyzed the relationship between the lowest T_{min} and D_{LCO}, daily T_{min} and precipitation were extracted from CRU-NCEP dataset (Version 7.2, https://vesg.ipsl.upmc.fr, assessed on 10 January 2019), which provides 6-hourly data at a spatial resolution of 0.5° × 0.5° through 2016 (Viovy, 2018). The CRU-NCEP 7.2 is a combination of two datasets: the CRU TS3.2 0.5° × 0.5° monthly data covering the period 1901 to 2002 and the NCEP reanalysis 2.5° × 2.5° 6-hourly data covering the period 1948 to 2016. We determined daily T_{min} as the minimum value of the four 6-hourly minimum temperature values for each day. The CRU-NCEP data were resampled at 0.05° × 0.05° by replication to match the D_{LCO} data.

We also investigated the impact of T_{min} and precipitation on D_{LCO} from ground-based observations in China and on D_{PDO} from eddy-covariance sites as complementary to satellite-derived D_{LCO}. Climatic data for *in situ* observations in China was extracted from the "Daily Surface Climate Variables of China" catalog (a dataset named SURF_CLI_CHN_MUL_DAY_V3.0), which includes daily climate data for 2474 sites in China from January 1951 to July 2014, provided by the Chinese Meteorological Administration. The distance between phenological and meteorological stations was less than 25 km. Climatic data for D_{PDO} were calculated from the half-hourly temperature dataset provided by FLUXNET2015.

2.4.3 | Relationships between the progress of leaf coloration and temperature

The impacts of temperature on the progress of leaf coloration were assessed in four ways. (1) We calculated the partial correlation coefficient between each of the timings of different stages

in leaf coloration (determined as NDVI decreases by 20%, 30%, 40, 50%, 60%, and 90%) and preceding T_{min} using the approach described in Section 2.4.2. We then compared the percentage of area corresponding to the partial correlation coefficient among the different timings. (2) Difference in temperature sensitivity between the D_{LCE} and D_{LCO} was used to assess the differential responses to T_{min} between D_{LCE} and D_{LCO}. The temperature sensitivity of D_{LCO} was defined as the coefficient for pre-D_{LCO} T_{min} in a linear regression in which D_{LCO} was set as the dependent variable, and pre-D_{LCO} T_{min} and pre-D_{LCO} total precipitation were independent variables. The temperature sensitivity of D_{LCE} was calculated similarly. See 2.4.2 for the details of the determination of pre-D_{LCO} (or pre-D_{LCE}) T_{min} and total precipitation. (3) Temperature sensitivity of the length of duration of leaf coloration was used to assess the impact of temperature on the length of duration of leaf coloration. The duration of leaf coloration was defined as the difference between D_{LCE} and D_{LCO}. Its temperature sensitivity was estimated as the coefficient for mean T_{min} in the linear regression in which the length was set dependent variable and the mean T_{min} and total precipitation in the period between D_{LCE} and D_{LCO} were independent variables. 4) Temperature sensitivity of the speed of leaf coloration was used to assess the impact of temperature on the speed of leaf coloration within a season. The speed of leaf coloration within a season was defined as the normalized decreasing speed of NDVI between D_{LCE} and $D_{LCO,}$ calculated as $-(NDVI_{DLCE} - NDVI_{DLCO})/(D_{LCE} - D_{LCO})/AMP_{NDVI}$, where AMP_{NDVI} is the annual amplitude of NDVI for a given pixel and given year. Temperature sensitivity of the speed of leaf coloration was then calculated as the coefficient for mean T_{min} when regressing the speed of leaf coloration against mean T_{min} and total precipitation between D_{LCE} and D_{LCO}. Here, T_{min} and precipitation were extracted from the CRU TS 4.03 monthly data.

2.4.3 | Dependence of D_{LCO} on daylength

Previous experimental findings suggest the daylength as a signal for the start of autumn leaf senescence (Table S1), indicating a photoperiodic control on D_{LCO}. However, it is difficult to assess the role of daylength by using interannual correlations between D_{LCO} and daylength under natural conditions since the daylength on a given date does not vary among years. Alternatively, because control of photoperiod on autumn leaf phenology may vary with daylength across different regions (Howe, Hackett, Furnier, & Klevorn, 1995; Pau et al., 2011; Paus, Nilsen, & Junttila, 1986; Saikkonen et al., 2012), we examined the variabilities in the correlation between

D_{LCO} and T_{min} and in temporal changes in D_{LCO} against the spatial gradient of daylength to explore the dependence of D_{LCO} on daylength. Meanwhile, the spatial variations in the response of autumn leaf phenology to temperature might be associated with local background temperature conditions (Ford, Harrington, & Clair, 2017; Zohner, Benito, Svenning, & Renner, 2016). Hence, the spatial variations in background temperature should be minimized when assessing the dependence of D_{LCO} on daylength. To do this, we first calculated the daylength for each pixel at the date of multiyear mean D_{LCO} over the period 2000–2018 and the mean T_{min} of the period before multiyear mean D_{LCO}. The period before multiyear mean D_{LCO} was the month preceding the multiyear mean D_{LCO} if the multiyear mean D_{LCO} was in the first half of a month; otherwise, the period was the month of the multiyear mean D_{LCO}. After that, for each cell of 1.5-hour daylength and 4-°C mean T_{min} in the space of the daylength and mean T_{min} (see Fig. 5 for graphic illustration), we calculated the percentage of area with significant ($P < 0.05$, *t*-test) D_{LCO} delays, the average of positive correlation, and the percentage of area with a positive correlation between D_{LCO} and T_{min} (or precipitation). In addition, there is more experimental evidence of photoperiodic control on the onset of leaf senescence for woody plants than for herbaceous plants (Table S1), indicating woody and herbaceous vegetation may respond to photoperiod differently. Therefore, the above exploration was also performed separately for woody and herbaceous vegetation, separately. Here, woody and herbaceous vegetation were merged from Classes 1–6 and Class 10, respectively, in the MODIS land-cover product (MCD12C1, Version 6) for 2009 (Friedl & Sulla-Menashe, 2015).

2.4.4 | Possible effect of summer NDVI

In some deciduous forests, NDVI may decline in early summer (i.e., late May–July) before leaf coloration, and this may potentially interfere with the determination of D_{LCO} to some extent (Elmore et al., 2012) and its relationship with temperature. To address this, for the pixels classified as deciduous broadleaf forest in the MODIS land-cover product (Friedl & Sulla-Menashe, 2015), we redefined D_{LCO} considering the possible effect of summer NDVI decline on D_{LCO} and then re-analyzed the trends in D_{LCO} and the relationship between D_{LCO} and temperature as described in Sections 2.4.1 and 2.4.2. For the sake of robustness, the possible effect of summer NDVI decline on D_{LCO} was considered in three different ways: (1) We used a modified double logistic model that considers early summer NDVI decline (Elmore et al., 2012) to fit the NDVI time series instead

of the original double logistic function for the pixels classified as deciduous broadleaf forest. D_{LCO} was then determined as the date when the rate of change of the curvature of a double logistic function fitted to the NDVI time series reached its first local minimum in the descending period; (2) D_{LCO} was defined as the date when NDVI decreased by 10% of its annual amplitude from 1 August. The maximum value used to determine the annual amplitude was the mean value of the upper quartile of the fitted NDVI values in August; and (3) D_{LCO} was defined as the date when NDVI decreased by 10% of its annual amplitude from 16 August. The maximum value used to determine the annual amplitude was the mean value of the upper quartile of the fitted NDVI values in the second half of August.

2.4.5 | Possible cold events before D_{LCO} (or D_{PDO})

A sudden drop of nighttime temperature to the freezing point can induce leaf coloration in a few days (Körner, 2007), and this may interfere with our partial correlation analysis between D_{LCO} (or D_{PDO}) and temperature. Hence, we re-examined the temporal changes in D_{LCO} and the correlation between D_{LCO} and temperature as described in Sections 2.4.1 and 2.4.2, after excluding possible cold events estimated using an empirical approach as follows (taking satellite-derived D_{LCO} for example).

First, we determined the T_{min} threshold below which there could potentially be a cold event for each pixel. Since cold event that induces rapid leaf senescence should happen 1–5 days before D_{LCO}, the lowest T_{min} during the 6 to 35 days before D_{LCO} for all years was set as the T_{min} threshold. A temperature higher than such a threshold will not induce a cold event. For vegetation in middle and high latitudes, a temperature higher than freezing (0 °C) does not cause frost damage (Körner, 2021; Lenz, Hoch, Vitasse, & Körner, 2013; Sakai & Larcher, 1987; Taschler & Neuner, 2004). Therefore, if the lowest T_{min} was higher than 0 °C, the T_{min} threshold was set to 0 °C.

Second, for a given pixel, a year was determined as a candidate cold event year if the lowest T_{min} in the period 1 to 5 days before D_{LCO} was lower than the above-mentioned T_{min} threshold. Then, from the years in which there was no candidate cold event, we determined the latest D_{LCO} that was not caused by a cold event for that pixel.

Finally, a D_{LCO} was recognized as possibly caused by a cold event if it was in the candidate cold event years and meantime earlier than the latest D_{LCO} that was not caused by a cold event. For a D_{LCO} (referred to as D'_{LCO}) from the candidate cold event years and later than the latest D_{LCO} that was not caused by a cold event, it (D'_{LCO}) would be recognized as a D_{LCO} possibly caused by a cold event if one of the following two conditions is met: (1) the decreasing rate of T_{min} in the period 1 to 5 days before D'_{LCO} was faster than the maximum decreasing rate of T_{min} among the years in which there was no candidate cold event; (2) the decrease (absolute value) in T_{min} in the period 1 to 5 days before D'_{LCO} was greater than the maximum decrease in T_{min} among the years with no candidate cold event. Here, for a given year, the decreasing rate of T_{min} in the period 1 to 5 days before D_{LCO} (or D'_{LCO}) was calculated as the minimum of the slopes of T_{min} against calendar date. A slope of T_{min} against calendar date was calculated as [T_{min}(time2)– T_{min}(time1)]/(time2– time1), where time2 = D_{LCO}–1, D_{LCO}–2, D_{LCO}–3, D_{LCO}–4, or D_{LCO}–5 and time1 = D_{LCO}–2, D_{LCO}–3, D_{LCO}–4, or D_{LCO}–5, and time2 is later than time1. The decrease in T_{min} in the period 1 to 5 days before D_{LCO} (or D'_{LCO}) for a given year is the maximum value of magnitudes of [T_{min}(time2)– T_{min}(time1)].

This empirical approach may have overestimated the number of years with cold events before D_{LCO} (hereafter, these identified events were referred as possible cold events), but our objective here is to exclude cold events as many as possible and then to examine if the main findings of our study were caused by cold events. In addition, under clear skies, the temperature of the canopy surface could be lower than the air temperature, so we also determined the possible cold events by using 2 °C as the T_{min} threshold (Körner, 2021).

Here, the daily T_{min} used to determine possible cold events for satellite-derived D_{LCO} was extracted from the CRU-NCEP 7.2 dataset. Daily T_{min} for ground-based observations in China was derived from the nearest meteorological station (<25 km), provided by the Chinese Meteorological Administration. Daily T_{min} for D_{PDO} was calculated from the half-hourly temperature dataset provided by FLUXNET2015.

3 | RESULTS

3.1 | Comparison of satellite D_{LCO} with PhenoCam D_{LCO}

The satellite D_{LCO} explained more than 80% of the variations in PhenoCam derived D_{LCO} (N = 378 and 377 for GCC and VCI, respectively) (Fig. 2). The differences between the satellite D_{LCO} and the PhenoCam D_{LCO} are caused by the mismatch between the annual NDVI and GCC (or VCI) trajectories due to the difference in spatial coverage between the PhenoCam and satellite pixel in the cases of phenologically heterogeneous land surface (see Section 2 of the Supplementary Methods).

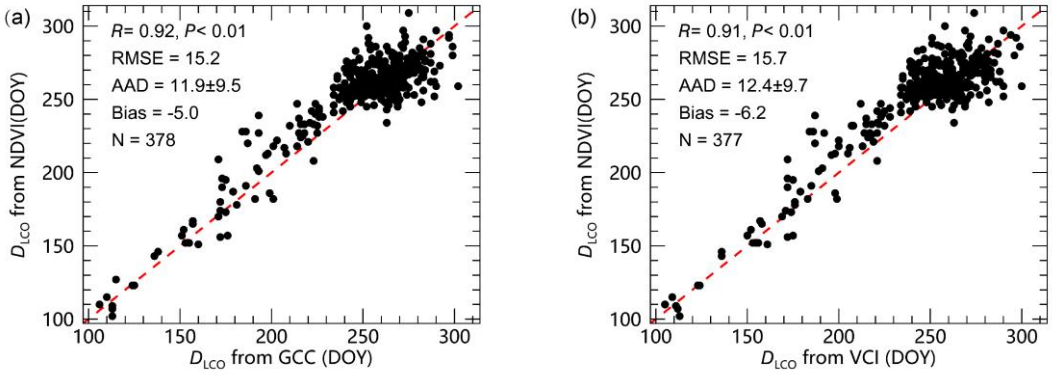

Fig. 2 Comparison between satellite D_{LCO} and PhenoCam D_{LCO}. The PhenoCam D_{LCO} was determined from GCC (a) and VCI (b), respectively. *R*: Pearson's correlation coefficient; RMSE: root mean square error; AAD: average absolute difference; bias is defined as the difference between the mean of satellite D_{LCO} and the mean of PhenoCam D_{LCO}, and negative bias means the PhenoCam D_{LCO} is earlier than satellite D_{LCO}.

3.2 | Proportion of possible cold events before D_{LCO} (or D_{PDO})

Possible cold events occurred before D_{LCO} or D_{PDO} in very small fractions of pixel-years/site-years with phenological data (1.6%, 1.7%, and 0.6% for satellite D_{LCO}, ground-based observations in China, and D_{PDO} from eddy-covariance sites, respectively; Table 1). The proportion of years possibly affected by cold events was slightly higher when using the method based on a temperature threshold of 2 °C than that of 0 °C.

Table 1. Proportions of years with possible cold events before D_{LCO} (for satellite and *in situ* observations) and before D_{PDO} (for FLUXNET2015).

Metrics	Satellite D_{LCO}	*in situ* D_{LCO}	FLUXNET2015

	(2000–2016)	China	D_{PDO}
Proportion (%) of years with possible cold events (0 °C)	1.6	1.7	0.6
Proportion (%) of years with possible cold events (2 °C)	2.1	3.5	1.0

D_{LCO}, timing of onset of leaf coloration in autumn; D_{PDO}, timing of onset of the decrease in maximum canopy photosynthetic capacity in autumn. Possible cold events were determined mainly by using a threshold-based method with a daily minimum temperature of 0 °C or 2 °C (see Section 2.4.5 for identification of possible cold events).

3.3 | Temporal trends in D_{LCO} and the advanced stages of leaf coloration

D_{LCO} was not significantly delayed in 94% of the area during the study period, as assessed by OLSR. The few pixels with a significant delay trend (6%; $P < 0.05$, *t*-test) were scattered across the Northern Hemisphere (Fig. 3a). Excluding years with possible cold events before D_{LCO} produced similar results (Fig. S3 and Table S4). The Theil-Sen estimator generated results supporting the lack of changes in D_{LCO} (no significant delay in 96% of the area; $P < 0.05$, Mann-Kendall test; Fig. S4a and Table S5). When we defined D_{LCO} as the inflection point at which NDVI begins to decline, we obtained similar results (Fig. S4b and c). Considering early summer NDVI decline produced similar results (Figs. S5, S6, and S7).

Complementary to satellite-derived D_{LCO}, we also examined the temporal changes of D_{LCO} by using ground-based leaf coloration data from China. D_{LCO} was not significantly delayed for 90% and 94% of the 332 time series as shown by OLSR (Fig. 3b) and the Theil-Sen method (Table S5), respectively. Similar results were produced when possible cold events were excluded (Table S4).

The timings of earlier stages of leaf coloration exhibited delaying trends in fewer areas. The leaf coloration stages determined as the dates when NDVI decreases by 50% (i.e., D_{LCE}), 40%, 30%, 20%, and 10% (i.e., D_{LCO}) were significantly ($P < 0.05$, *t*-test) delayed for 14%, 14%, 12%, 9%, and 6% of the area, respectively (Fig. S8).

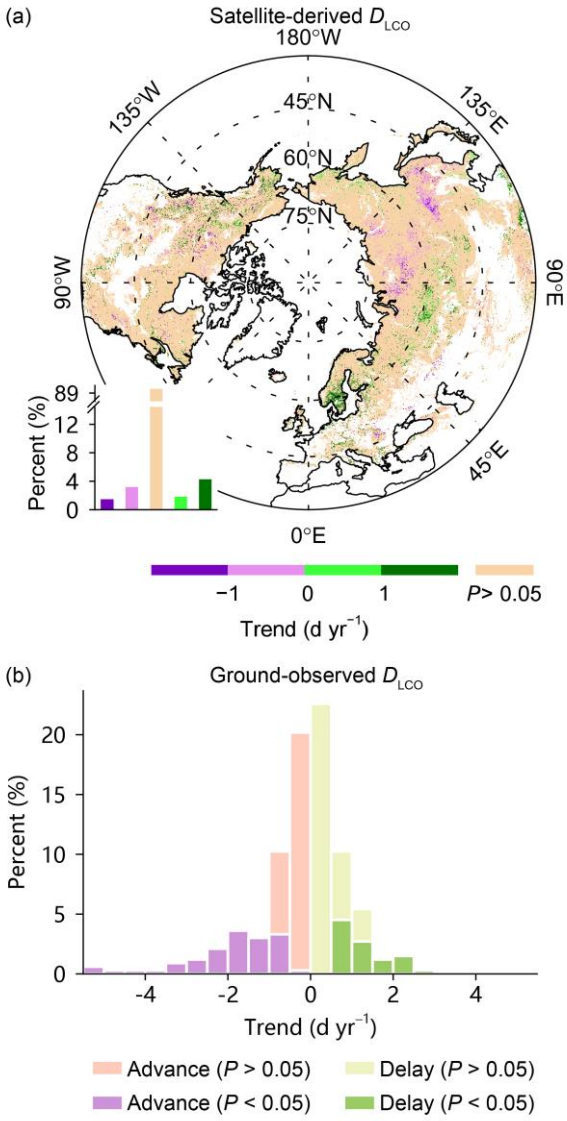

468

469 **Fig. 3** Temporal trends in the timing of the onset of leaf coloration (D_{LCO}), as retrieved from
470 satellite and *in situ* observations. (a) Satellite-derived D_{LCO} trends over 2000–2018. The bar chart
471 in the bottom-left corner shows the percentage of area within each interval of the significant
472 temporal trends and the percentage of area with nonsignificant trends, indicated by the color scale
473 at the bottom. Positive and negative trend values refer to significantly delayed and advanced D_{LCO},
474 respectively. D_{LCO} corresponds to a 10% decrease in NDVI. (b) Ground-observed D_{LCO} trends
475 derived over 1971–1997 from *in situ* leaf coloration observations in China. Significant temporal
476 trends were determined by using *t*-tests at $P < 0.05$ and ordinary least squares regression.

477

478 **3.4 | Correlation between D_{LCO} and temperature or precipitation**

D_{LCO} was not consistently correlated with pre-D_{LCO} T_{min}, with only 9% of the area in scattered pixels showing a significant positive correlation and 5% showing a significant negative correlation (Fig. 4a). D_{LCO} was positively correlated with pre-D_{LCO} total precipitation in 13% of the area, mainly in the temperate grassland of Northern America and in the middle latitudes of Eurasia, sub-arctic grassland, and alpine steppe of the Tibetan Plateau (Fig. S9). Therefore, neither pre-D_{LCO} T_{min} nor precipitation was a useful predictor of D_{LCO} in most areas. We obtained similar results when using the month preceding D_{LCO} (Fig. S10) or 15 days preceding D_{LCO} (Fig. S11) as the pre-D_{LCO} period, with only 6% and 5%, respectively, of the area showing a significant positive correlation between D_{LCO} and pre-D_{LCO} T_{min}. We also investigated the relationship between D_{LCO} and the lowest daily minimum temperature during the 15 days before the multiyear mean D_{LCO} and only 3% of the area showed a significant positive correlation (Fig. S12). Moreover, including the date of onset of green-up as an extra control variable in the partial correlation analyses did not affect the results (Fig. S13). The *in situ* phenological records in China indicated that ground-observed D_{LCO} was positively correlated with pre-D_{LCO} T_{min} for 13% of the time series and was not correlated with pre-D_{LCO} T_{min} for 82% of the time series (Table 2). Excluding D_{LCO} possibly caused by cold events produced similar results (Fig. S14 and Table S6). Overall, these results suggest that an increase in pre-D_{LCO} T_{min} is not likely to delay D_{LCO} in most areas in the middle and high northern latitudes.

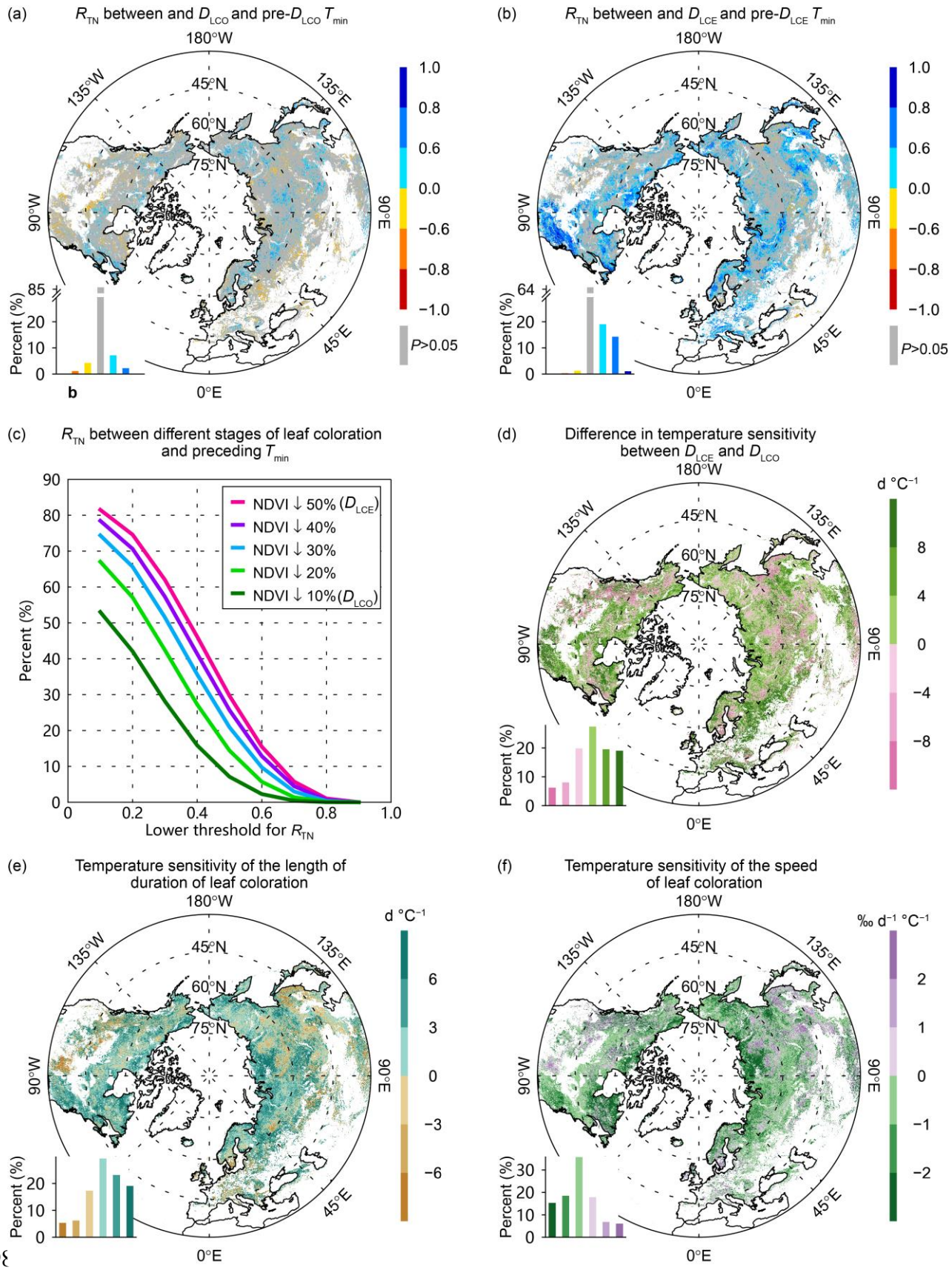

498

499 **Fig.** 4 Impacts of temperature on the timing of different stages of leaf coloration and on the
500 progress of leaf coloration over the period 2000–2018. (a) Spatial pattern of the partial correlation

coefficient (R_{TN}) between the onset of leaf coloration (D_{LCO}, 10% decrease in NDVI) and pre-D_{LCO} mean daily minimum temperature (T_{min}). (b) Spatial pattern of R_{TN} between timing of the end of leaf coloration (D_{LCE}, 50% decrease in NDVI) and pre-D_{LCE} T_{min}. The bar charts in (a) and (b) show the percentage of area for each interval of the partial correlation coefficient ($P < 0.05$), with the coefficient indicated by the color scale on the right. Non-significant correlations ($P > 0.05$) are in gray. (c) Percentage of area for which R_{TN} between the timing of a given stage of leaf coloration and preceding T_{min} is higher than a given threshold indicated by the horizontal axis. For example, R_{TN} for the onset of leaf coloration is higher than 0.2 in about 40% of the area. (d) Difference in temperature sensitivity between D_{LCE} and D_{LCO}. Positive values indicate that D_{LCE} is more sensitive to temperature than D_{LCO}, whereas negative values indicate that D_{LCO} is more sensitive to temperature than D_{LCE}. (e) Temperature sensitivity of the length of duration of leaf coloration. Positive values indicate that warming extends the duration of leaf coloration, whereas negative values indicate that warming shortens the leaf coloration duration. (f) Temperature sensitivity of the speed of leaf coloration. Positive values indicate that warming increases the speed of leaf coloration, whereas negative values indicate that warming reduces the speed of leaf coloration. The bar charts in (d), (e), and (f) show the percentage of area for each interval of the temperature sensitivity indicated by the color scale on the right.

Table 2. Percentage of correlations between D_{LCO} or D_{PDO} and each climate factor for each interval of the partial correlation coefficient.

Metric	Number of time series	Climate factor	Interval of the partial correlation coefficient ($P < 0.05$)						$P > 0.05$
			[−1.0, −0.8)	[−0.8, −0.6)	[−0.6, 0)	(0, 0.6]	(0.6, 0.8]	(0.8, 1.0]	
in situ D_{LCO} China	332	Temperature	0	2	3	4	8	1	82
		Precipitation	0	3	3	4	5	0	85
FLUXNET2015 D_{PDO}	36	Temperature	0	5	3	0	3	0	89
		Precipitation	0	6	0	8	3	5	78

D_{LCO}, timing of the onset of leaf coloration in autumn; D_{PDO}, timing of the onset of the decrease in maximum canopy photosynthetic capacity in autumn. The data in the farthest right column indicate the percentages of area or time series with non-significant correlations.

3.5 | Impacts of temperature on the progress of leaf coloration

We first examined whether the timings of earlier stages of leaf coloration are less closely related with temperature than later stages. The fact that the earlier stages of leaf coloration had fewer areas with a significantly delayed trend (Fig. S8) matches that the significantly positive correlations between the timings of earlier stages of leaf coloration and T_{min} were observed in fewer areas (Fig. 4c). The timings of leaf coloration stage corresponding to NDVI decreases by 40%, 30%, 20%, and 10% (i.e., D_{LCO}) were significantly positively correlated with T_{min} in 30%, 25%, 17%, and 9% of the area (Figs. 4a and c, and S15). Particularly, D_{LCE} was significantly positively correlated with pre-D_{LCE} T_{min} in 34% of the area (Fig. 4b), substantially more than that for the D_{LCO}-T_{min} correlations (9%, Fig. 4a). The proportion increased to 38% and 41% for the timings of leaf coloration stage corresponding to a 60% and 90% decrease in NDVI (Fig. S16). These above results show decreasing correlations with temperature of earlier stages of leaf senescence. To further verify this, we examined the correlation between D_{PDO}, an indicator of leaf senescence earlier than D_{LCO}, and pre-D_{PDO} T_{min}. D_{PDO} and pre-D_{PDO} T_{min} were less positively correlated than were NDVI-derived D_{LCO} and pre-D_{LCO} T_{min} at the same sites during the same periods (3% and 6% of the sites for D_{PDO} and D_{LCO}, respectively, Table S7). Among all the eddy-covariance towers, D_{LCO} was significantly positively correlated with pre-D_{LCO} T_{min} in 3% of the 36 and was not correlated with pre-D_{PDO} T_{min} in 89% of the eddy-covariance records (Table 2). Moreover, excluding D_{PDO} possibly caused by cold events produced similar results (Table S6).

We then examined whether D_{LCO} is less sensitive to temperature than D_{LCE}. In most regions (66%) of the middle and high northern latitudes, the temperature sensitivity of D_{LCO} was smaller than that of D_{LCE} (Fig. 4d). The temperature sensitivity of D_{LCO} was less than D_{LCE} by at least 4 d $°C^{-1}$ in 39% of the study area, mainly in northern Europe, the eastern USA, eastern Canada, and western Russia. In 14% of the area, the temperature sensitivity of D_{LCO} was more than 4 d $°C^{-1}$ greater than D_{LCE}, mainly distributed in the Tibetan Plateau, western North America, area in Europe near 60°N, northern Kazakhstan, and between 45°N and 65°N in Russia.

As can be expected from the smaller temperature sensitivity of D_{LCO} relative to that of D_{LCE}, warming could extend the duration of leaf coloration in 71% of the area (Fig. 4e). In 42% of the

area, the temperature sensitivity of the length of duration of leaf coloration was greater than 3 d $°C^{-1}$, mainly in Russia, eastern North America, and northern Europe. The area with a temperature sensitivity lower than − 3 d $°C^{-1}$ accounted for 11% of the study area, scattered in Tibetan Plateau, central USA, western North America, between 45°N and 60°N in Europe, northern Kazakhstan, and southeastern Russia.

Moreover, warming could slow the progress of leaf coloration. In 69% of the area, the speed of leaf coloration could be reduced by higher temperature (Fig. 4f), particularly in the region north of 60°N. The temperature sensitivity of the speed of leaf coloration was lower than –1‰ d^{-1} $°C^{-1}$ in 34% of the study area (negative values of temperature sensitivity indicate that warming reduces the speed of leaf coloration), mainly in eastern and northern Canada, northern Europe, and northern Russia. Only 13% of the area showed a highly increasing in the speed of leaf coloration under increasing temperature (> 1‰ d^{-1} $°C^{-1}$), scattered in Mongolia, Tibetan Plateau, western Canada, central and western USA, and central and southeastern Russia.

When considering early summer NDVI decline, we also found that more advanced stages of leaf coloration were more responsive to temperature (Figs. S17c, S18c, S17d and S18d), and warming could slow the coloration progress (Figs. S17f and S18f) and extend the duration of leaf coloration (Figs. S17e and S18e).

3.6 | Dependence of D_{LCO} on daylength

We attempted to explore the dependence of D_{LCO} on daylength, by examining the variabilities in the correlation between D_{LCO} and T_{min} and in temporal changes in D_{LCO} against the spatial gradient of daylength. In the areas with longer daylengths at multiyear mean D_{LCO}, there were proportionally fewer significant D_{LCO} delays during 2000–2018 (Fig. 5a and Fig. S19a), and the positive relationship between D_{LCO} and pre-D_{LCO} T_{min} was slightly weaker, as indicated by the smaller partial correlation coefficient between them (Fig. 5d). Such patterns were more prominent for woody vegetation than for herbaceous vegetation (Fig. 5b, c, e, and f; Fig. S19b and c). For vegetation with a daylength at D_{LCO} of more than 13.5 h, D_{LCO} was more positively correlated

with pre-D_{LCO} T_{min} in colder areas at a given daylength (Fig. 5d–f). The dependences of D_{LCO} trends on daylength and of the correlation between D_{LCO} and pre-D_{LCO} T_{min} on daylength were also found when years with possible cold events before D_{LCO} were excluded (Fig. S20) and when we considered summer decline in NDVI (Figs. S21 and S22). The correlation between D_{LCO} and pre-D_{LCO} total precipitation was independent of daylength and was slightly stronger for the areas with a higher temperature before D_{LCO}, mostly because of the stronger effect of precipitation in delaying D_{LCO} in herbaceous vegetation (Figs. S9 and S23).

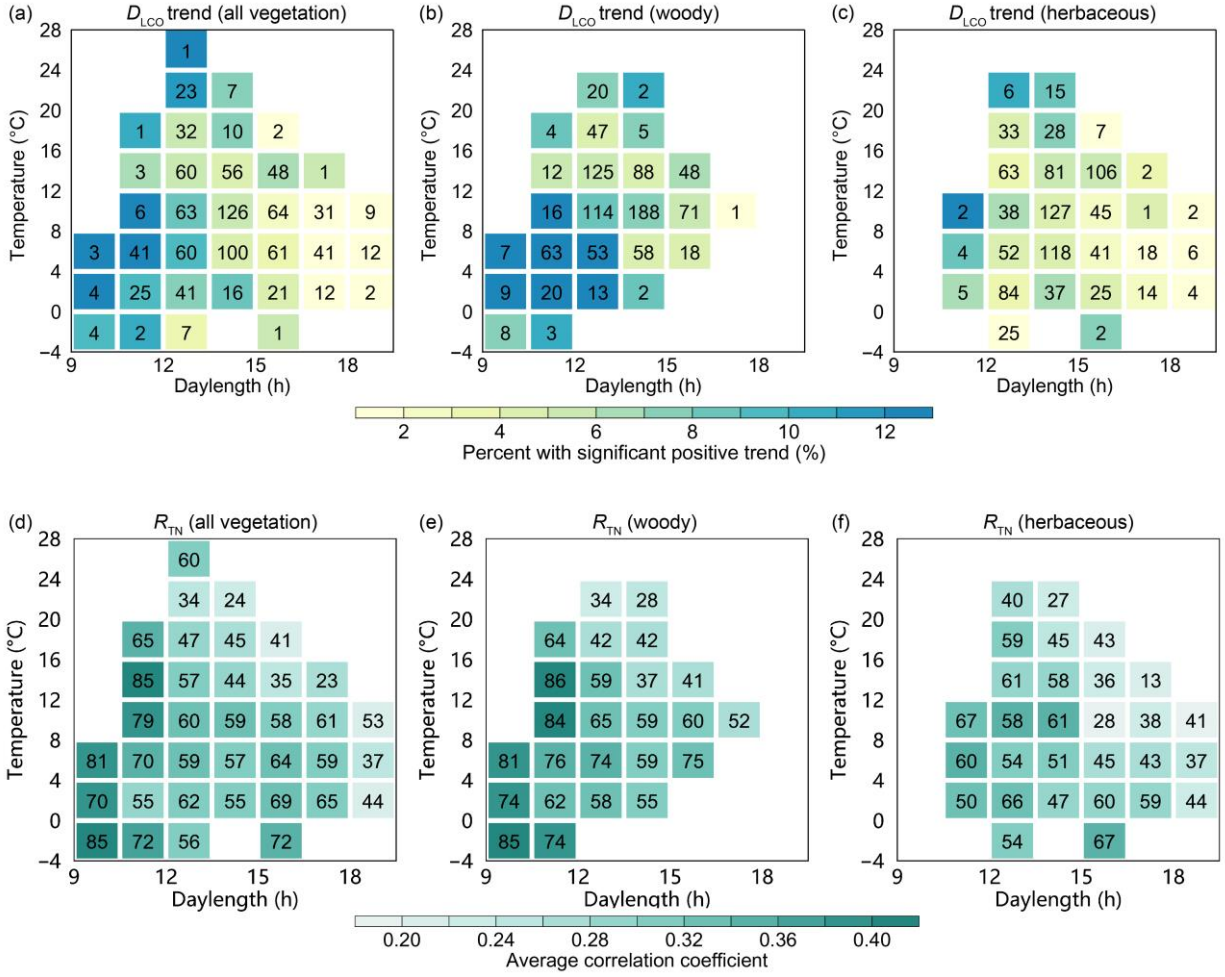

Fig. 5 Dependence of temporal trends in the timing of the onset of leaf coloration (D_{LCO}, 10% decrease in NDVI, a–c) and of the partial correlation coefficient (R_{TN}, d–f) between D_{LCO} and pre-D_{LCO} mean daily minimum temperature (T_{min}) on daylength and temperature over the period 2000–2018. (a) All vegetation. Color indicates the percentage of area with significant ($P < 0.05$) D_{LCO} delays in each cell (i.e., a specific temperature × daylength combination), as indicated in the

scale at the bottom. The number in each cell indicates the ratio (unit: ‰) of the area in each cell to the total area with D_{LCO} retrieval. The temporal trends and their significances were determined with ordinary least squares regression and *t*-tests. (b) and (c), The same as (a) but for woody and herbaceous vegetation, respectively. (d) All vegetation. Color indicates the average of the positive R_{TN}, as indicated in the scale at the bottom. The number in each cell indicates the percentage of area with a positive correlation in each cell. (e) and (f), The same as (d) but for woody and herbaceous vegetation, respectively. Only cells where the ratio of the area of the cell to the total area is >1‰ are represented.

4 | DISCUSSION

In previous analyses of *in situ* and satellite observations (Garonna et al., 2014; Gill et al., 2015; Liu et al., 2016), the advanced stage of autumnal leaf senescence, indicated by D_{LCE}, was significantly delayed in a larger proportion of areas, or time series, than was D_{LCO} in our study. In the current study, D_{LCE} was also significantly delayed in more areas than D_{LCO} (Fig. S8), probably because the timings of the earlier stages of leaf coloration determined from satellite data were less affected by T_{min} than the later stages (Figs. 4a-c and S15). Evidence for photoperiodic control of the start of leaf senescence (Fracheboud et al., 2009; Keskitalo et al., 2005) suggests that the early phases of leaf senescence are insensitive to warming, in contrast to the later phases. Since the degradation of chlorophyll starts earlier than leaf coloration (Lim, Kim, & Nam, 2007; Tang et al., 2016), the timing of autumnal phenological metrics that closely follow chlorophyll degradation before D_{LCO} should be less delayed by temperature increase than D_{LCO} if chlorophyll degradation is triggered by the photoperiod. In our analysis, we verified that D_{PDO} was less positively correlated with temperature than D_{LCO} (Table S7), probably because the start of autumnal chlorophyll degradation was controlled by photoperiod and was not delayed by higher temperature (Bauerle et al., 2012; Fracheboud et al., 2009; Keskitalo et al., 2005).

Overall, our results suggest that temperature does not initiate senescence in autumn in most areas; rather, it influences the speed of coloration change after it starts (Fig. 4f) (Fracheboud et al., 2009). The lack of a positive correlation between D_{LCO} (or D_{PDO}) and pre-D_{LCO} (or pre-D_{PDO}) temperature suggests an overriding photoperiodic control that makes the timing of the onset of

622 leaf senescence stable. In the areas with longer daylengths (calculated for each pixel/location at
623 multiyear mean D_{LCO} over 2000–2018), there were proportionally fewer significant D_{LCO} delays
624 during 2000–2018 (Fig. 5a and Fig. S19a), and the positive relationship between D_{LCO} and pre-
625 D_{LCO} T_{min} was slightly weaker, as indicated by the smaller partial correlation coefficient between
626 them (Fig. 5d). Such dependences on daylength were more prominent for woody vegetation than
627 for herbaceous vegetation (Fig. 5b, c, e, and f; Fig. S19b and c), in agreement with experimental
628 findings suggesting that the initiation of leaf senescence in woody plants is likely controlled by
629 photoperiod (Fracheboud et al., 2009; Keskitalo et al., 2005). These findings indicate stronger
630 photoperiodic control in areas where daylength at D_{LCO} is longer (i.e., shorter nights), possibly
631 because plants respond to the length of uninterrupted darkness rather than daylength (Borthwick
632 & Hendricks, 1960; Hamner, 1940; Howe et al., 1995; Paus et al., 1986). Interestingly, for
633 vegetation with a daylength at D_{LCO} of more than 13.5 h, D_{LCO} was more positively correlated
634 with pre-D_{LCO} T_{min} in colder areas (Fig. 5d–f), indicating a stronger effect of temperature in areas
635 with harsh temperature conditions, consistent with experimental studies (Ford et al., 2017; Zohner
636 et al., 2016). Therefore, although for these types of vegetation the correlation between D_{LCO} and
637 temperature is weak, probably because of stronger photoperiodic control, there is still a signal of
638 temperature influence on D_{LCO}, reflecting a stronger selection pressure in harsher temperature
639 environments.

640 Although observational evidence is limited, experimental results have been reported for the
641 photoperiodic induction of leaf senescence in several, mostly woody, species (Table S1). However,
642 in those manipulative experiments, daylength was altered by several hours (> 4 h, Table S1),
643 which is more extreme than the natural conditions plants are likely to experience. Daylength
644 depends only on the day of year and location. Because of the inter-annual limited variations in the
645 timings of leaf coloration or senescence onset, the fluctuation in daylength under natural
646 conditions is far less than that in manipulative experiments. Therefore, the role of photoperiod in
647 leaf senescence identified under such experimental conditions does not necessarily apply to plants
648 under natural conditions. The results in this study support experimental findings in wild plants at
649 the biome and continental scales and show that photoperiod influences the onset of leaf coloration,
650 which closely follows the initiation of leaf senescence.

651 Autumnal leaf senescence in preparation for overwintering is an evolutionary trade-off
652 between the reallocation of leaf nutrients before leaf shed to reduce the risk of frost damage and
653 the assimilation of carbon (Estiarte & Peñuelas, 2015). The response of leaf senescence to an
654 increase in temperature in autumn influences this trade-off. The absence of delays over time in
655 the onset of leaf coloration and in the onset of decrease in maximum canopy photosynthetic
656 capacity in response to climate warming, as observed in our study, may limit the detrimental
657 effects of frost in autumn (Liu et al., 2018) and may also pose limited impacts on the start of the
658 remobilization and resorption of nutrients (Estiarte & Peñuelas, 2015). The slower progress rate
659 of leaf senescence (Fig. 4f) and extended duration of leaf coloration (Fig. 4e) under warming may
660 increase the efficiency of nitrogen resorption (Rennenberg, Wildhagen, & Ehlting, 2010) and
661 increase the vegetation greenness in this period, which will modify on the surface energy balance
662 through biophysical processes (Shen et al., 2015). The extended period of leaf coloration may also
663 prolong the plant transpiration time and increase soil water consumption. The impact of autumn
664 warming on net ecosystem productivity is dual, increasing both respiratory flux to the atmosphere
665 (Piao et al., 2008) and forest gross primary photosynthesis (Keenan et al., 2014). The relatively
666 static onset date of leaf coloration and its weak response to temperature would preclude the
667 vegetation from fully using the potential increase in CO_2 assimilation in early autumn induced by
668 warming (Stinziano & Way, 2017). Combined with a delay in the end of the season and a
669 respiration increase due to warming, this suggests that additional warming will probably not result
670 in a continuous increase in autumn CO_2 assimilation.

671

672 In summary, satellite NDVI time series and ground-based phenological observations
673 indicated no significant delay in the start of autumnal leaf coloration for most areas covered by
674 natural vegetation over middle and high northern latitudes. Neither pre-D_{LCO} temperature nor pre-
675 D_{LCO} precipitation significantly affected the interannual variations of the start of leaf coloration
676 in most areas, indicating that the start of leaf senescence is triggered by photoperiod. Interestingly,
677 there was a weaker positive correlation between the start of autumnal leaf coloration and pre-D_{LCO}
678 T_{min} for vegetation in regions with longer daylength, indicating strong photoperiodic control of
679 the start of leaf senescence. For vegetation with a given daylength at D_{LCO} longer than 13.5 h, the

positive correlation between D_{LCO} and pre-D_{LCO} T_{min} was slightly stronger in colder areas, suggesting that there is strong selection pressure in harsher temperature environments on the timing of leaf coloration onset and that autumn warming could have a stronger delaying effect on leaf coloration onset in colder areas than in warmer areas. This study suggests that autumnal warming will not change the start date of leaf senescence, but it might slow the rate of senescence. A slower senescence speed possibly could extend the period of senescence and provide more time to reallocate nutrients and prepare for overwintering. Such changes could substantially affect carbon and nutrient cycles. Our study provides a foundation for understanding the complex relationships among nutrient cycling, vegetation growth, energy exchange, and climate change in autumn in temperate and boreal regions dominated by winter deciduous vegetation.

Data Availability

All data used for this study are publicly available online. The satellite reflectance products at 0.05-degree resolution (MOD09CMG) used to estimate phenological metrics and the global land cover map (MCD12C1-2009) used to identify natural vegetation are freely available online at https://ladsweb.modaps.eosdis.nasa.gov. The PhenoCam data (PhenoCam Dataset V2.0) used to evaluate the satellite-derived phenological metrics are available at https://doi.org/10.3334/ORNLDAAC/1674, and the subsets of satellite reflectance products at 500-meter resolution (MOD09A1) at PhenoCam sites are downloaded from https://modis.ornl.gov/globalsubset/. The climatic data of region are publicly available: CRU TS 4.03 monthly climatic data are available via http://data.ceda.ac.uk and CRU-NCEP 7.2 6-hourly climatic data are available via https://vesg.ipsl.upmc.fr. In situ phenological observations in China are available from the National Earth System Science Data Sharing Infrastructure, National Science and Technology Infrastructure of China (http://www.geodata.cn). The climatic data of in situ observations in China are available from National Meteorological Information Center (http://data.tpdc.ac.cn). The site-based gross primary productivity products used to estimate phenological metrics and the corresponding half-hourly climatic data are extracted from the FLUXNET2015 Dataset (http://fluxnet.fluxdata.org/data/fluxnet2015-dataset/). The source code of the Spatial-Temporal Savitzky-Golay filter is available at https://github.com/cao-

sre/STSG_IDL_program. The codes for analyses are available from figshare (https://figshare.com/s/be760555bb74ef0e6bf2).

References

Bauerle, W. L., Oren, R., Way, D. A., Qian, S. S., Stoy, P. C., Thornton, P. E., ... Reynolds, R. F. (2012). Photoperiodic regulation of the seasonal pattern of photosynthetic capacity and the implications for carbon cycling. *Proceedings of the National Academy of Sciences, 109*(22), 8612-8617. doi:10.1073/pnas.1119131109

Beck, P. S. A., Atzberger, C., Høgda, K. A., Johansen, B., & Skidmore, A. K. (2006). Improved monitoring of vegetation dynamics at very high latitudes: A new method using MODIS NDVI. *Remote Sensing of Environment, 100*(3), 321-334. doi:10.1016/j.rse.2005.10.021

Berman, E. E., Graves, T. A., Mikle, N. L., Merkle, J. A., Johnston, A. N., & Chong, G. W. (2020). Comparative Quality and Trend of Remotely Sensed Phenology and Productivity Metrics across the Western United States. *Remote Sensing, 12*(16). doi:10.3390/rs12162538

Borthwick, H. A., & Hendricks, S. B. (1960). Photoperiodism in Plants. *Science, 132*(3435), 1223-1228. doi:10.1126/science.132.3435.1223

Buitenwerf, R., Rose, L., & Higgins, S. I. (2015). Three decades of multi-dimensional change in global leaf phenology. *Nature Climate Change, 5*(4), 364-368. doi:10.1038/nclimate2533

Cao, R., Chen, Y., Shen, M., Chen, J., Zhou, J., Wang, C., & Yang, W. (2018). A simple method to improve the quality of NDVI time-series data by integrating spatiotemporal information with the Savitzky-Golay filter. *Remote Sensing of Environment, 217*, 244-257. doi:https://doi.org/10.1016/j.rse.2018.08.022

Chen, J., Rao, Y., Shen, M., Wang, C., Zhou, Y., Ma, L., ... Yang, X. (2016). A simple method for detecting phenological change from time series of vegetation index. *IEEE Transactions on Geoscience and Remote Sensing, 54*(6), 3436-3449. doi:10.1109/TGRS.2016.2518167

China Meteorological Administration. (1993). *Observation criterion of agricultural meteorology*: China Meteorological Press, Beijing (in Chinese).

Cong, N., Shen, M., & Piao, S. (2017). Spatial variations in responses of vegetation autumn phenology to climate change on the Tibetan Plateau. *Journal of Plant Ecology*. doi:10.1093/jpe/rtw084

739 Delpierre, N., Dufrêne, E., Soudani, K., Ulrich, E., Cecchini, S., Boé, J., & François, C. (2009).
740 Modelling interannual and spatial variability of leaf senescence for three deciduous tree
741 species in France. *Agricultural and Forest Meteorology, 149*(6), 938-948.
742 doi:https://doi.org/10.1016/j.agrformet.2008.11.014
743 Elmore, A. J., Guinn, S. M., Minsley, B. J., & Richardson, A. D. (2012). Landscape controls on
744 the timing of spring, autumn, and growing season length in mid-Atlantic forests. *Global*
745 *Change Biology, 18*(2), 656-674. doi:10.1111/j.1365-2486.2011.02521.x
746 Estiarte, M., & Peñuelas, J. (2015). Alteration of the phenology of leaf senescence and fall in
747 winter deciduous species by climate change: effects on nutrient proficiency. *Global*
748 *Change Biology, 21*(3), 1005-1017. doi:10.1111/gcb.12804
749 Estrella, N., & Menzel, A. (2006). Responses of leaf colouring in four deciduous tree species to
750 climate and weather in Germany. *Climate Research, 32*(3), 253-267.
751 Ford, K. R., Harrington, C. A., & Clair, J. B. S. (2017). Photoperiod cues and patterns of genetic
752 variation limit phenological responses to climate change in warm parts of species' range:
753 Modeling diameter-growth cessation in coast Douglas-fir. *Global Change Biology, 23*(8),
754 3348-3362. doi:10.1111/gcb.13690
755 Fracheboud, Y., Luquez, V., Björkén, L., Sjödin, A., Tuominen, H., & Jansson, S. (2009). The
756 control of autumn senescence in European aspen. *Plant Physiology, 149*(4), 1982-1991.
757 doi:10.1104/pp.108.133249
758 Friedl, M., & Sulla-Menashe, D. (2015). MCD12C1 MODIS/Terra+Aqua Land Cover Type
759 Yearly L3 Global 0.05Deg CMG V006 In *NASA EOSDIS Land Processes DAAC.*
760 *http://doi.org/10.5067/MODIS/MCD12C1.006*.
761 Fu, Y. H., Zhang, X., Piao, S., Hao, F., Geng, X., Vitasse, Y., ... Janssens, I. A. (2019). Daylength
762 helps temperate deciduous trees to leaf-out at the optimal time. *Global Change Biology,*
763 *25*(7), 2410-2418. doi:https://doi.org/10.1111/gcb.14633
764 Fu, Y. H., Zhao, H., Piao, S., Peaucelle, M., Peng, S., Zhou, G., ... Janssens, I. A. (2015). Declining
765 global warming effects on the phenology of spring leaf unfolding. *Nature, 526*(7571), 104-
766 107. doi:https://doi.org/10.1038/nature15402
767 Fu, Y. S. H., Campioli, M., Vitasse, Y., De Boeck, H. J., Van den Berge, J., AbdElgawad, H., ...
768 Janssens, I. A. (2014). Variation in leaf flushing date influences autumnal senescence and

769 next year's flushing date in two temperate tree species. *Proceedings of the National*
770 *Academy of Sciences, 111*(20), 7355-7360. doi:10.1073/pnas.1321727111
771 Gan, S. S., & Amasino, R. M. (1997). Making sense of senescence - Molecular genetic regulation
772 and manipulation of leaf senescence. *Plant Physiology, 113*(2), 313-319. doi:DOI
773 10.1104/pp.113.2.313
774 Ganguly, S., Friedl, M. A., Tan, B., Zhang, X., & Verma, M. (2010). Land surface phenology from
775 MODIS: Characterization of the Collection 5 global land cover dynamics product. *Remote*
776 *Sensing of Environment, 114*(8), 1805-1816. doi:https://doi.org/10.1016/j.rse.2010.04.005
777 Gao, M., Piao, S., Chen, A., Yang, H., Liu, Q., Fu, Y. H., & Janssens, I. A. (2019). Divergent
778 changes in the elevational gradient of vegetation activities over the last 30 years. *Nat*
779 *Commun, 10*(1), 2970. doi:10.1038/s41467-019-11035-w
780 Garonna, I., De Jong, R., De Wit, A. J. W., Mücher, C. A., Schmid, B., & Schaepman, M. E. (2014).
781 Strong contribution of autumn phenology to changes in satellite-derived growing season
782 length estimates across Europe (1982-2011). *Global Change Biology, 20*(11), 3457-3470.
783 Ge, Q. S., Wang, H. J., Rutishauser, T., & Dai, J. H. (2015). Phenological response to climate
784 change in China: a meta-analysis. *Global Change Biology, 21*(1), 265-274.
785 Gill, A. L., Gallinat, A. S., Sanders-DeMott, R., Rigden, A. J., Short Gianotti, D. J., Mantooth, J.
786 A., & Templer, P. H. (2015). Changes in autumn senescence in northern hemisphere
787 deciduous trees: a meta-analysis of autumn phenology studies. *Annals of Botany, 116*(6),
788 875-888. doi:10.1093/aob/mcv055
789 Gu, L., Post, W. M., Baldocchi, D. D., Black, T. A., Suyker, A. E., Verma, S. B., ... Wofsy, S. C.
790 (2009). Characterizing the seasonal dynamics of plant community photosynthesis across
791 a range of vegetation types. In A. Noormets (Ed.), *Phenology of Ecosystem Processes* (pp.
792 35-58): Springer, New York, NY.
793 Hamner, K. C. (1940). Interrelation of light and darkness in photoperiod. *Botanical Gazette,*
794 *101*(3), 658-687.
795 Harris, I., Jones, P. D., Osborn, T. J., & Lister, D. H. (2014). Updated high-resolution grids of
796 monthly climatic observations – the CRU TS3.10 Dataset. *International Journal of*
797 *Climatology, 34*(3), 623-642. doi:10.1002/joc.3711
798 Howe, G. T., Hackett, W. P., Furnier, G. R., & Klevorn, R. E. (1995). Photoperiodic Responses of

799 a Northern and Southern Ecotype of Black Cottonwood. *Physiologia Plantarum, 93*(4),
800 695-708.
801 Jeganathan, C., Dash, J., & Atkinson, P. M. (2014). Remotely sensed trends in the phenology of
802 northern high latitude terrestrial vegetation, controlling for land cover change and
803 vegetation type. *Remote Sensing of Environment, 143*, 154-170.
804 doi:10.1016/j.rse.2013.11.020
805 Jeong, S. J., Ho, C. H., Gim, H. J., & Brown, M. E. (2011). Phenology shifts at start vs. end of
806 growing season in temperate vegetation over the Northern Hemisphere for the period
807 1982–2008. *Global Change Biology, 17*(7), 2385-2399.
808 Keenan, T. F., Gray, J., Friedl, M. A., Toomey, M., Bohrer, G., Hollinger, D. Y., ... Richardson, A.
809 D. (2014). Net carbon uptake has increased through warming-induced changes in
810 temperate forest phenology. *Nature Climate Change, 4*(7), 598-604.
811 doi:10.1038/nclimate2253
812 Keenan, T. F., & Richardson, A. D. (2015). The timing of autumn senescence is affected by the
813 timing of spring phenology: implications for predictive models. *Global Change Biology,*
814 *21*(7), 2634-2641. doi:10.1111/gcb.12890
815 Keskitalo, J., Bergquist, G., Gardeström, P., & Jansson, S. (2005). A cellular timetable of autumn
816 senescence. *Plant Physiol, 139*(4), 1635-1648. doi:10.1104/pp.105.066845
817 Klosterman, S., & Richardson, A. D. (2017). Observing Spring and Fall Phenology in a Deciduous
818 Forest with Aerial Drone Imagery. *Sensors (Basel), 17*(12). doi:10.3390/s17122852
819 Klosterman, S. T., Hufkens, K., Gray, J. M., Melaas, E., Sonnentag, O., Lavine, I., ... Richardson,
820 A. D. (2014). Evaluating remote sensing of deciduous forest phenology at multiple spatial
821 scales using PhenoCam imagery. *Biogeosciences, 11*(16), 4305-4320. doi:
822 https://doi.org/10.5194/bg-11-4305-2014
823 Körner, C. (2007). Significance of temperature in plant life. In J. I. L. Morison & M. D. Morecroft
824 (Eds.), *Plant Growth and Climate Change* (pp. 48-69).
825 Körner, C. (2021). *Alpine Plant Life: Functional Plant Ecology of High Mountain Ecosystems*.
826 Cham: Springer International Publishing.
827 Körner, C., & Basler, D. (2010). Response-warming, photoperiods, and tree phenology. *Science,*
828 *329*(5989), 278-278. doi:10.1126/science.329.5989.278

Körner, C., & Hiltbrunner, E. (2018). The 90 ways to describe plant temperature. *Perspectives in Plant Ecology, Evolution and Systematics, 30*, 16-21. doi:https://doi.org/10.1016/j.ppees.2017.04.004

Leblans, N. I. W., Sigurdsson, B. D., Vicca, S., Fu, Y. S., Penuelas, J., & Janssens, I. A. (2017). Phenological responses of Icelandic subarctic grasslands to short-term and long-term natural soil warming. *Global Change Biology, 23*(11), 4932-4945.

Lenz, A., Hoch, G., Vitasse, Y., & Körner, C. (2013). European deciduous trees exhibit similar safety margins against damage by spring freeze events along elevational gradients. *New Phytologist, 200*(4), 1166-1175. doi:10.1111/nph.12452

Lim, P. O., Kim, H. J., & Nam, H. G. (2007). Leaf Senescence. *Annual Review of Plant Biology, 58*, 115-136. doi:1543-5008/07/0602-0115$20.00

Liu, Q., Fu, Y. H., Zhu, Z., Liu, Y., Liu, Z., Huang, M., ... Piao, S. (2016). Delayed autumn phenology in the Northern Hemisphere is related to change in both climate and spring phenology. *Global Change Biology, 22*(11), 3702-3711.

Liu, Q., Piao, S., Janssens, I. A., Fu, Y., Peng, S., Lian, X., ... Wang, T. (2018). Extension of the growing season increases vegetation exposure to frost. *Nature Communications, 9*(1), 426. doi:10.1038/s41467-017-02690-y

Lukasová, V., Bucha, T., Škvareninová, J., & Škvarenina, J. (2019). Validation and Application of European Beech Phenological Metrics Derived from MODIS Data along an Altitudinal Gradient. *Forests, 10*(1), 60.

Mariën, B., Balzarolo, M., Dox, I., Leys, S., Lorène, M. J., Geron, C., ... Campioli, M. (2019). Detecting the onset of autumn leaf senescence in deciduous forest trees of the temperate zone. *New Phytologist, 224*(1), 166-176.

Matsumoto, K., Ohta, T., Irasawa, M., & Nakamura, T. (2003). Climate change and extension of the *Ginkgo biloba* L. growing season in Japan: CLIMATE CHANGE AND EXTENSION. *Global Change Biology, 9*(11), 1634-1642. doi:10.1046/j.1365-2486.2003.00688.x

Melaas, E. K., Friedl, M. A., & Zhu, Z. (2013). Detecting interannual variation in deciduous broadleaf forest phenology using Landsat TM/ETM+ data. *Remote Sensing of Environment, 132*, 176-185. doi:https://doi.org/10.1016/j.rse.2013.01.011

Menzel, A., Yuan, Y., Matiu, M., Sparks, T., Scheifinger, H., Gehrig, R., & Estrella, N. (2020).

Climate change fingerprints in recent European plant phenology. *Global Change Biology, 26*(4), 2599-2612. doi:https://doi.org/10.1111/gcb.15000

Morisette, J. T., Richardson, A. D., Knapp, A. K., Fisher, J. I., Graham, E. A., Abatzoglou, J., ... Liang, L. (2009). Tracking the rhythm of the seasons in the face of global change: phenological research in the 21st century. *Frontiers in Ecology and the Environment, 7*(5), 253-260. doi:10.1890/070217

Myneni, R. B., Keeling, C. D., Tucker, C. J., Asrar, G., & Nemani, R. R. (1997). Increased plant growth in the northern high latitudes from 1981 to 1991. *Nature, 386*(6626), 698-702. doi:10.1038/386698a0

Nagai, S., Nasahara, K. N., Muraoka, H., Akiyama, T., & Tsuchida, S. (2010). Field experiments to test the use of the normalized-difference vegetation index for phenology detection. *Agricultural and Forest Meteorology, 150*(2), 152-160. doi:https://doi.org/10.1016/j.agrformet.2009.09.010

Nezval, O., Krejza, J., Světlík, J., Šigut, L., & Horáček, P. (2020). Comparison of traditional ground-based observations and digital remote sensing of phenological transitions in a floodplain forest. *Agricultural and Forest Meteorology, 291*. doi:10.1016/j.agrformet.2020.108079

Pastorello, G. Z., Papale, D., Chu, H., Trotta, C., Agarwal, D. A., Canfora, E., ... Torn, M. S. (2017). A new data set to keep a sharper eye on land-air exchanges. *Eos*. Retrieved from https://doi.org/10.1029/2017EO071597 doi:10.1029/2017EO071597

Pau, S., Wolkovich, E. M., Cook, B. I., Davies, T. J., Kraft, N. J. B., Bolmgren, K., ... Cleland, E. E. (2011). Predicting phenology by integrating ecology, evolution and climate science. *Global Change Biology, 17*(12), 3633-3643. doi:10.1111/j.1365-2486.2011.02515.x

Paus, E., Nilsen, J., & Junttila, O. (1986). Bud Dormancy and Vegetative Growth in Salix-Polaris as Affected by Temperature and Photoperiod. *Polar Biology, 6*(2), 91-95.

Peñuelas, J., Rutishauser, T., & Filella, I. (2009). Phenology feedbacks on climate change. *Science, 324*(5929), 887-888. doi:10.1126/science.1173004

Piao, S., Ciais, P., Friedlingstein, P., Peylin, P., Reichstein, M., Luyssaert, S., ... Vesala, T. (2008). Net carbon dioxide losses of northern ecosystems in response to autumn warming. *Nature, 451*(7174), 49-52. doi:10.1038/nature06444

889 Ren, J., Campbell, J., & Shao, Y. (2017). Estimation of SOS and EOS for Midwestern US Corn
890 and Soybean Crops. *Remote Sensing, 9*(7). doi:10.3390/rs9070722
891 Rennenberg, H., Wildhagen, H., & Ehlting, B. (2010). Nitrogen nutrition of poplar trees. *Plant*
892 *Biology, 12*(2), 275-291. doi:10.1111/j.1438-8677.2009.00309.x
893 Richardson, A. D., Hufkens, K., Milliman, T., & Frolking, S. (2018). Intercomparison of
894 phenological transition dates derived from the PhenoCam Dataset V1.0 and MODIS
895 satellite remote sensing. *Scientific Reports, 8*.
896 Richardson, A. D., Keenan, T. F., Migliavacca, M., Ryu, Y., Sonnentag, O., & Toomey, M. (2013).
897 Climate change, phenology, and phenological control of vegetation feedbacks to the
898 climate system. *Agricultural and Forest Meteorology, 169*, 156-173.
899 doi:https://doi.org/10.1016/j.agrformet.2012.09.012
900 Saikkonen, K., Taulavuori, K., Hyvönen, T., Gundel, P. E., Hamilton, C. E., Vänninen, I., ...
901 Helander, M. (2012). Climate change-driven species' range shifts filtered by
902 photoperiodism. *Nature Climate Change, 2*(4), 239-242. doi:10.1038/nclimate1430
903 Sakai, A., & Larcher, W. (1987). *Frost Survival of Plants* (Vol. 62). Berlin, Heidelberg: Springer
904 Berlin Heidelberg.
905 Sen, P. K. (1968). Estimates of the Regression Coefficient Based on Kendall's Tau. *Journal of the*
906 *American Statistical Association, 63*(324), 1379-1389.
907 doi:10.1080/01621459.1968.10480934
908 Seyednasrollah, B., Young, A. M., Hufkens, K., Milliman, T., Friedl, M. A., Frolking, S., &
909 Richardson, A. D. (2019). Tracking vegetation phenology across diverse biomes using
910 Version 2.0 of the PhenoCam Dataset. *Sci Data, 6*(1), 222. doi:10.1038/s41597-019-0229-
911 9
912 Seyednasrollah, B., Young, A. M., Hufkens, K., Milliman, T., Friedl, M. A., Frolking, S., ... Zona,
913 D. (2019). PhenoCam Dataset v2.0: Vegetation Phenology from Digital Camera Imagery,
914 2000-2018. In: ORNL Distributed Active Archive Center.
915 Shang, R., Liu, R., Xu, M., Liu, Y., Zuo, L., & Ge, Q. (2017). The relationship between threshold-
916 based and inflexion-based approaches for extraction of land surface phenology. *Remote*
917 *Sensing of Environment, 199*, 167-170. doi:10.1016/j.rse.2017.07.020
918 Shen, M., Jiang, N., Peng, D., Rao, Y., Huang, Y., Fu, Y. H., ... Tang, Y. (2020). Can changes in

autumn phenology facilitate earlier green-up date of northern vegetation? *Agricultural and Forest Meteorology, 291*. doi:10.1016/j.agrformet.2020.108077

Shen, M., Tang, Y., Desai, A. R., Gough, C., & Chen, J. (2014). Can EVI-derived land-surface phenology be used as a surrogate for phenology of canopy photosynthesis? *International Journal of Remote Sensing, 35*(3), 1162-1174. doi:https://doi.org/10.1080/01431161.2013.875636

Shen, M., Zhang, G., Cong, N., Wang, S., Kong, W., & Piao, S. (2014). Increasing altitudinal gradient of spring vegetation phenology during the last decade on the Qinghai–Tibetan Plateau. *Agricultural and Forest Meteorology, 189-190*, 71-80. doi:10.1016/j.agrformet.2014.01.003

Shen, M. G., Piao, S. L., Jeong, S. J., Zhou, L. M., Zeng, Z. Z., Ciais, P., ... Yao, T. D. (2015). Evaporative cooling over the Tibetan Plateau induced by vegetation growth. *Proceedings of the National Academy of Sciences, 112*(30), 9299-9304. doi:https://doi.org/10.1073/pnas.1504418112

Soudani, K., Delpierre, N., Berveiller, D., Hmimina, G., & Dufrêne, R. (2021). A survey of proximal methods for monitoring leaf phenology in temperate deciduous forests. *Biogeosciences, 18*(11), 3391-3408.

Soudani, K., Hmimina, G., Delpierre, N., Pontailler, J. Y., Aubinet, M., Bonal, D., ... Dufrêne, E. (2012). Ground-based Network of NDVI measurements for tracking temporal dynamics of canopy structure and vegetation phenology in different biomes. *Remote Sensing of Environment, 123*, 234-245. doi:10.1016/j.rse.2012.03.012

Stinziano, J. R., & Way, D. A. (2017). Autumn photosynthetic decline and growth cessation in seedlings of white spruce are decoupled under warming and photoperiod manipulations. *Plant Cell and Environment, 40*(8), 1296-1316. doi:10.1111/pce.12917

Tang, J., Körner , C., Muraoka, H., Piao, S., Shen, M., Thackeray, S. J., & Yang, X. (2016). Emerging opportunities and challenges in phenology: a review. *Ecosphere, 7*(8), e01436.

Taschler, D., & Neuner, G. (2004). Summer frost resistance and freezing patterns measured in situ in leaves of major alpine plant growth forms in relation to their upper distribution boundary. *Plant, Cell and Environment, 27*(6), 737-746. doi:10.1111/j.1365-3040.2004.01176.x

Theil, H. (1992). A rank-invariant method of linear and polynomial regression analysis. In B. Raj

949 & J. Koerts (Eds.), *Henri Theil's Contributions to Economics and Econometrics: Econometric Theory and Methodology* (Vol. 23, pp. 345-381). Dordrecht: Springer Netherlands.
952 Thomas, H., & Stoddart, J. L. (1980). Leaf Senescence. *Annual Review of Plant Physiology and Plant Molecular Biology, 31*, 83-111. doi:DOI 10.1146/annurev.pp.31.060180.000503
954 Vermote, E. F. (2015). MOD09CMG MODIS/Terra Surface Reflectance Daily L3 Global 0.05Deg CMG V006. In *NASA EOSDIS Land Processes DAAC*.
956 Viovy, N. (2018). CRUNCEP Version 7 - Atmospheric Forcing Data for the Community Land Model. In *Research Data Archive at the National Center for Atmospheric Research, Computational and Information Systems Laboratory*. Boulder CO.
959 White, M. A., Thornton, P. E., & Running, S. W. (1997). A continental phenology model for monitoring vegetation responses to interannual climatic variability. *Global Biogeochemical Cycles, 11*(2), 217-234. doi:https://doi.org/10.1029/97gb00330
962 Wingate, L., Ogée, J., Cremonese, E., Filippa, G., Mizunuma, T., Migliavacca, M., ... Grace, J. (2015). Interpreting canopy development and physiology using a European phenology camera network at flux sites. *Biogeosciences, 12*(20), 5995-6015. doi:10.5194/bg-12-5995-2015
966 Wu, C., Wang, X., Wang, H., Ciais, P., Peñuelas, J., Myneni, R. B., ... Ge, Q. (2018). Contrasting responses of autumn-leaf senescence to daytime and night-time warming. *Nature Climate Change, 8*(12), 1092-1096. doi:10.1038/s41558-018-0346-z
969 Xu, C., Liu, H., Williams, A. P., Yin, Y., & Wu, X. (2016). Trends toward an earlier peak of the growing season in Northern Hemisphere mid-latitudes. *Global Change Biology, 22*(8), 2852-2860. doi:10.1111/gcb.13224
972 Yang, X., Tang, J., & Mustard, J. F. (2014). Beyond leaf color: Comparing camera-based phenological metrics with leaf biochemical, biophysical, and spectral properties throughout the growing season of a temperate deciduous forest. *Journal of Geophysical Research: Biogeosciences, 119*(3), 181-191. doi:10.1002/2013jg002460
976 Ye, Y., & Zhang, X. (2021). Exploration of global spatiotemporal changes of fall foliage coloration in deciduous forests and shrubs using the VIIRS land surface phenology product. *Science of Remote Sensing, 4*. doi:10.1016/j.srs.2021.100030

Yu, H., Luedeling, E., & Xu, J. (2010). Winter and spring warming result in delayed spring phenology on the Tibetan Plateau. *Proceedings of the National Academy of Sciences, 107*(51), 22151-22156. doi:https://doi.org/10.1073/pnas.1012490107

Zhang, X. (2015). Reconstruction of a complete global time series of daily vegetation index trajectory from long-term AVHRR data. *Remote Sensing of Environment, 156*, 457-472. doi:10.1016/j.rse.2014.10.012

Zhang, X., Friedl, M. A., Schaaf, C. B., Strahler, A. H., Hodges, J. C., Gao, F., ... Huete, A. (2003). Monitoring vegetation phenology using MODIS. *Remote Sensing of Environment, 84*(3), 471-475.

Zhang, X., Tarpley, D., & Sullivan, J. T. (2007). Diverse responses of vegetation phenology to a warming climate. *Geophysical Research Letters, 34*(19). doi:https://doi.org/10.1029/2007gl031447

Zhao, B., Donnelly, A., & Schwartz, M. D. (2020). Evaluating autumn phenology derived from field observations, satellite data, and carbon flux measurements in a northern mixed forest, USA. *International Journal of Biometeorology, 64*(5), 713-727. doi:10.1007/s00484-020-01861-9

Zohner, C. M., Benito, B. M., Svenning, J.-C., & Renner, S. S. (2016). Day length unlikely to constrain climate-driven shifts in leaf-out times of northern woody plants. *Nature Climate Change, 6*(12), 1120-1123. doi:10.1038/nclimate3138

SUPPORTING INFORMATION

Additional supporting information may be found in the online version of this article at the publisher's web-site.

Figure S1 Locations of the sites of *in situ* observations used in this study.

Figure S2 Spatial pattern of the length of the pre-D_{LCO} period for mean daily minimum temperature.

Figure S3 Temporal trends in satellite D_{LCO} over the period 2000–2016 before and after the exclusion of years with possible cold events before D_{LCO}.

Figure S4 Temporal trends determined by Theil-Sen estimator in satellite D_{LCO} determined by the threshold-based method and temporal trends in satellite D_{LCO} determined by the inflection-

point-based method.

Figure S5 Temporal trends in satellite D_{LCO} determined by the threshold-based method over the period 2000–2018, considerting possible summer NDVI decline before 1 August.

Figure S6 Temporal trends in satellite D_{LCO} determined by the threshold-based method over the period 2000–2018, considerting possible summer NDVI decline before 16 August.

Figure S7 Temporal trends in satellite D_{LCO} determined by the inflection-point-based method over the period 2000–2018, considerting possible summer NDVI decline.

Figure S8 Percentage of area with significant temporal trends in the timings of different stages of leaf coloration, as retrieved from satellite images.

Figure S9 Spatial pattern of the partial correlation coefficient between satellite D_{LCO} and pre-D_{LCO} total precipitation over the period 2000–2018.

Figure S10 Spatial pattern of the partial correlation coefficient between satellite D_{LCO} and pre-D_{LCO} (1 month preceding the multiyear mean D_{LCO}) mean daily minimum temperature over the period 2000–2018.

Figure S11 Spatial pattern of the partial correlation coefficient between satellite D_{LCO} and pre-D_{LCO} (15 days preceding the multiyear mean D_{LCO}) mean daily minimum temperature over the period 2000–2016.

Figure S12 Spatial pattern of the partial correlation coefficient between satellite D_{LCO} and the lowest daily minimum temperature during the 15 days before the multiyear mean D_{LCO} over the period 2000–2016.

Figure S13 Spatial pattern of the partial correlation coefficient between satellite D_{LCO} and pre-D_{LCO} climatic factors, with green-up onset date as an extra control variable over the period 2000–2018.

Figure S14 Spatial pattern of the partial correlation coefficient between satellite D_{LCO} and pre-D_{LCO} climatic factors over the period 2000–2016 before and after the exclusion of years with possible cold events before D_{LCO}.

Figure S15 Spatial pattern of the partial correlation coefficient between the timing of different stages of leaf coloration and the mean daily minimum temperature for an optimized period preceding each stage over the period 2000–2018.

Figure S16 Spatial pattern of the partial correlation coefficient between the timing of the end of

leaf coloration (D_{LCE}) and pre-D_{LCE} T_{min} over the period 2000–2018.

Figure S17 Impacts of temperature on the timing of different stages of leaf coloration and on the progress of leaf coloration over the period 2000–2018, considerting possible summer NDVI decline before 1 August.

Figure S18 Impacts of temperature on the timing of different stages of leaf coloration and on the progress of leaf coloration over the period 2000–2018, considerting possible summer NDVI decline before 16 August.

Figure S19 Dependence of temporal trends determined by Theil-Sen estimator in satellite D_{LCO} on daylength and temperature at D_{LCO} over the period 2000–2018.

Figure S20 Dependence of temporal trends in satellite D_{LCO}, of the partial correlation coefficient between D_{LCO} and pre-D_{LCO} mean daily minimum temperature, and of the partial correlation coefficient between D_{LCO} and pre-D_{LCO} total precipitation on daylength and temperature at D_{LCO} over the period 2000–2016 after the exclusion of years with possible cold events before D_{LCO}.

Figure S21 Dependence of temporal trends in satellite D_{LCO} and of the partial correlation coefficient between D_{LCO} and pre-D_{LCO} mean daily minimum temperature on daylength and temperature at D_{LCO} over the period 2000–2018, considerting possible summer NDVI decline before 1 August.

Figure S22 Dependence of temporal trends in satellite D_{LCO} and of the partial correlation coefficient between D_{LCO} and pre-D_{LCO} mean daily minimum temperature on daylength and temperature at D_{LCO} over the period 2000–2018, considerting possible summer NDVI decline before 16 August.

Figure S23 Dependence of the partial correlation coefficient between satellite D_{LCO} and pre-D_{LCO} total precipitation on daylength and temperature at D_{LCO} over the period 2000–2018

Table S1 Experiments on photoperiodic control of plant growth.

Table S2 *In situ* observations in China used in this study.

Table S3 FLUXNET2015 flux tower sites used in this study.

Table S4 Percentage of time series for each interval of the temporal trend in D_{LCO} before and after the exclusion of years with cold events.

Table S5 Percentage of time series for each interval of the temporal trend in D_{LCO}.

Table S6 Percentage of correlations between D_{LCO} or D_{PDO} and each climate factor for each interval of the partial correlation coefficient before and after the exclusion of years with cold events.

Table S7 Percentage of correlations between D_{LCO} or D_{PDO} and each climate factor for each interval of the partial correlation coefficient.

Supplementary Method 1. Preparation of high quality 5-day NDVI time series

Supplementary Method 2. Comparison between satellite D_{LCO} and D_{LCO} from PhenoCam dataset

Supplementary Information for

Warming does not delay the start of autumnal leaf coloration but slows its progress rate

This PDF file includes:

Figures S1 to S23
Tables S1 to S7
Supplementary Methods
Supplementary References

Supplementary Figures

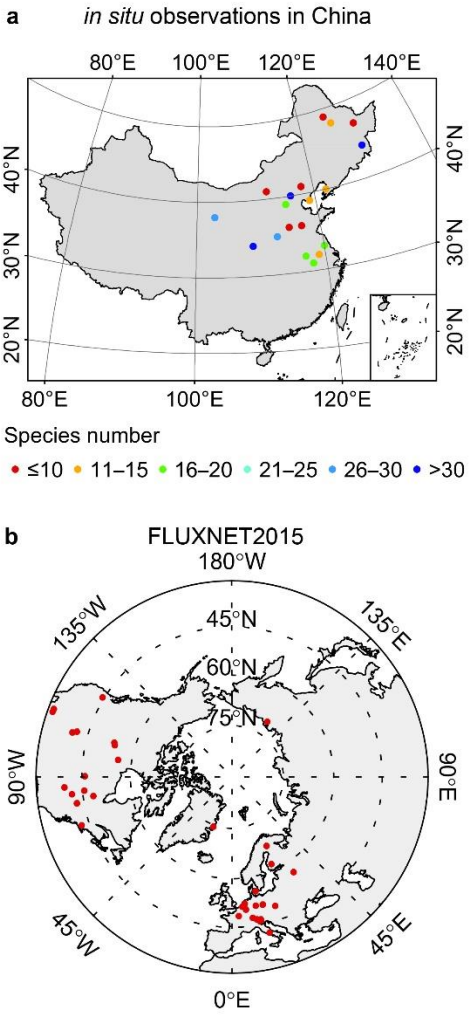

Figure S1. Locations of the sites of *in situ* observations used in this study. (a) phenological observation sites in China. (b) FLUXNET2015 flux tower sites.

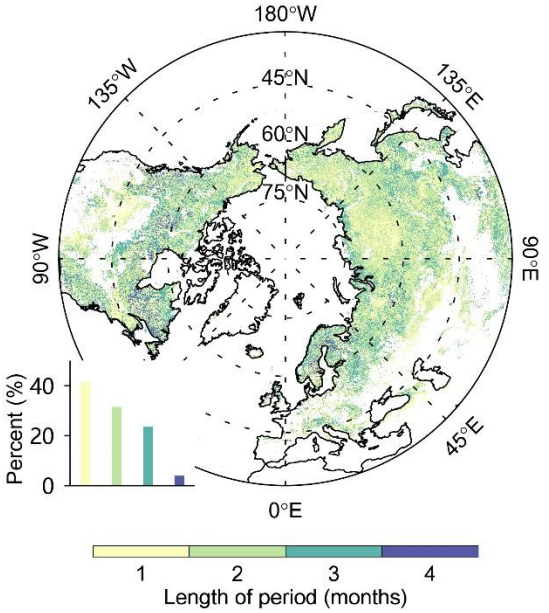

Figure S2. Spatial pattern of the length of the pre-D_{LCO} period for mean daily minimum temperature (T_{min}). The bar chart shows the percentage of area for each interval of the length of the pre-D_{LCO} period, with the length indicated by the color scale at the bottom.

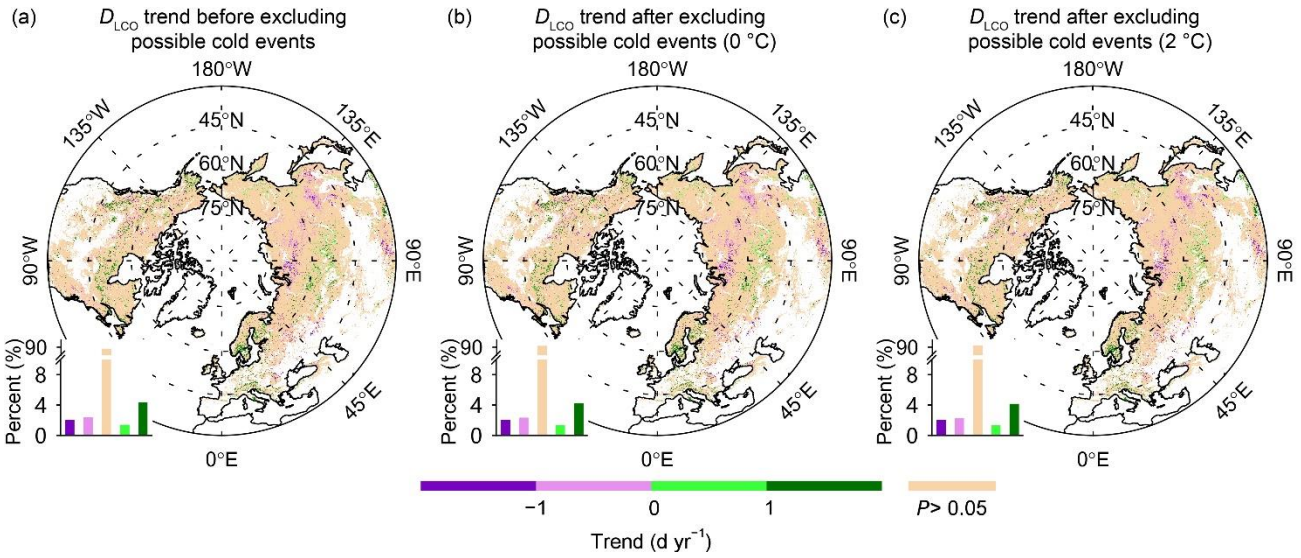

Figure S3. Temporal trends in timing of the onset of leaf coloration (D_{LCO}), retrieved from satellite images over the period 2000–2016 before (a) and after (b and c) the exclusion of years with possible cold events before D_{LCO}. Cold events were determined mainly by using a threshold-based method with daily minimum temperatures of 0 °C (b) or 2 °C (c). The bar chart in each panel shows the percentage of area within each interval of the significant temporal trends and the percentage of area with nonsignificant trends, indicated by the color scale at the bottom. The percentage for each interval of the trend is provided in Table S4. D_{LCO} corresponds to a 10% decrease in NDVI. Significant temporal trends were determined by using *t*-tests at $P < 0.05$ and ordinary least squares regression.

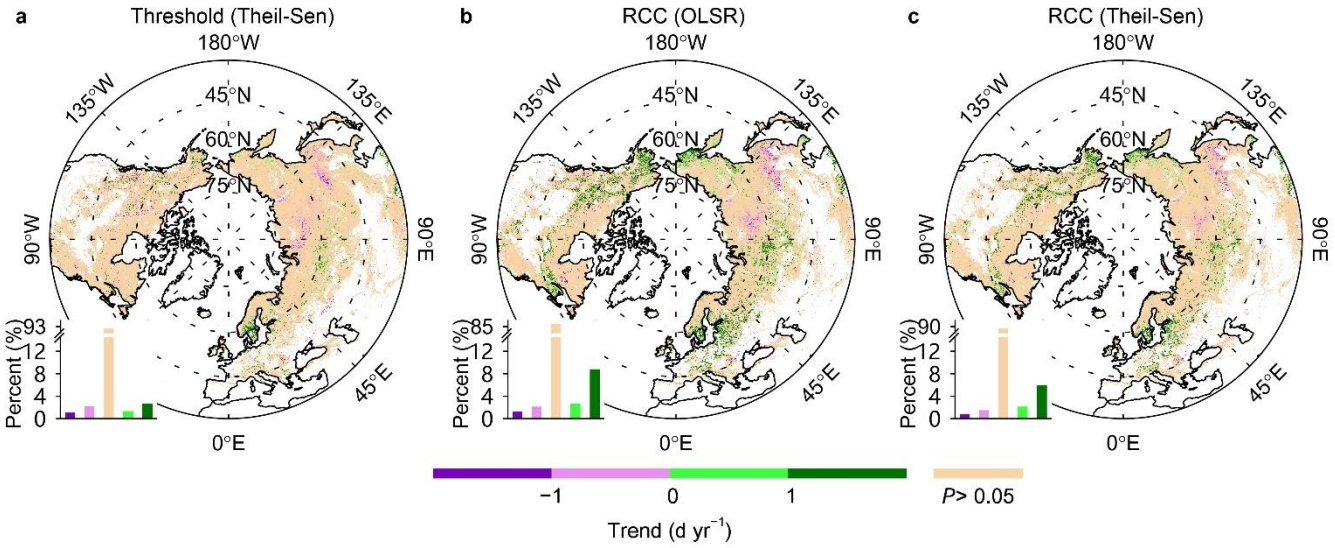

Figure S4. Temporal trends in timing of the onset of leaf coloration (D_{LCO}), retrieved from satellite images over the period 2000–2018. The bar chart in each panel shows the percentage of area within each interval of the significant temporal trends and the percentage of area with nonsignificant trends, indicated by the color scale at the bottom. Positive and negative trend values refer to significantly delayed and advanced D_{LCO}, respectively. D_{LCO} in (a) corresponds to a 10% decrease in NDVI (Threshold). D_{LCO} in (b) and (c) was determined as the date of inflection point when NDVI began to decline (RCC). In (a) and (c), significant temporal trends were determined by using Mann-Kendall tests at $P < 0.05$ and a Theil-Sen estimator; in (b), significant temporal trends were determined by using *t*-tests at $P < 0.05$ and ordinary least squares regression (OLSR).

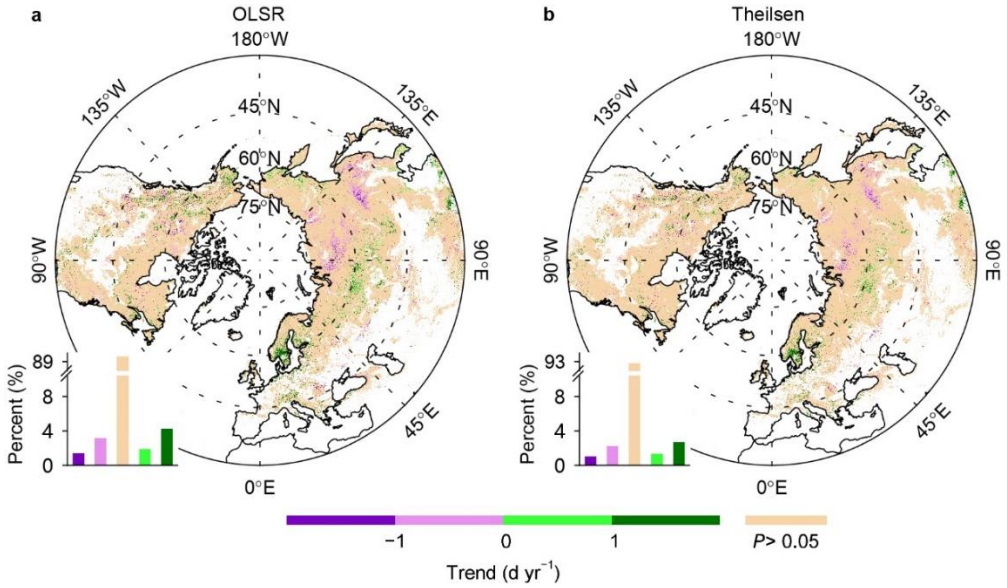

Figure S5. Temporal trends in the timing of onset of leaf coloration (D_{LCO}), retrieved from satellite images for 2000–2018. The bar chart in each panel shows the percentage of area within each interval of the significant temporal trends and the percentage of area with nonsignificant trends, indicated by the color scale at the bottom. Positive and negative trend values refer to significantly delayed and advanced D_{LCO}, respectively. For the pixels identified as deciduous broadleaved forests, D_{LCO} was defined as the date when NDVI decreased by 10% of its annual amplitude from 1 August (see Section 2.4.4 for details). In (a), significant temporal trends were determined by using *t*-tests at $P < 0.05$ and ordinary least squares regression (OLSR). In (b), significant temporal trends were determined by using Mann-Kendall tests at $P < 0.05$ and a Theil-Sen estimator.

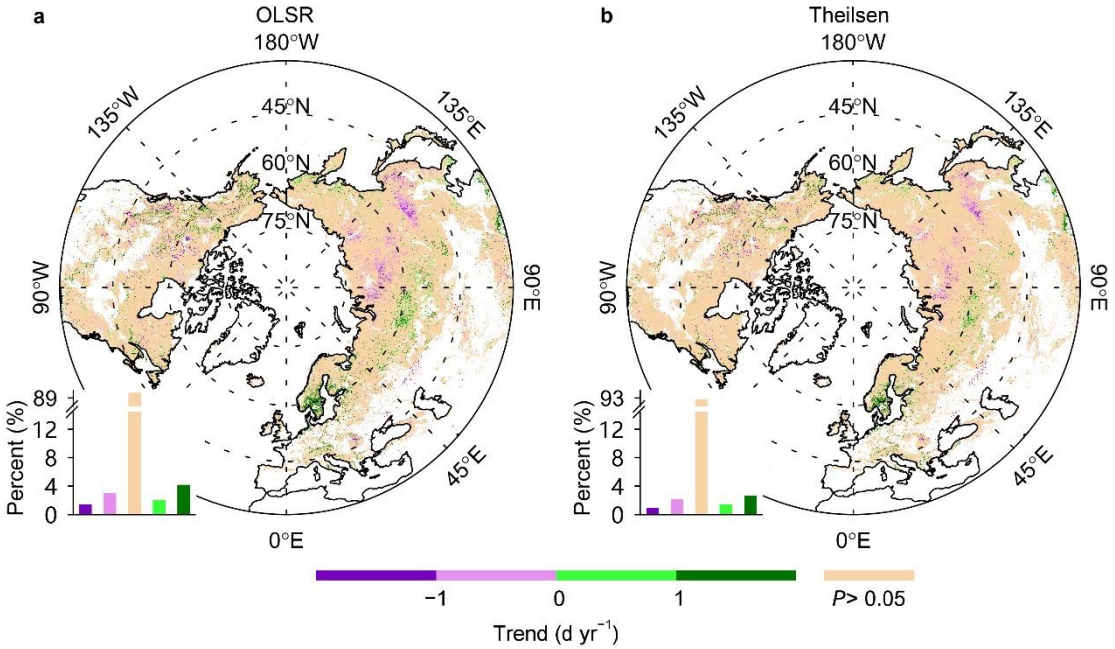

Figure S6. Temporal trends in the timing of onset of leaf coloration (D_{LCO}), as retrieved from satellite images for the period 2000–2018. The bar chart in each panel shows the percentage of area within each interval of the significant temporal trends and the percentage of area with nonsignificant trends, indicated by the color scale at the bottom. Positive and negative trend values refer to significantly delayed and advanced D_{LCO}, respectively. For the pixels identified as deciduous broadleaved forests, D_{LCO} was defined as the date when NDVI decreased by 10% of its annual amplitude from 16 August (see section 2.4.4 for details). In (a), significant temporal trends were determined by using *t*-tests at $P < 0.05$ and ordinary least squares regression (OLSR). In (b), significant temporal trends were determined by using Mann-Kendall tests at $P < 0.05$ and a Theil-Sen estimator.

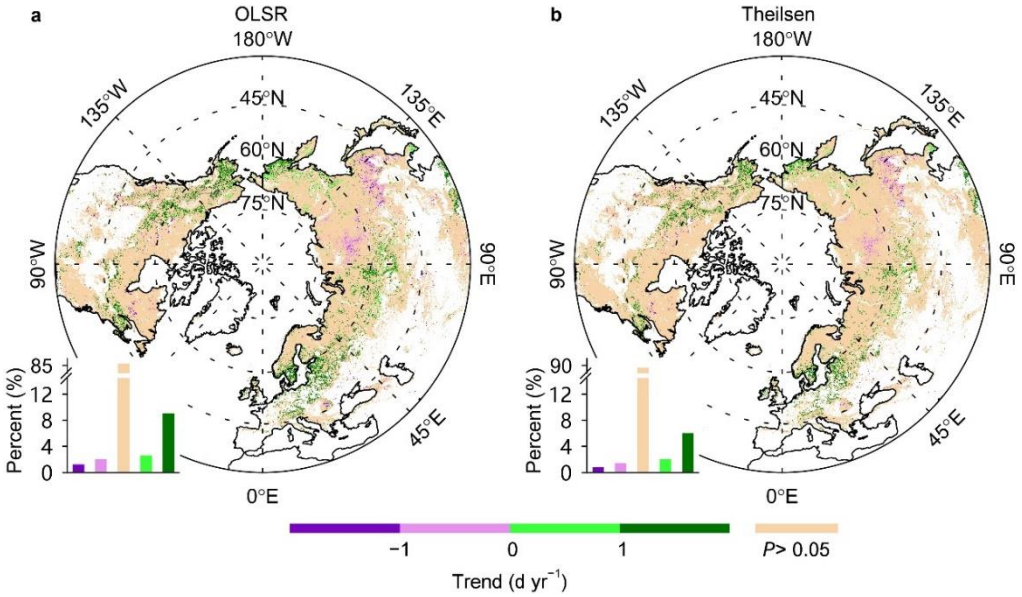

Figure S7. Temporal trends in the timing of onset of leaf coloration (D_{LCO}), as retrieved from satellite images for 2000–2018. The bar chart in each panel shows the percentage of area within each interval of the significant temporal trends and the percentage of area with nonsignificant trends, indicated by the color scale at the bottom. Positive and negative trend values refer to significantly delayed and advanced D_{LCO}, respectively. D_{LCO} was determined as the date of inflection point when NDVI began to drop. For the pixels identified as deciduous broadleaved forests, the fitting function was a modified double logistic function that considered summer NDVI green-down. In (a), significant temporal trends were determined by using *t*-tests at $P < 0.05$ and ordinary least squares regression (OLSR). In (b), significant temporal trends were determined by using Mann-Kendall tests at $P < 0.05$ and a Theil-Sen estimator.

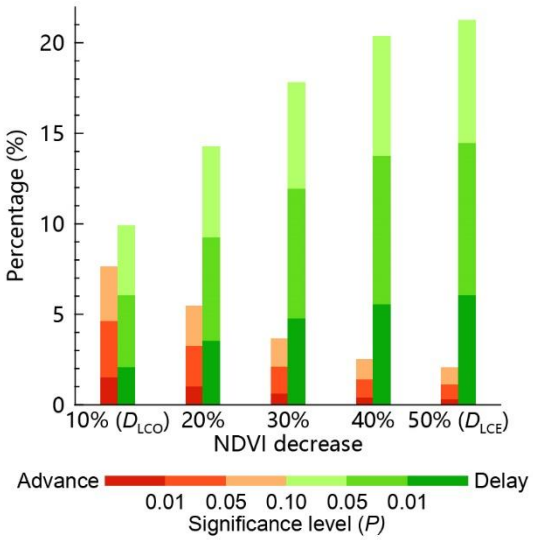

Figure S8. Percentage of area with significant temporal trends in the timing of different stages of leaf coloration, as retrieved from satellite images. Significance levels of the temporal trends were determined by using *t*-tests for ordinary least squares regression over the period 2000–2018 at middle and high northern latitudes (30°N–75°N). The timings of the different stages of leaf coloration were defined as the dates when NDVI decreased by 10% (i.e., D_{LCO}), 20%, 30%, 40%, or 50% (i.e., D_{LCE}) of its annual amplitude in autumn.

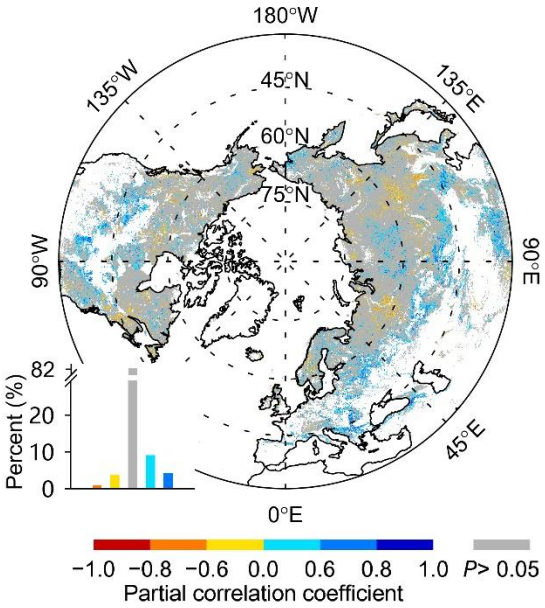

Figure S9. Spatial pattern of the partial correlation coefficient between the timing of onset of leaf coloration (D_{LCO}) and pre-D_{LCO} total precipitation over the period 2000–2018. The bar chart in the bottom-left corner shows the percentage of area for each interval of the partial correlation coefficient, with the coefficient values indicated by the color scale at the bottom.

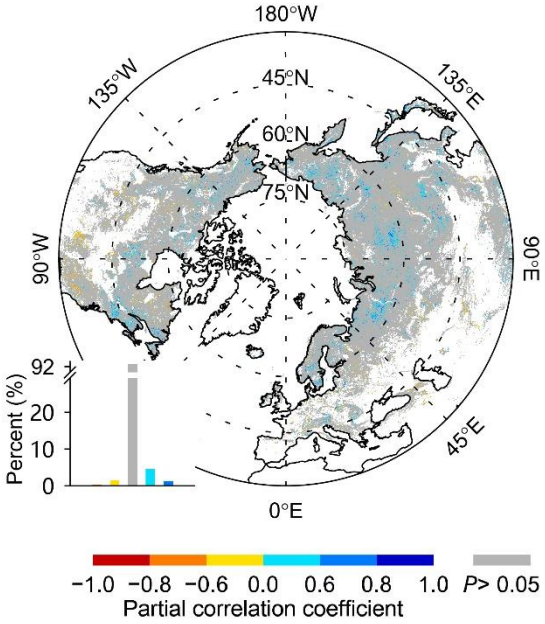

Figure S10. Spatial pattern of the partial correlation coefficient between the timing of onset of leaf coloration (D_{LCO}) and pre-D_{LCO} (1 month preceding the multiyear mean D_{LCO}) mean daily minimum temperature over the period 2000–2018. The bar chart in each panel shows the percentage of area for each interval of the partial correlation coefficient, with the coefficient value indicated by the color scale at the bottom. Non-significant correlations ($P > 0.05$) are in gray.

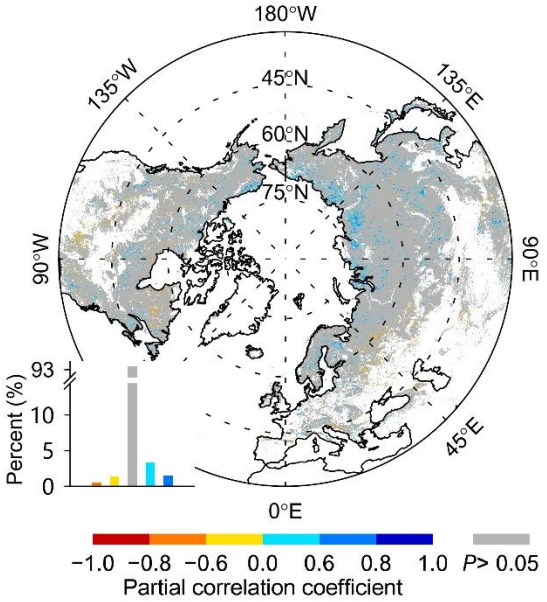

Figure S11. Spatial pattern of the partial correlation coefficient between the timing of onset of leaf coloration (D_{LCO}) and pre-D_{LCO} (15 days preceding the multiyear mean D_{LCO}) mean daily minimum temperature while controlling for the corresponding total precipitation over the period 2000–2016. The bar chart shows the percentage of area for each interval of partial correlation coefficient, with the coefficient value indicated by the color scale at the bottom. Non-significant correlations ($P > 0.05$) are in gray.

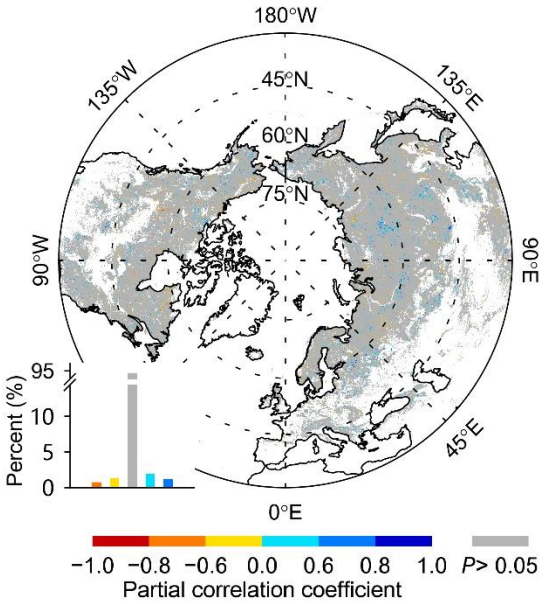

Figure S12. Spatial pattern of the partial correlation coefficient between the timing of the onset of leaf coloration (D_{LCO}) and the lowest daily minimum temperature (T_{min}) during the 15 days before the multiyear mean D_{LCO}, with the concurrent mean T_{min} and total precipitation as control variables over the period 2000–2016. The bar chart shows the percentage of area for each interval of the partial correlation coefficient ($P < 0.05$), with the coefficient indicated by the color scale at the bottom. Non-significant correlations ($P > 0.05$) are in gray.

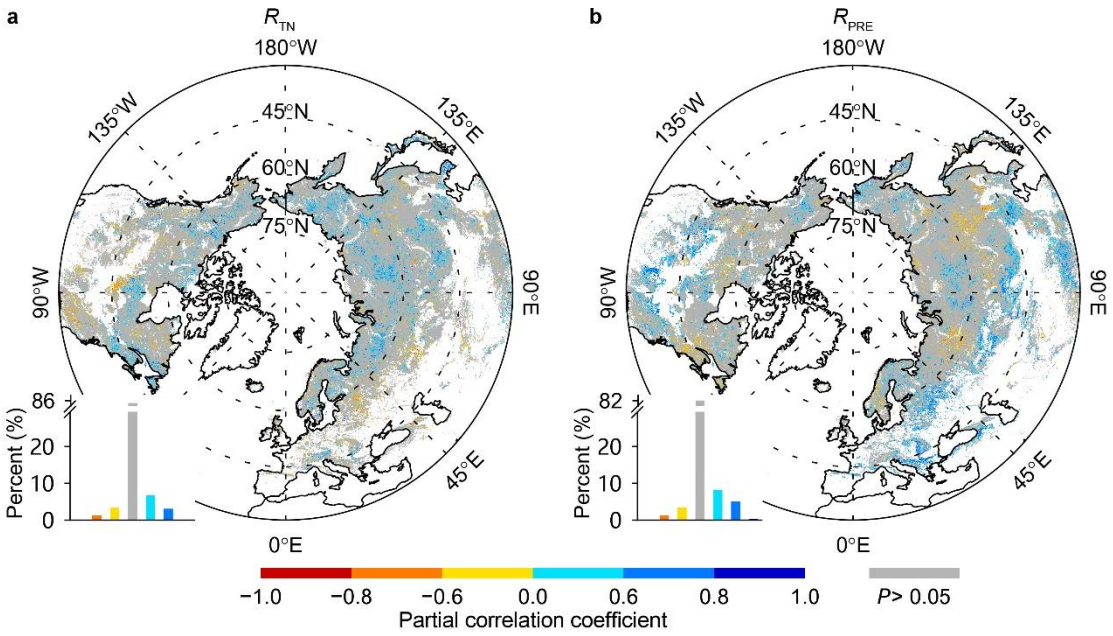

Figure S13. Spatial pattern of the partial correlation coefficient between the timing of onset of leaf coloration (D_{LCO}) and pre-D_{LCO} climatic factors, with green-up onset date as an extra control variable over the period 2000–2018. a, Spatial pattern of the partial correlation coefficient (R_{TN}) between D_{LCO} and pre-D_{LCO} mean daily minimum temperature (T_{min}) while controlling for the corresponding total precipitation and green-up onset date. b, Spatial pattern of the partial correlation coefficient (R_{PRE}) between D_{LCO} and pre-D_{LCO} total precipitation while controlling for the corresponding T_{min} and green-up onset date. The bar chart in each panel shows the percentage of area for each interval of the partial correlation coefficient, with the coefficient value indicated by the color scale at the bottom. Non-significant correlations ($P > 0.05$) are in gray.

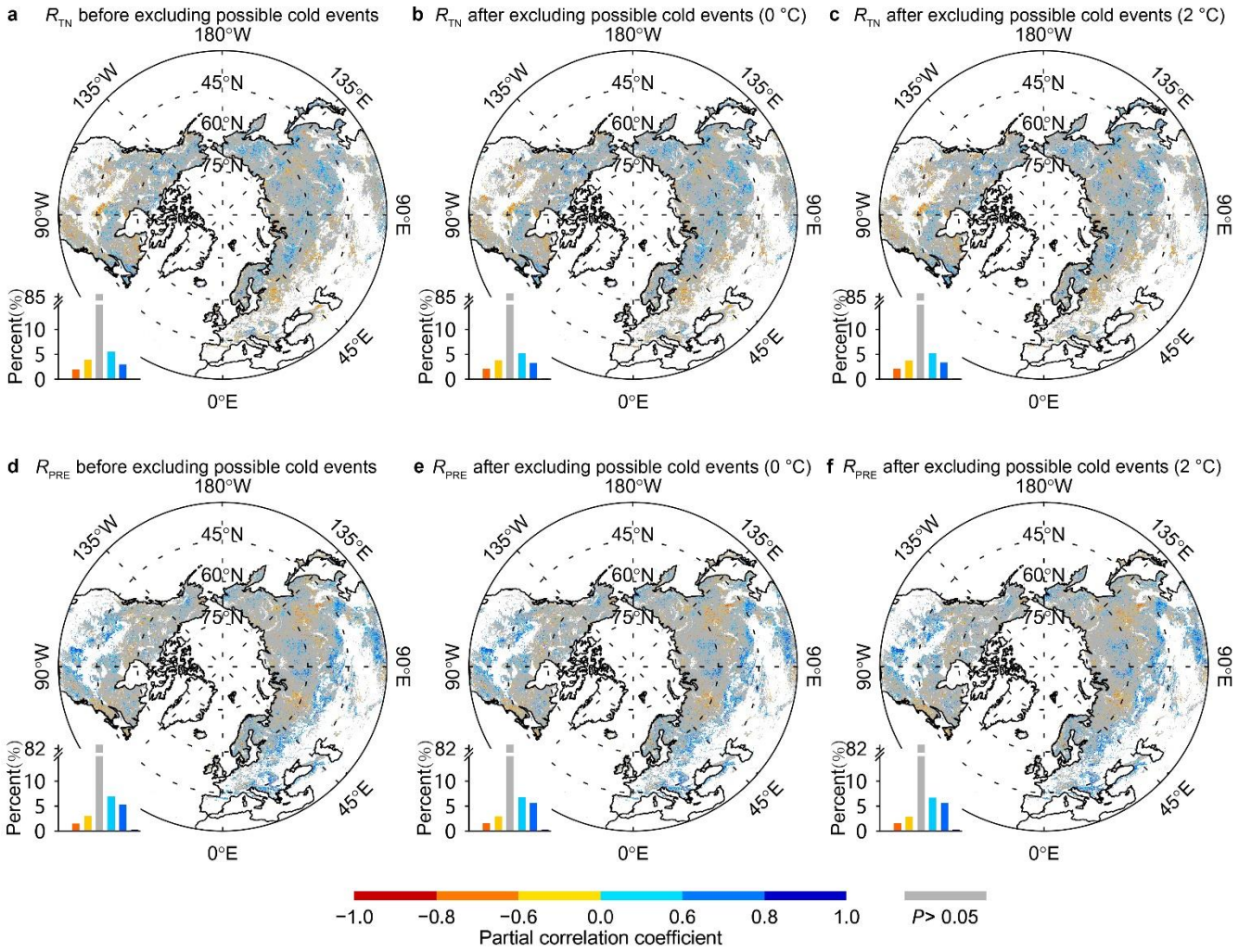

Figure S14. Spatial pattern of the partial correlation coefficient between the timing of onset of leaf coloration (D_{LCO}) and pre-D_{LCO} climatic factors over the period 2000–2016 before and after the exclusion of years with possible cold events before D_{LCO}. a–c, Spatial pattern of the partial correlation coefficient (R_{TN}) between D_{LCO} and pre-D_{LCO} mean daily minimum temperature (T_{min}) before (a) and after (b and c) the exclusion of years with possible cold events. d–f, The same as (a–c), but for the partial correlation between D_{LCO} and pre-D_{LCO} total precipitation (R_{PRE}). The bar chart in each panel shows the percentage of area for each interval of the partial correlation coefficient, with the coefficient value indicated by the color scale at the bottom. Non-significant correlations ($P > 0.05$) are in gray, and the percentage for each interval is provided in Table S6. Possible cold events were determined mainly by using a threshold-based method with a daily minimum temperature of 0 °C (b and e) or 2 °C (c and f).

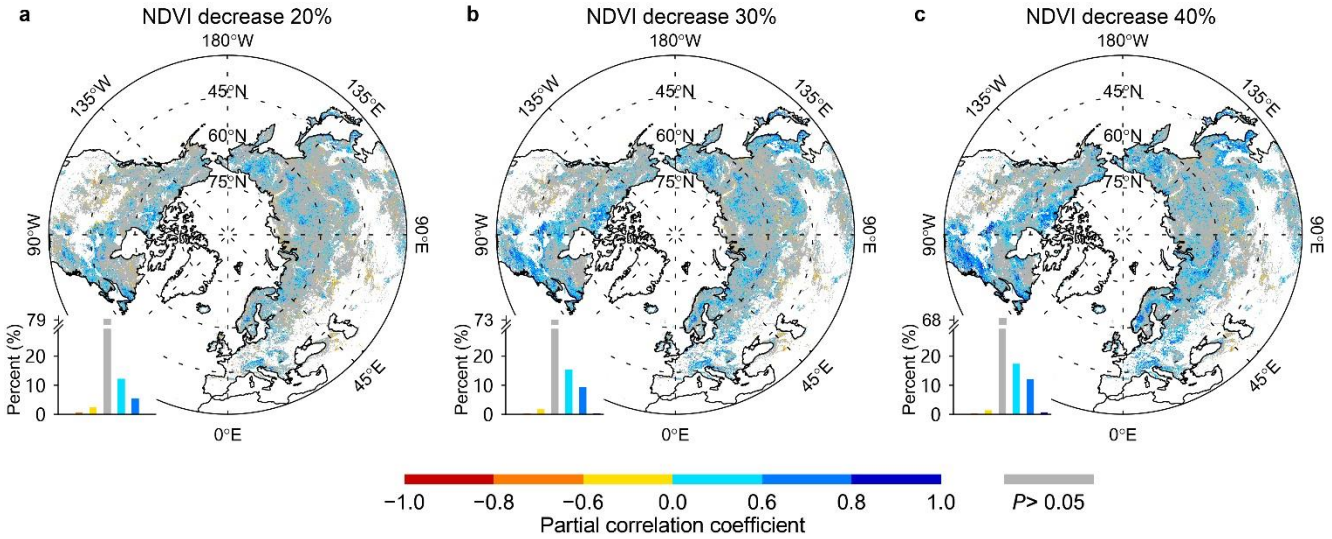

Figure S15. Spatial pattern of the partial correlation coefficient between the timing of different stages of leaf coloration and the mean daily minimum temperature for an optimized period preceding each stage for 2000–2018. The timings of different stages of leaf coloration are determined as the first dates when NDVI decreased by 20% (a), 30% (b), or 40% (c) of its annual amplitude in autumn. The bar chart in each panel shows the percentage of area for each interval of the partial correlation coefficient, with the coefficient value indicated by the color scale at the bottom. Non-significant correlations ($P > 0.05$) are in gray.

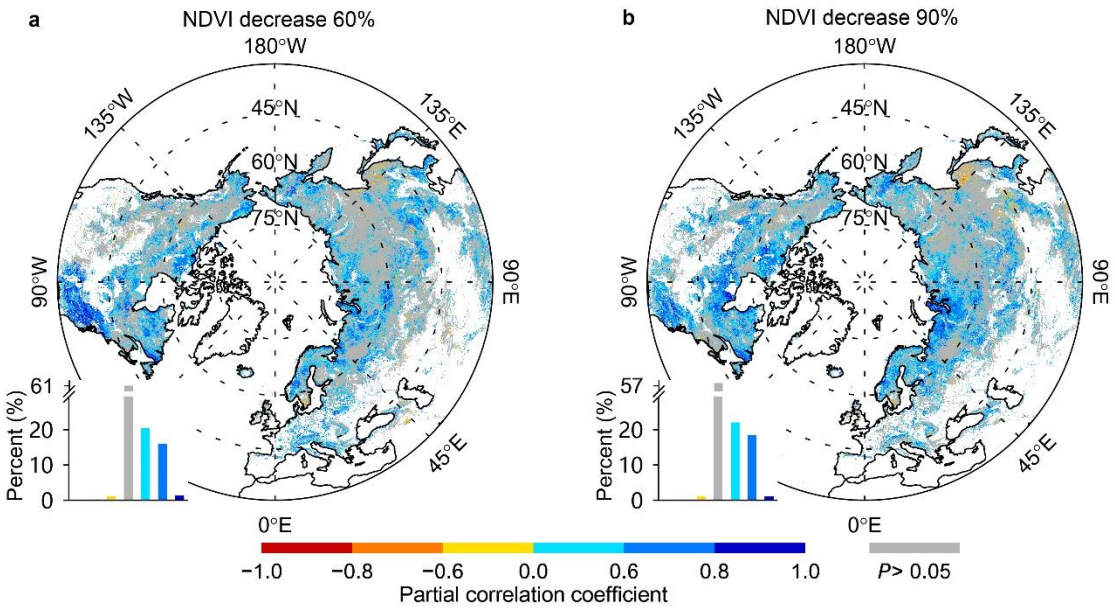

Figure S16. Spatial pattern of the partial correlation coefficient between the timing of the end of leaf coloration (D_{LCE}) and pre-D_{LCE} T_{min} over the period 2000–2018. D_{LCE} was determined as the date when NDVI drops by 60% (**a**) and 90% (**b**), respectively. The bar chart in the bottom-left corner shows the percentage of area for each interval of the partial correlation coefficient, with the coefficient values indicated by the color scale at the bottom. Non-significant correlations ($P > 0.05$) are in gray.

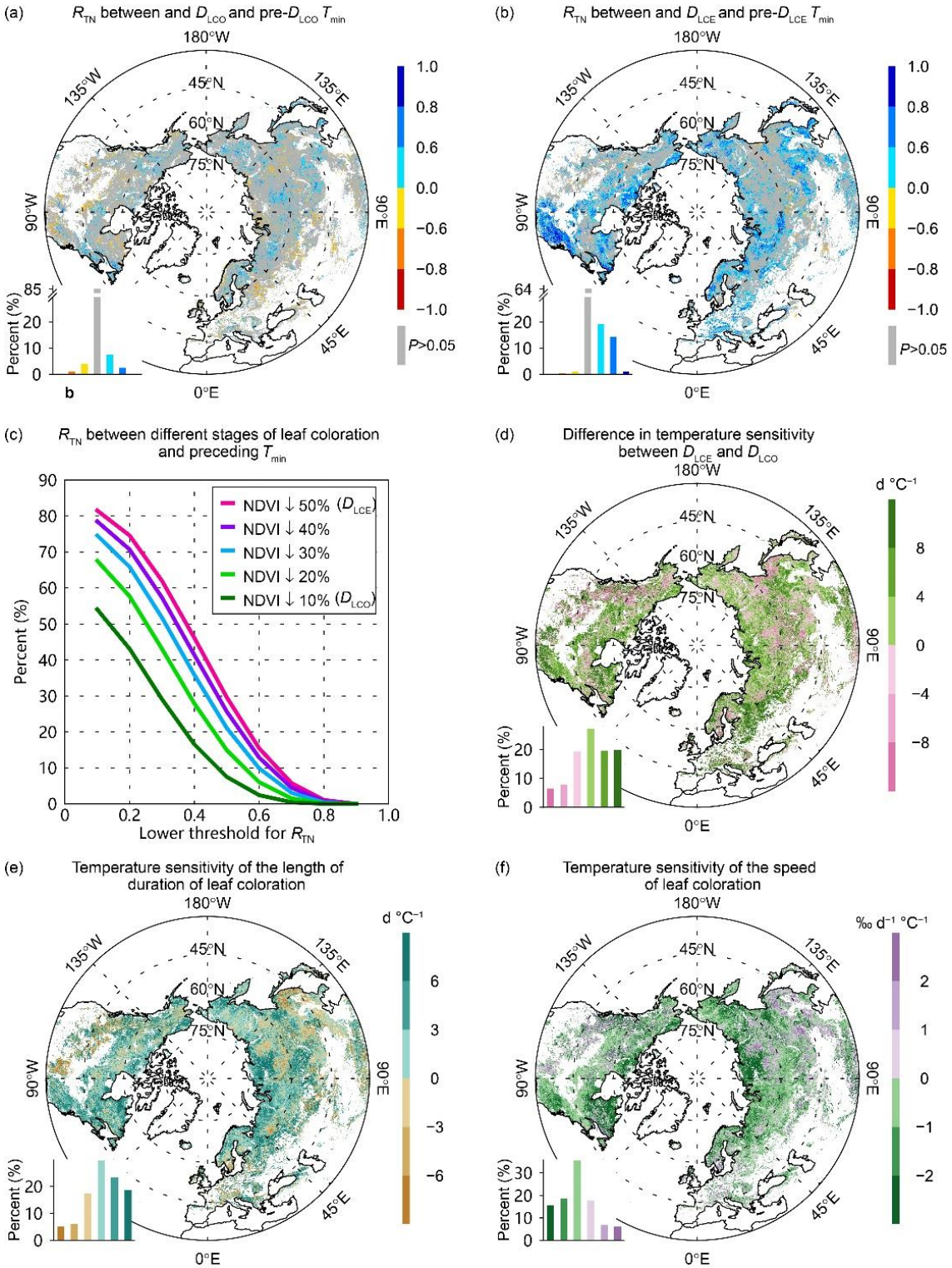

Figure S17. Impacts of temperature on the timing of different stages of leaf coloration and on the progress of leaf coloration over the period 2000–2018. (a) Spatial pattern of the partial correlation coefficient (R_{TN}) between D_{LCO} and pre-D_{LCO} mean daily minimum temperature (T_{min}). (b) Spatial pattern of R_{TN} between timing of the end of leaf coloration (D_{LCE}) and pre-D_{LCE} T_{min}. For pixels

identified as deciduous broadleaved forests, D_{LCO} and D_{LCE} were defined as the dates when NDVI decreased by 10% and 50%, respectively, of their annual amplitude from 1 August (see section 2.4.4 for details).The bar charts in (a) and (b) show the percentage of area for each interval of the partial correlation coefficient ($P < 0.05$), with the coefficient indicated by the color scale on the right. Non-significant correlations ($P > 0.05$) are in gray. (c) Percentage of area for which R_{TN} between the timing of a given stage of leaf coloration and preceding T_{min} is higher than a given threshold indicated by the horizontal axis. For example, R_{TN} for the onset of leaf coloration is higher than 0.2 in about 40% of the area. (d) Difference in temperature sensitivity between D_{LCE} and D_{LCO}. Positive values indicate that D_{LCE} is more sensitive to temperature than D_{LCO}, whereas negative values indicate that D_{LCO} is more sensitive to temperature than D_{LCE}. (e) Temperature sensitivity of the length of duration of leaf coloration. Positive values indicate that warming extends the duration of leaf coloration, whereas negative values indicate that warming shortens the leaf coloration duration. (f) Temperature sensitivity of the speed of leaf coloration. Positive values indicate that warming increases the speed of leaf coloration, whereas negative values indicate that warming reduces the speed of leaf coloration. The bar charts in (d), (e) and (f) show the percentage of area for each interval of the temperature sensitivity indicated by the color scale on the right.

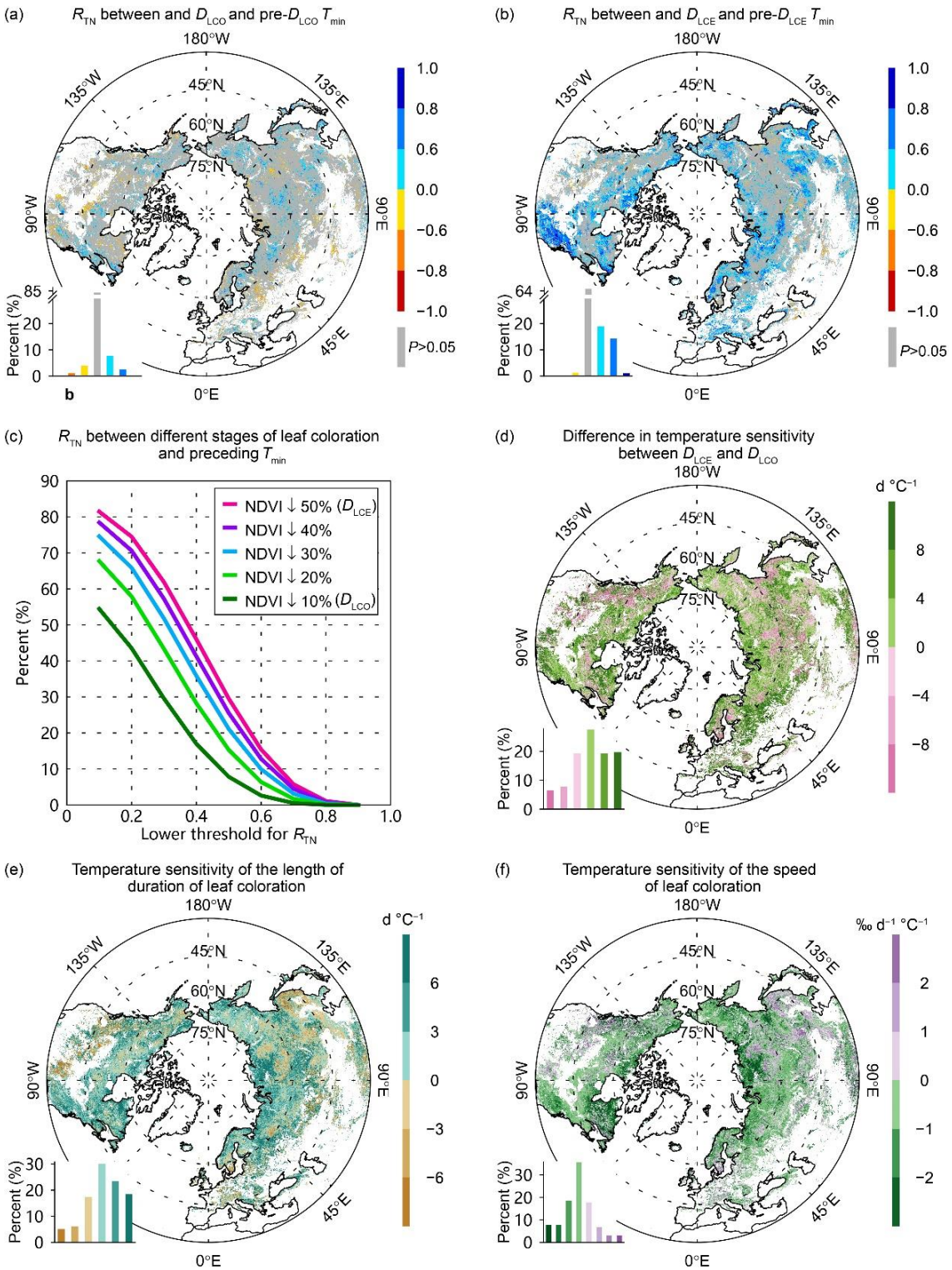

Figure S18. Impacts of temperature on the timing of different stages of leaf coloration and on the progress of leaf coloration over the period 2000–2018. (a) Spatial pattern of the partial correlation coefficient (R_{TN}) between D_{LCO} and pre-D_{LCO} mean daily minimum temperature (T_{min}). (b) Spatial pattern of R_{TN} between timing of the end of leaf coloration (D_{LCE}) and pre-D_{LCE} T_{min}. For pixels

identified as deciduous broadleaved forests, D_{LCO} and D_{LCE} were defined as the dates when NDVI decreased by 10% and 50%, respectively, of their annual amplitude from 16 August (see section 2.4.4 for details). The bar charts in (a) and (b) show the percentage of area for each interval of the partial correlation coefficient ($P < 0.05$), with the coefficient indicated by the color scale on the right. Non-significant correlations ($P > 0.05$) are in gray. (c) Percentage of area for which R_{TN} between the timing of a given stage of leaf coloration and preceding T_{min} is higher than a given threshold indicated by the horizontal axis. For example, R_{TN} for the onset of leaf coloration is higher than 0.2 in about 40% of the area. (d) Difference in temperature sensitivity between D_{LCE} and D_{LCO}. Positive values indicate that D_{LCE} is more sensitive to temperature than D_{LCO}, whereas negative values indicate that D_{LCO} is more sensitive to temperature than D_{LCE}. (e) Temperature sensitivity of the length of duration of leaf coloration. Positive values indicate that warming extends the duration of leaf coloration, whereas negative values indicate that warming shortens the leaf coloration duration. (f) Temperature sensitivity of the speed of leaf coloration. Positive values indicate that warming increases the speed of leaf coloration, whereas negative values indicate that warming reduces the speed of leaf coloration. The bar charts in (d), (e) and (f) show the percentage of area for each interval of the temperature sensitivity indicated by the color scale on the right.

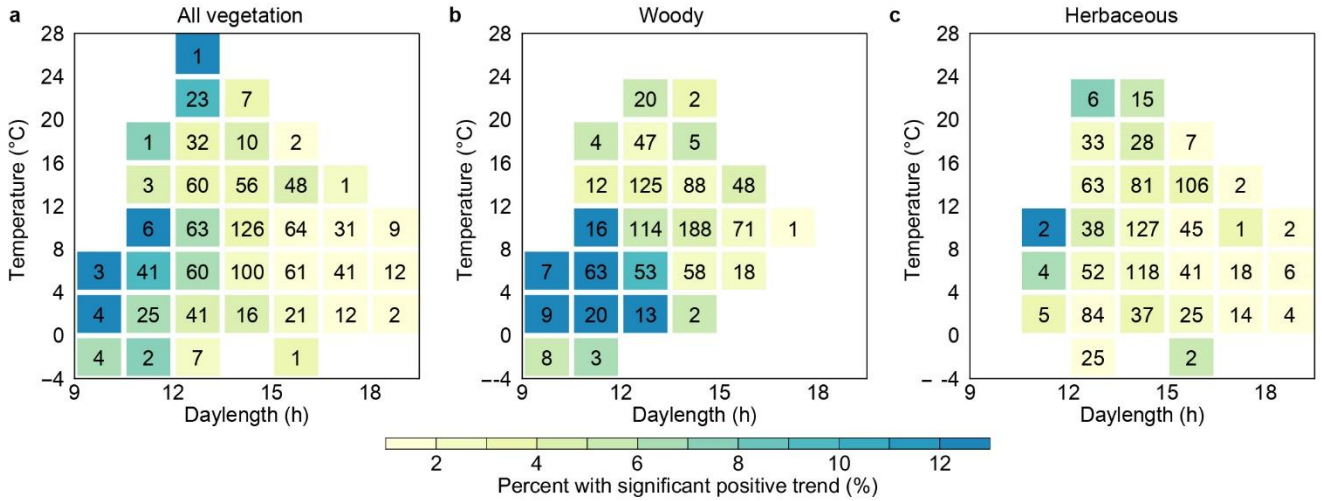

Figure S19. Dependence of temporal trends in the timing of onset of leaf coloration (D_{LCO}) on daylength and temperature at D_{LCO} over the period 2000–2018 for all (a), woody (b), and herbaceous (c) vegetation. a, Color indicates the percentage of area with significant ($P < 0.05$) D_{LCO} delays in each cell (i.e., a specific temperature × daylength combination), as indicated by the color scale at the bottom. The number in each cell indicates the ratio (unit: ‰) of the area in each cell to the total area with D_{LCO} retrieval. Temporal trends and their significances were determined by using the Theil-Sen estimator and Mann-Kendall tests. b and c, The same as (a), but for woody and herbaceous vegetation, respectively. Only cells where the ratio of the area of the cell to the total area is >1‰ are represented.

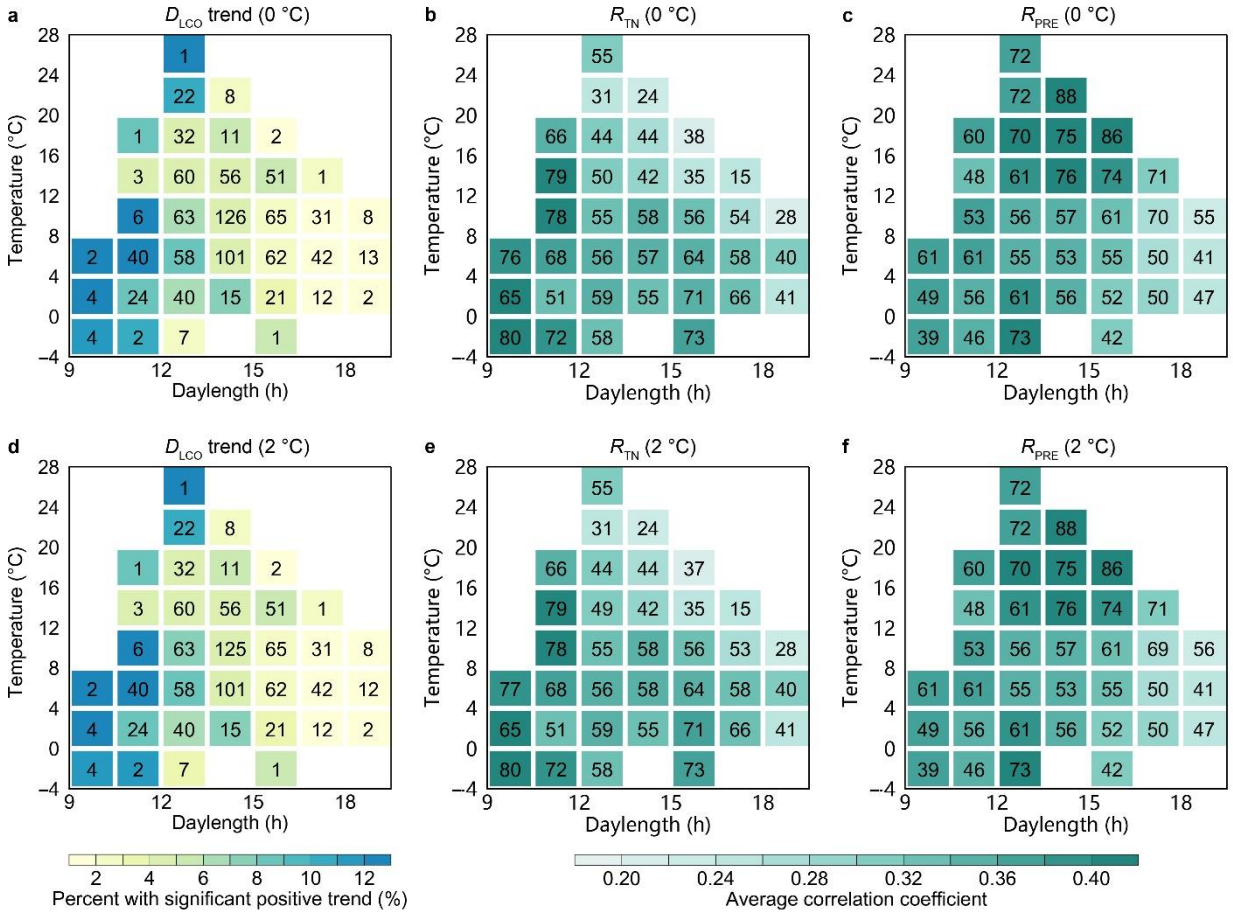

Figure S20. Dependence of temporal trends in the timing of onset of leaf coloration (D_{LCO}, a and d), of the partial correlation coefficient (R_{TN}, b and e) between D_{LCO} and pre-D_{LCO} mean daily minimum temperature, and of the partial correlation coefficient (R_{PRE}, c and f) between D_{LCO} and pre-D_{LCO} total precipitation on daylength and temperature at D_{LCO} over the period 2000–2016 after the exclusion of years with possible cold events before D_{LCO}. Possible cold events were determined mainly by using a threshold-based method with a daily minimum temperature of 0 °C (a–c) or 2 °C (d–f). a and d, Color indicates the percentage of area with significant ($P < 0.05$) D_{LCO} delays in each cell (i.e., a specific temperature × daylength combination), as indicated by the color scale at the bottom. The number in each cell indicates the ratio (unit: ‰) of the area in each cell to the total area with D_{LCO} retrieval. b and e, Color indicates the average of the positive R_{TN}, as indicated by the color scale at the bottom. The number indicates the percentage of area with a positive correlation in each cell. c and f, The same as (b and e), but for the positive R_{PRE}. Only cells where the ratio of the area of the cell to the total area is >1‰ are represented.

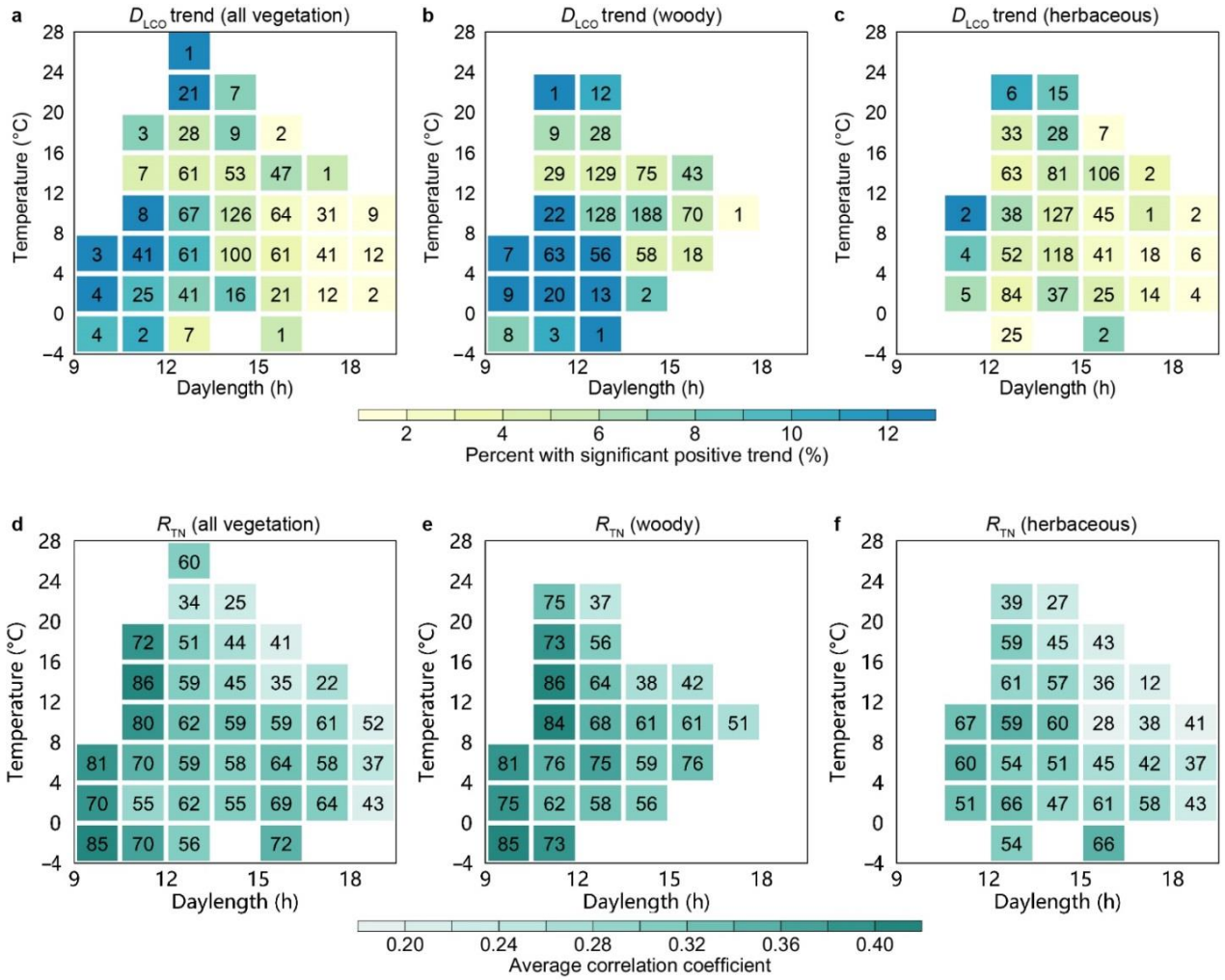

Figure S21. Dependence of temporal trends in the timing of onset of leaf coloration (D_{LCO}, a–c) and of the partial correlation coefficient (R_{TN}, d–f) between D_{LCO} and pre-D_{LCO} mean daily minimum temperature (T_{min}) on daylength and temperature at D_{LCO} over the period 2000–2018. a, Color indicates the percentage of area with significant ($P < 0.05$) D_{LCO} delays in each cell (i.e., a specific temperature × daylength combination), as indicated by the color scale at the bottom. The number in each cell indicates the ratio (unit: ‰) of the area in each cell to the total area with D_{LCO} retrieval. The temporal trends and their significances were determined by ordinary least squares regression and *t*-tests. b and c, The same as (a) but for woody and herbaceous vegetation, respectively. d, Color indicates the average of the positive R_{TN}. The number indicates the percentage of area with a positive correlation in each cell, as indicated by the color scale at the bottom. e and f, The same as (d) but for woody and herbaceous vegetation, respectively. For the pixels identified as deciduous broadleaved forests, D_{LCO} was defined as the date when NDVI decreased by 10% of its annual amplitude from 1 August (see Section 2.4.4 for details). Only cells where the ratio of the area of the cell to the total area is >1‰ are represented.

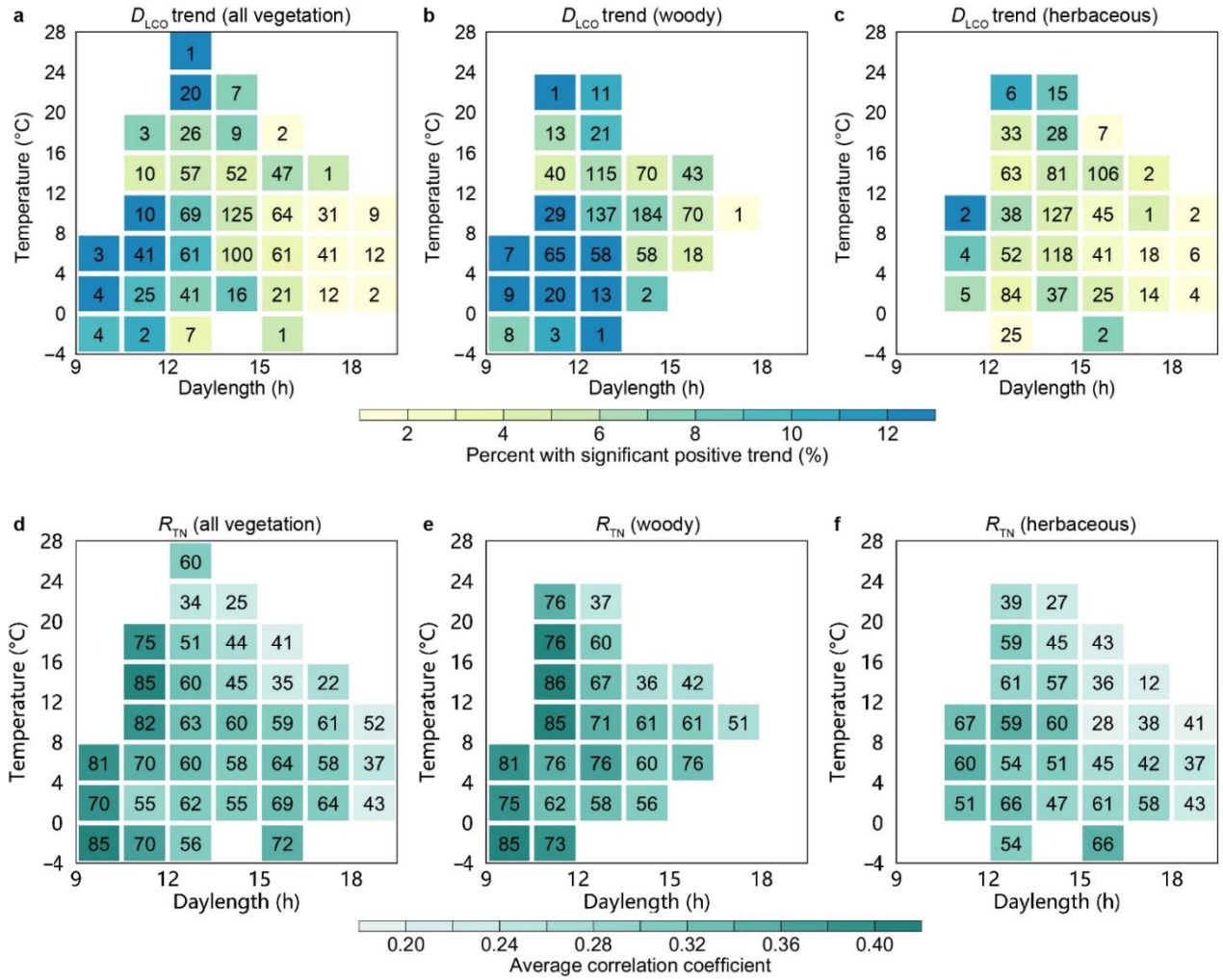

Figure S22. Dependence of temporal trends in the timing of onset of leaf coloration (D_{LCO}, a–c) and of the partial correlation coefficient (R_{TN}, d–f) between D_{LCO} and pre-D_{LCO} mean daily minimum temperature (T_{min}) on daylength and temperature at D_{LCO} over the period 2000–2018. a, Color indicates the percentage of area with significant ($P < 0.05$) D_{LCO} delays in each cell (i.e., a specific temperature × daylength combination), as indicated by the color scale at the bottom. The number in each cell indicates the ratio (unit: ‰) of the area in each cell to the total area with D_{LCO} retrieval. The temporal trends and their significances were determined by ordinary least squares regression and *t*-tests. b and c, The same as (a) but for woody and herbaceous vegetation, respectively. d, Color indicates the average of the positive R_{TN}, as indicated by the color scale at the bottom. The number indicates the percentage of area with a positive correlation in each cell. e and f, The same as (d) but for woody and herbaceous vegetation, respectively. For the pixels identified as deciduous broadleaved forests, D_{LCO} was defined as the date when NDVI decreased by 10% of its annual amplitude from 16 August (see Section 2.4.4 for details). Only cells where the ratio of the area of the cell to the total area is >1‰ are represented.

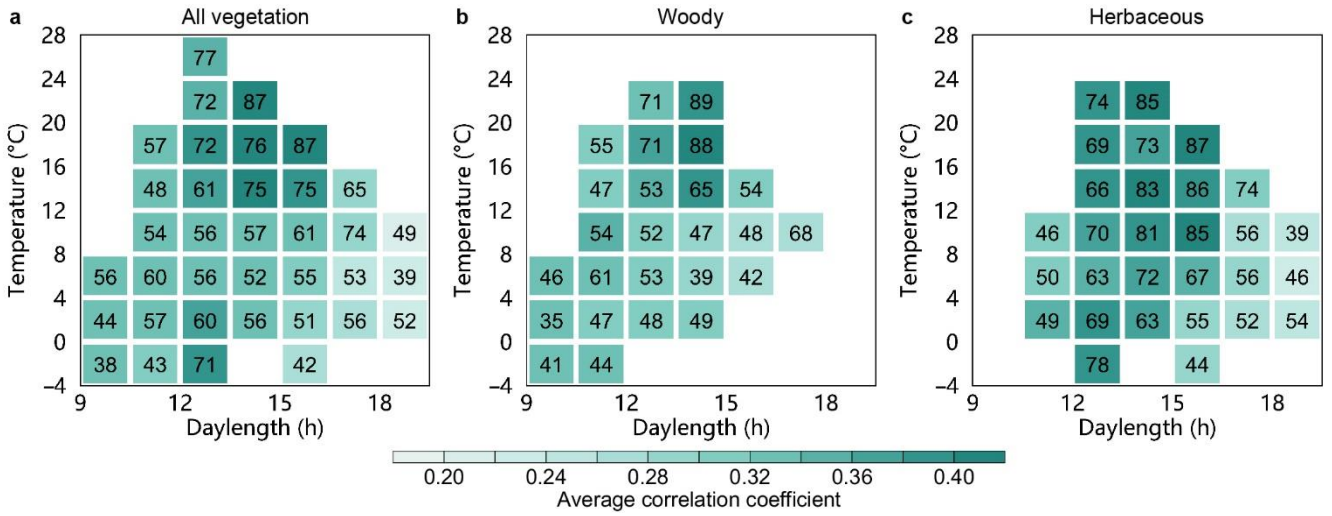

Figure S23. Dependence of the partial correlation coefficient (R_{PRE}) between the timing of onset of leaf coloration (D_{LCO}) and pre-D_{LCO} total precipitation on daylength and temperature at D_{LCO} over the period 2000–2018 for all (a), woody (b), and herbaceous (c) vegetation. a, Color indicates the average of the positive R_{PRE}, as indicated by the color scale at the bottom. The number indicates the percentage of area with a positive correlation in each cell (i.e., a specific temperature × daylength combination); b and c, The same as (a), but for woody and herbaceous vegetation, respectively. Only cells where the ratio of the area of the cell to the total area is >1‰ are represented.

Supplementary Tables

Table S1. Experiments on photoperiodic control of plant growth.

Species	Life-form	Findings from experiments	Experimental setting	Reference
Acer rubrum L.	Deciduous tree	Growth stopped after about four weeks of short photoperiod treatment (8 hours).	Chamber cultivating +controlled photoperiod	Downs and Borthwick (1956)
Acer saccharum Marsh.	Deciduous tree	Long photoperiod treatment (16 hours) resulted in delayed senescence and abscission for up to five months.	Chamber cultivating +controlled photoperiod	Olmsted (1951)
Aesculus hippocastanum L.	Deciduous tree	Growth stopped after about four weeks of short photoperiod treatment (8 hours).	Chamber cultivating +controlled photoperiod	Downs and Borthwick (1956)
Betula mandshurica [Regel] Nakai.	Deciduous tree	Growth stopped after about four weeks of short photoperiod treatment (8 hours).	Chamber cultivating +controlled photoperiod	Downs and Borthwick (1956)
Betula pubescens Ehrh.	Deciduous tree	Elongation growth ceased after 7–8 days of short photoperiod treatment (12 hours).	Chamber cultivating +controlled photoperiod	Rinne, Saarelainen, and Junttila (1994)
Catalpa bignonioides Walt.	Deciduous tree	Growth stopped after about four weeks of short photoperiod treatment (8 hours).	Chamber cultivating +controlled photoperiod	Downs and Borthwick (1956)
Catalpa speciosa Warder	Deciduous tree	Growth stopped after about four weeks of short photoperiod treatment (8 hours).	Chamber cultivating +controlled photoperiod	Downs and Borthwick (1956)
Cornus florida L.	Deciduous tree	Growth stopped after about four weeks of short photoperiod treatment (8 hours).	Chamber cultivating +controlled photoperiod	Downs and Borthwick (1956)
Liquidambar styraciflua L.	Deciduous tree	Growth stopped after about four weeks of short photoperiod treatment (8 hours).	Chamber cultivating +controlled photoperiod	Downs and Borthwick (1956)
Liquidambar styraciflua L.	Deciduous tree	The plant grew nearly all winter under a 16 hours photoperiod.	Chamber cultivating +controlled photoperiod	Kramer (1936)
Liriodendron tulipifera L.	Deciduous tree	Growth stopped after about ten days of short photoperiod treatment (8 hours).	Chamber cultivating +controlled photoperiod	Downs and Borthwick (1956)
Liriodendron tulipifera L.	Deciduous tree	The plant grew all winter under a 16 hours photoperiod.	Chamber cultivating +controlled photoperiod	Kramer (1936)
Paulownia tomentosa [Thunb.] Steud.	Deciduous tree	Growth stopped after about four weeks of short photoperiod treatment (8 hours).	Chamber cultivating +controlled photoperiod	Downs and Borthwick (1956)
Populus trichocarpa Torr, & Gray	Deciduous tree	Plant set bud after 18 days of short photoperiod treatment (13 hours), which is regulated by phytochrome.	Stem cutting + controlled photoperiod	Howe, Gardner GHackett, and Furnier (1996)

Species	Life-form	Findings from experiments	Experimental setting	Reference
Populus tremula	Deciduous tree	Shortening photoperiod was the main trigger for the initiation of autumn senescence.	Chamber cultivating +controlled photoperiod	Fracheboud et al. (2009)
Populus tremula	Deciduous tree	Photoperiod is the sole trigger for the onset of autumn senescence.	Observation under natural conditions	Keskitalo, Bergquist, Gardeström, and Jansson (2005)
Populus tremula x tremuloides	Deciduous tree	When plants are shifted from long days (16 hours) to short days (8 hours), they respond by growth cessation and bud set after 32 days.	Chamber cultivating +controlled photoperiod	Böhlenius et al. (2006)
Ulmus americana L.	Deciduous tree	Growth stopped after about twenty weeks of short photoperiod treatment (8 hours).	Chamber cultivating +controlled photoperiod	Downs and Borthwick (1956)
Picea abies (L.) Karst.	Evergreen tree	Growth cessation occurred within two weeks after exposure to short photoperiods (≤15 hours).	Chamber cultivating +controlled photoperiod	Heide (1974)
Picea glauca (Moench) Voss	Evergreen tree	Growth cessation occurred after five weeks of short photoperiod treatment (8 hours) under warm temperature conditions.	Chamber cultivating +controlled photoperiod	Hamilton et al. (2016)
Pinus sylvestris L.	Evergreen tree	Northern populations grown under 50°N photoperiod (shorter) stopped growth earlier than that under 60°N photoperiod (longer).	Chamber cultivating +controlled photoperiod	Oleksyn, Tjoelker, and Reich (1992)
Pinus sylvestris L.	Evergreen tree	Growth stopped after about four weeks of short photoperiod treatment (8 hours).	Chamber cultivating +controlled photoperiod	Downs and Borthwick (1956)
Pinus taeda L.	Evergreen tree	Growth stopped after about four weeks of short photoperiod treatment (8 hours).	Chamber cultivating +controlled photoperiod	Downs and Borthwick (1956)
Pinus taeda L.	Evergreen tree	The plant grew all winter with a 14.5 hours photoperiod.	Chamber cultivating +controlled photoperiod	Kramer (1936)
Pinus virginiana Mill.	Evergreen tree	Growth stopped after about four weeks of short photoperiod treatment (8 hours).	Chamber cultivating +controlled photoperiod	Downs and Borthwick (1956)
Salix pentandra L.	Deciduous small tree or shrub	Short photoperiod (≤ 22 hours for a northern ecotype and ≤ 15 hours for a southern ecotype) induced apical growth cessation.	Chamber cultivating +controlled photoperiod	Junttila (1980)
Salix polaris L.	Deciduous small tree or shrub	Leaf abscission in the arctic ecotype was stimulated by short photoperiod when grown at 15°C.	Collected with roots + controlled photoperiod	Paus, Nilsen, and Junttila (1986)

Species	Life-form	Findings from experiments	Experimental setting	Reference
Syringa vulgaris L.	Deciduous small tree or shrub	Photosynthetic efficiency has a more consistent relationship with photoperiod than with temperature.	Observation under natural conditions	Aikio, Taulavuori, Hurskainen, Taulavuori, and Tuomi (2019)
Hibiscus rosa-sinensis L.	Evergreen small tree or shrub	Leaves under long photoperiod treatment (16 hours) spend ten more days to complete senescence than that under short photoperiod treatment (8 hours).	Leaves cutting + controlled photoperiod	Misra and Biswal (1973)
Hibiscus syriacus L.	Deciduous shrub	Short photoperiod (8 hours) induced dormancy while long photoperiod (16 hours) delayed dormancy and resulted in considerable winter injury	Chamber cultivating +controlled photoperiod	Davidson (1957)
Weigela florida A. DC.	Deciduous shrub	Short photoperiod (8 hours) induced dormancy while long photoperiod (16 hours) delayed dormancy and resulted in considerable winter injury.	Chamber cultivating +controlled photoperiod	Davidson (1957)
Rhododendron catawbiense Michx.	Evergreen shrub	Short photoperiod (8 hours) induced dormancy while long photoperiod (16 hours) delayed dormancy and resulted in considerable winter injury.	Chamber cultivating +controlled photoperiod	Davidson (1957)
Cucurbita pepo Linn.	Herbaceous	After three months of growth, much larger percentage of mesophyll cell death was detected in short photoperiod (9 hours) than that in long photoperiod (18 hours).	Chamber cultivating +controlled photoperiod	Wang, Hu, Li, Cui, and Zhu (2002)
Sedum telephium L. subsp. *maximum* (L.) Krocker	Herbaceous	After eight weeks of growth, plants in long photoperiod (24 hours) elongated rapidly while those in short photoperiod (10 hours) became dormant.	Chamber cultivating +controlled photoperiod	Heide (2001)
Vitis labruscana Bailey	Herbaceous	Cane elongation was less in response to short photoperiod treatments (12 or 13 hours), as compared to natural photoperiod (13.7 or 14.3 hours).	Stem cutting + controlled photoperiod	Fennell and Hoover (1991)
Vitis riparia Michx.	Herbaceous	Cane elongation was less in response to short photoperiod treatments (12 or 13 hours), as compared to natural photoperiod (13.7 or 14.3 hours).	Stem cutting + controlled photoperiod	Fennell and Hoover (1991)

Table S2. *In situ* observations in China used in this study.

Site Name	Latitude	Longitude	Species number	Start year	End year	Year length
Nunkiang	49	125	5	1975±0	1993±4	17±4
Wudalianchi	48	126	11	1976±3	1995±3	18±3
Kiamusze	47	130	6	1981±1	1996±0	16±1
Minqin	38	103	29	1981±1	1996±1	12±1
Hohhot	41	112	10	1981±2	1996±1	13±2
Mutankiang	44	130	41	1980±2	1996±2	13±2
Beijing	40	116	42	1972±1	1994±3	20±4
Chengteh	41	118	5	1983±2	1996±0	12±1
Qinhuangdao	39	119	15	1980±0	1993±0	13±1
Gaizhou	40	122	12	1979±1	1996±0	17±1
Yixian	39	115	17	1980±0	1993±0	12±1
Liaocheng	36	115	5	1974±4	1993±2	15±3
Tyan	36	117	5	1974±0	1986±0	11±0
Sian	34	109	33	1977±3	1994±3	15±3
Luoyang	35	113	27	1977±4	1996±1	18±4
Yancheng	33	120	19	1981±4	1996±0	15±3
Zhengjiang	32	119	15	1976±3	1993±2	17±3
Hefei	32	117	19	1979±1	1995±1	17±2
Wuhu	31	118	16	1982±1	1996±0	13±1

The mean ± standard deviation of start year, end year and length of time series are provided for each site.

Table S3. FLUXNET2015 flux tower sites used in this study.

Fluxnet ID	Vegetation type	Latitude	Longitude	Year range	Reference
BE-Bra	Mixed Forests	51.31	4.52	1999-2002, 2004-2014	Janssens (2016)
BE-Vie	Mixed Forests	50.31	6.00	1996-2014	De Ligne, Manise, Heinesch, Aubinet, and Vincke (2016)
CA-Gro	Mixed Forests	48.22	−82.16	2003-2013	McCaughey (2016)
CA-Man	Evergreen Needleleaf Forest	55.88	−98.48	1994-2004, 2006-2008	Amiro (2016)
CA-Oas	Mixed Forests	53.63	−106.20	1996-2010	Black (2016a)
CA-Obs	Evergreen Needleleaf Forest	53.99	−105.12	1999-2010	Black (2016b)
CA-TP3	Mixed Forests	42.71	−80.35	2003-2014	Arain (2016a)
CA-TP4	Mixed Forests	42.71	−80.36	2002-2014	Arain (2016b)
CH-Dav	Evergreen Needleleaf Forest	46.82	9.86	1997-2014	Hörtnagl, Eugster, Merbold, et al. (2016)
CH-Lae	Mixed Forests	47.48	8.37	2004-2014	Hörtnagl, Eugster, Buchmann, et al. (2016)
CZ-BK1	Evergreen Needleleaf Forest	49.50	18.54	2004-2014	Šigut, Havrankova, Jocher, Pavelka, and Janouš (2016)
DE-Gri	Mixed Forests	50.95	13.51	2004-2014	Bernhofer et al. (2016a)
DE-Hai	Mixed Forests	51.08	10.45	2000-2012	Knohl et al. (2016)
DE-Tha	Evergreen Needleleaf Forest	50.96	13.57	1996-2014	Bernhofer et al. (2016b)
DK-Sor	Deciduous Broadleaf Forest	55.49	11.64	1996-2014	Ibrom and Pilegaard (2016)
DK-ZaH	Open Shrublands	74.47	−20.55	2000-2010, 2012-2014	Lund, Jackowicz-Korczynski, and Abermann (2016)
FI-Hyy	Evergreen Needleleaf Forest	61.85	24.30	1996-2014	Mammarella et al. (2016)
FI-Sod	Evergreen Needleleaf Forest	67.36	26.64	2001-2014	Aurela et al. (2016)
FR-Fon	Deciduous Broadleaf Forest	48.48	2.78	2005-2014	Berveiller et al. (2016)

Fluxnet ID	Vegetation type	Latitude	Longitude	Year range	Reference
IT-Col	Deciduous Broadleaf Forest	41.85	13.59	1997-2002, 2004-2014	Matteucci (2016)
IT-Lav	Evergreen Needleleaf Forest	45.96	11.28	2003-2014	Gianelle, Zampedri, Cavagna, and Sottocornola (2016)
IT-MBo	Grasslands	46.01	11.05	2003-2013	Gianelle, Cavagna, Zampedri, and Marcolla (2016)
IT-Ren	Evergreen Needleleaf Forest	46.59	11.43	1999, 2002-2003, 2005-2013	Minerbi and Montagnani (2016)
NL-Loo	Evergreen Needleleaf Forest	52.17	5.74	1996-2014	Moors and Elbers (2016)
RU-Cok	Open Shrublands	70.83	147.49	2003-2013	Dolman et al. (2016)
RU-Fyo	Mixed Forests	56.46	32.92	1998-2014	Varlagin, Kurbatova, and Vygodskaya (2016)
US-GLE	Evergreen Needleleaf Forest	41.36	−106.24	2005-2014	Massman (2016)
US-Ha1	Mixed Forests	42.54	−72.17	1992-2012	Munger (2016)
US-MMS	Deciduous Broadleaf Forest	39.32	−86.41	1999-2014	Novick and Phillips (2016)
US-Me2	Evergreen Needleleaf Forest	44.45	−121.56	2002-2014	Law (2016)
US-NR1	Evergreen Needleleaf Forest	40.03	−105.55	1999-2014	Blanken (2016)
US-Oho	Deciduous Broadleaf Forest	41.55	−83.84	2004-2013	Chen (2016)
US-PFa	Mixed Forests	45.95	−90.27	1996-2014	Desai (2016)
US-SRM	Open Shrublands	31.82	−110.87	2004-2014	Scott (2016a)
US-UMB	Deciduous Broadleaf Forest	45.56	−84.71	2000-2014	Gough, Bohrer, and Curtis (2016)
US-Wkg	Grasslands	31.74	−109.94	2004-2014	Scott (2016b)

275

Table S4. Percentage of time series for each interval of the temporal trend in D_{LCO} before and after the exclusion of years with cold events.

Metrics	Number of time-series	Cold events	Interval of significant temporal trend (d y^{-1}) ($P < 0.05$)				$P > 0.05$
			<−1	[−1, 0)	(0, 1]	>1	
Satellite D_{LCO} (2000–2016)	2.01×10^6	Not excluded	2	2	2	4	90
		Excluded (0 °C)	2	2	2	4	90
		Excluded (2 °C)	2	2	2	54	90
in situ D_{LCO} China	326	Not excluded	12	4	4	6	74
		Excluded (0 °C)	12	4	5	6	73
		Excluded (2 °C)	12	3	5	7	73

D_{LCO}, timing of onset of leaf coloration in autumn. Temporal trends were determined by using the ordinary least squares regression between D_{LCO} and the respective years, with *t*-tests. Only time series with at least 10 continuous years of data after exclusion of years with cold events were included. Cold events were determined mainly by using a threshold-based method with a daily minimum temperature of 0 °C or 2 °C. Data in the farthest right column indicate the percentage of area or time-series with a non-significant trend.

Table S5. Percentage of time series for each interval of the temporal trend in D_{LCO}.

Metrics	Number of time-series	Interval of significant temporal trend (d y^{-1}) ($P < 0.05$)				$P > 0.05$
		<−1	[−1, 0)	(0, 1]	>1	
Satellite D_{LCO} (2000–2018)	2.07×10^6	1	2	1	3	93
in situ D_{LCO} China	332	8	2	3	3	84

D_{LCO}, timing of the onset of leaf coloration in autumn. Temporal trends were determined by using the Theil-Sen estimator between D_{LCO} and the respective years, with Mann-Kendall tests. Data in the farthest right column indicate the percentage of area or time-series with a non-significant trend.

Table S6. Percentage of correlations between D_{LCO} or D_{PDO} and each climate factor for each interval of the partial correlation coefficient before and after the exclusion of years with cold events.

Metrics	Climatic Factor	Cold Events	Interval of the partial correlation coefficient ($P < 0.05$)						$P > 0.05$
			[−1.0, −0.8)	[−0.8, −0.6)	[−0.6, 0)	(0, 0.6]	(0.6, 0.8]	(0.8, 1.0]	
Satellite D_{LCO} (2000–2016)	Temperature	Not excluded	0	2	4	5	3	0	86
		Excluded (0 °C)	0	2	4	5	3	0	86
		Excluded (2 °C)	0	2	4	5	3	0	86
	Precipitation	Not excluded	0	2	3	7	5	0	83
		Excluded (0 °C)	0	2	3	7	5	0	83
		Excluded (2 °C)	0	2	3	7	5	0	83
in situ D_{LCO} China	Temperature	Not excluded	0	2	3	4	8	1	82
		Excluded (0 °C)	0	2	2	4	9	1	82
		Excluded (2 °C)	0	3	1	4	9	1	82
	Precipitation	Not excluded	0	3	3	4	5	0	85
		Excluded (0 °C)	0	3	3	3	6	0	85
		Excluded (2 °C)	0	3	3	3	6	0	85
FLUXNET2015 D_{PDO}	Temperature	Not excluded	0	5	3	0	3	0	89
		Excluded (0 °C)	0	5	3	0	0	0	92
		Excluded (2 °C)	0	5	3	0	0	0	92
	Precipitation	Not excluded	0	6	0	8	3	5	78
		Excluded (0 °C)	0	6	0	8	3	5	78
		Excluded (2 °C)	0	6	0	8	3	5	78

D_{PDO}, timing of onset of decrease in maximum canopy photosynthetic capacity in autumn; D_{LCO}, timing of onset of leaf coloration in autumn. Cold events were determined mainly by using a threshold-based method with a daily minimum temperature of 0 °C or 2 °C. Data in the farthest right column indicate the percentage of area or time-series with a non-significant correlation.

Table S7. Percentage of correlations between D_{LCO} or D_{PDO} and each climate factor for each interval of the partial correlation coefficient.

Climatic factor	Metrics	Interval of the partial correlation coefficient ($P < 0.05$)						$P > 0.05$
		[−1.0, −0.8)	[−0.8, −0.6)	[−0.6, 0)	(0, 0.6]	(0.6, 0.8]	(0.8, 1.0]	
Temperature	FLUXNET2015 D_{PDO}	0	7	0	0	3	0	90
	Satellite D_{LCO}	0	4	3	3	3	0	87
Precipitation	FLUXNET2015 D_{PDO}	0	7	0	0	3	7	83
	Satellite D_{LCO}	0	0	0	0	7	0	93

D_{PDO}, timing of onset of decrease in maximum canopy photosynthetic capacity in autumn; D_{LCO}, timing of onset of leaf coloration in autumn. The relationships between D_{LCO} (or D_{PDO}) and temperature were determined by using a partial correlation analysis between D_{LCO} (or D_{PDO}) and pre-D_{LCO} (or pre-D_{PDO}) mean daily minimum temperature, with concurrent total precipitation as the control variable. The relationships between D_{LCO} (or D_{PDO}) and pre-D_{LCO} (or pre-D_{PDO}) precipitation were determined similarly. Only sites with at least 10 continuous years of valid data for both D_{LCO} and D_{PDO} were included. Data in the farthest right column indicate the percentage of area or time-series with a non-significant correlation. To make the satellite D_{LCO} and FLUXNET2015 D_{PDO} more comparable, MOD09A1 with a spatial resolution of 500 m was used for extracting satellite D_{LCO}.

Supplementary Methods

1 Preparation of high quality 5-day NDVI time series

The quality of the daily surface reflectance data from MOD09CMG was unsatisfactory owing to cloud contamination (Vermote, 2015), so we used the 5-day maximum value composite approach (Zhang, 2015), combined with a Savitzky-Golay filter (Cao et al., 2018), to produce a high-quality NDVI time series before determining D_{LCO}. Details of the data preprocessing are given in the following text.

1) Calculating daily NDVI. We calculated the daily NDVI time series with the quality flag from surface reflectance in the red and near-infrared bands as $NDVI = (NIR - RED)/(NIR + RED)$. The quality flags for daily NDVI were derived from the two quality bands (i.e., Internal CM and State QA) of the reflectance product MOD09CMG (Vermote, Roger, & Ray, 2015). We determined four types of conditions that corresponded to the assigned quality flags: 1) clear, 2) uncertain, 3) snowy, and 4) cloudy (with deteriorating data quality), according to Cao et al. (2018) These were subsequently used in the Savitzky-Golay filtering (Cao et al., 2018). To be precise, the quality flag was set to "cloudy" if the cloud state in either Internal CM or State QA was labeled as "yes" or "cloudy or mixed"; the quality flag was set to "snowy" if the snow/ice flag in State QA was labeled as "yes"; and the quality flag was set to "uncertain" if the cloud state in State QA was not set (assumed clear). All the other data flags were set to "clear" (see the index table below). In addition, considering that the NDVI value of a vegetation pixel ranged from −0.2 to 1.0, NDVI data outside this range were treated as gaps in the NDVI time series.

Quality flag of daily NDVI	MOD35 snow/ice flag in State QA	Cloud state in State QA	Cloud state in Internal CM
clear	no	clear	no
uncertain	no	not set (assumed clear)	no
snowy	yes	clear or not set (assumed clear)	no
cloudy	-	cloudy or mixed	-
	-	-	yes

"No" and "yes" in the snow/ice flag indicate absence and presence of snow or ice, respectively; "no" and "yes" in the internal CM indicate absence and presence of cloud, respectively; "-" means no specific snow/ice or cloud state was required.

2) Determining the background NDVI value for each pixel. The background value represents the annual minimum NDVI during winter (December–February), in which NDVI was expected to be stable for winter deciduous vegetation if there was no snow/ice or cloud contamination. The background NDVI value was calculated as the mean of high winter NDVI values, because snow/ice or cloud contamination

decreases NDVI owing to the uncertainties in the snow/ice and cloud flags (Beck, Atzberger, Høgda, Johansen, & Skidmore, 2006). To obtain high winter NDVI values for a given pixel, we first calculated a time series of winter NDVI higher than 0.10 (snow-contaminated NDVI is usually lower than 0.10). The high winter NDVI values were expected to be higher than the 50th percentile of this time series of winter NDVI and lower than the mean + 2SD of this time series of winter NDVI. In some cases, there would be no winter NDVI values higher than 0.10; for these cases the background NDVI value was set at 0.10.

3) Compositing the 5-day NDVI time series from daily NDVI time series. The daily NDVI time-series were aggregated to a 5-day composite as follows: if there were one or more NDVI values meeting the quality level (i.e., the quality flag is "clear" in step 1) within the 5-day period, the median value was used as the composite value to reduce noise, and the composite value was flagged as "clear". If no acceptable NDVI data were found in the 5-day period, the maximum value was used as the composite value (see Figure SM1), and the composite value was flagged as the corresponding daily quality flag of the maximum value.

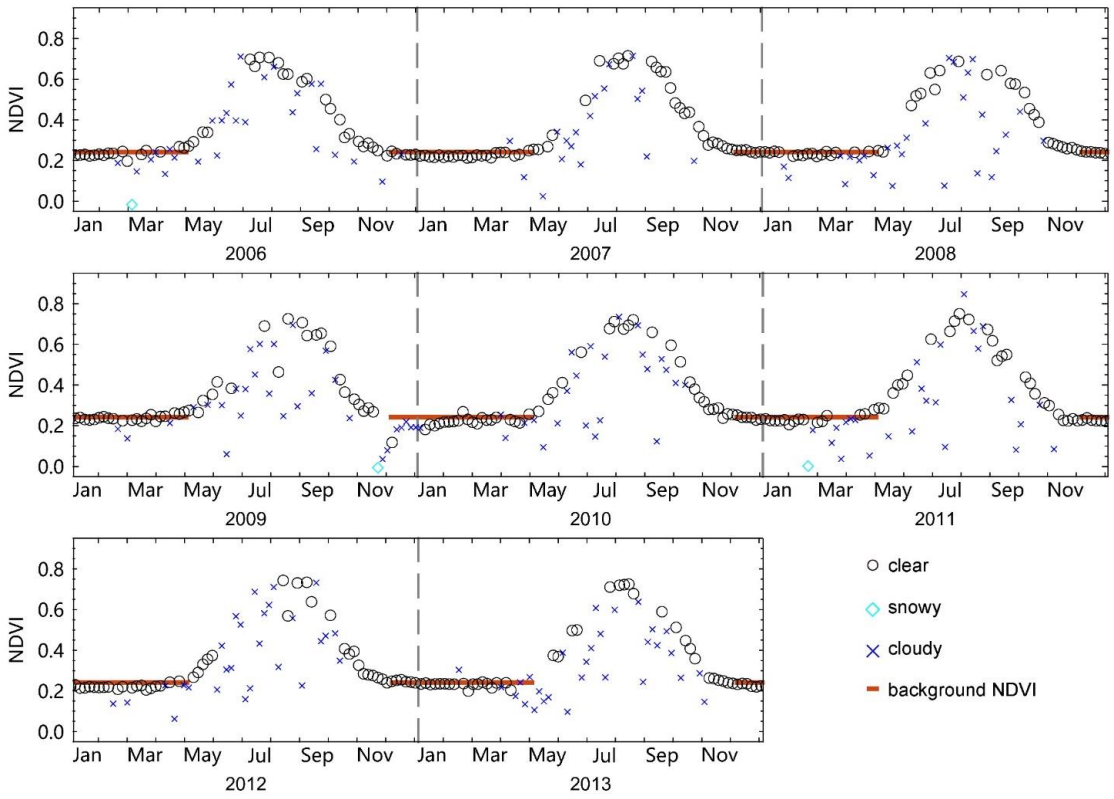

Figure SM1. An example (31.325°N, 98.125°E) showing composite 5-day NDVI time series from

daily NDVI time series.

4) Eliminating snow cover contamination in NDVI data. NDVI values in winter (December–February) were all replaced by the background NDVI value, and their flag was set to "clear", meaning that those NDVI values were not changed in the Savitzky-Golay filtering. In the other three seasons (March–November), the NDVI values lower than this background NDVI value were then substituted for the latter one (see Figure SM2) and their flag values were set to "cloudy".

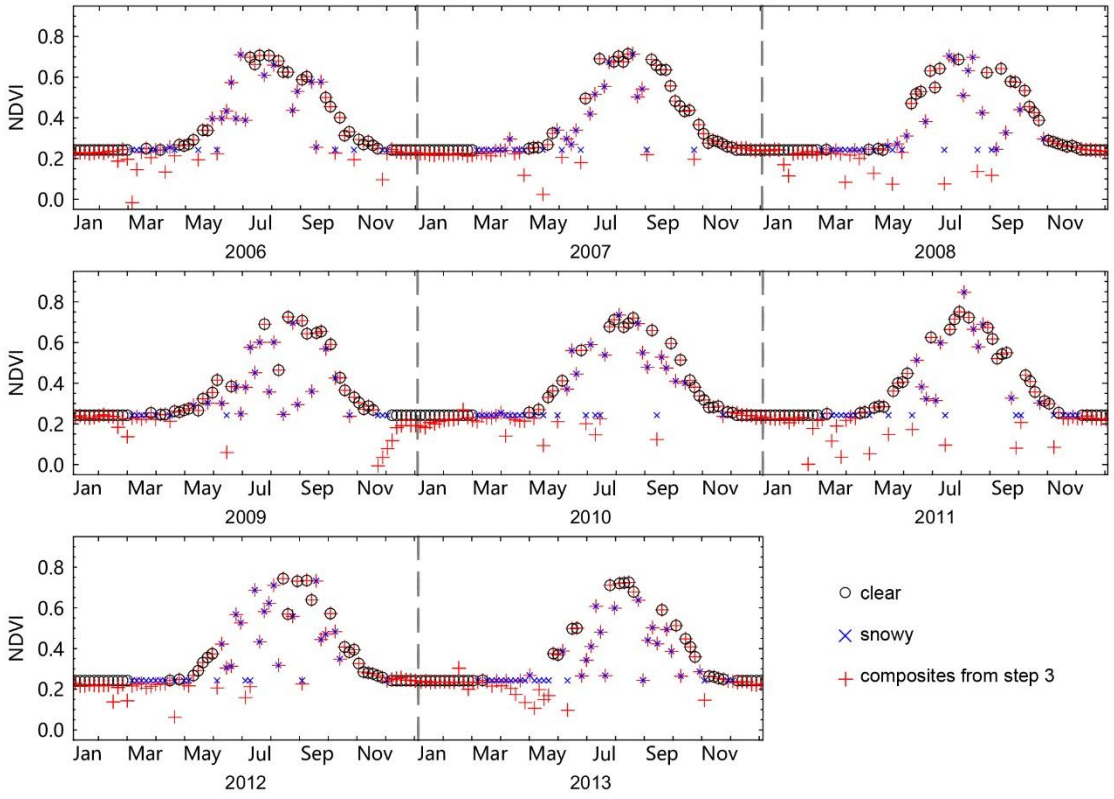

Figure SM2. An example showing the elimination of snow cover contamination in NDVI data.

5) Identifying irregularly high and low NDVI values. Disturbances in surface reflectance data, which are caused by cloud contamination, bidirectional effects, and data transmission errors, result in irregularly high and low NDVI values. Most of these irregular NDVI values could be marked by using the quality flag in step 1. However, because of the uncertainty of the quality flag, there was still a sharp increase or sudden large decrease of NDVI values flagged as "clear" in the 5-day NDVI profile from March to November. Because vegetation growth is a continuous process without large increases or decreases in greenness over a few days, NDVI values that showed sharp decreases or increases were

364 defined as irregularly low or high NDVI values, respectively, and they were identified by using the
365 shape of the NDVI curve and an outlier detection method.

366 The irregularly low NDVI values were identified by using the shape of the NDVI curve.
367 Assuming that the 5-day NDVI increased or decreased gradually in a seasonal course, for any 5-day
368 NDVI at time *t*, denoted as *NDVI*(*t*), an *NDVI*(*t*) was identified as an irregularly low value, if there
369 existed two positive integers *k* and *m* satisfying

370 $$NDVI(t) - NDVI(t-k) \leq -k \times (0.15 \times \text{maxNDVI})$$

371 $$NDVI(t) - NDVI(t+m) \leq -m \times (0.15 \times \text{maxNDVI})$$

372 where $1 \leq k \leq 6$, $1 \leq m \leq 6$, and maxNDVI was the 75th percentile of the time series of annual maximum
373 NDVI from 2000 to 2018. In a few cases, there may have been two consecutive irregularly low values,
374 which were identified as follows. Two consecutive NDVI values, *NDVI*(*t*) and *NDVI*(*t* +1), were
375 identified as consecutive irregularly low values if they satisfied the following inequalities:

376 $$NDVI(t) - NDVI(t-1) \leq -1 \times (0.15 \times \text{maxNDVI})$$

377 $$NDVI(t+1) - NDVI(t-1) \leq -0.9 \times (0.15 \times \text{maxNDVI})$$

378 $$NDVI(t+1) - NDVI(t+2) \leq -2 \times (0.15 \times \text{maxNDVI}).$$

379 The irregularly high NDVI values were identified by using the shape of the NDVI curve and an
380 outlier detection method. The NDVI curve shape-based method included two procedures. Procedure 1
381 was to detect non-consecutive irregularly high NDVI values. Assuming that the 5-day NDVI increased
382 or decreased gradually in a seasonal course, an NDVI value at time *t*, *NDVI*(*t*), was identified as an
383 irregularly high value if it satisfied

384 $$NDVI(t) \geq 1.15 \times \max\{NDVI(t-6), NDVI(t-5), \dots, NDVI(k), \dots, NDVI(t+6)\}$$

385 where $t-6 \leq k \leq t+6$ and $k \neq t$.

386 In some cases, there could be two or more irregularly high NDVI values within 1 month around
387 peak season that could not be detected by using the above algorithm. Such irregularly high NDVI values
388 were identified in Procedure 2, which used the information of a non-consecutive irregularly high NDVI
389 value identified in Procedure 1. We first constructed an array by selecting non-consecutive irregularly
390 high NDVI values in Procedure 1, which were the annual maximum values (denoted as $NDVI_{IHM}$).
391 Then, the NDVI values were identified as irregularly high NDVI values if they were 15% higher than

the median value of the array of $NDVI_{IHM}$.

Because the NDVI values around the peak season were essential for retrieving D_{LCO}, to be more robust, the irregularly high NDVI values were also identified by using Grubb's test (Grubbs, 1950). We first composed an array by using the three highest NDVI values of each year. The outliers in this array were then detected by using Grubb's test at a significance level of $\alpha = 0.05$. Owing to inter-annual variations in the annual maximum greenness, the outliers detected by Grubb's test may not necessarily have been the irregularly high NDVI values. Therefore, in a given year, only outliers that were 15% higher than the mean of the three highest non-outlier NDVI values for that year were identified as irregularly high NDVI values. Finally, all the irregularly high NDVI values identified above were used as irregularly high NDVI values.

The figure SM3 gives examples of irregularly low and high NDVI values.

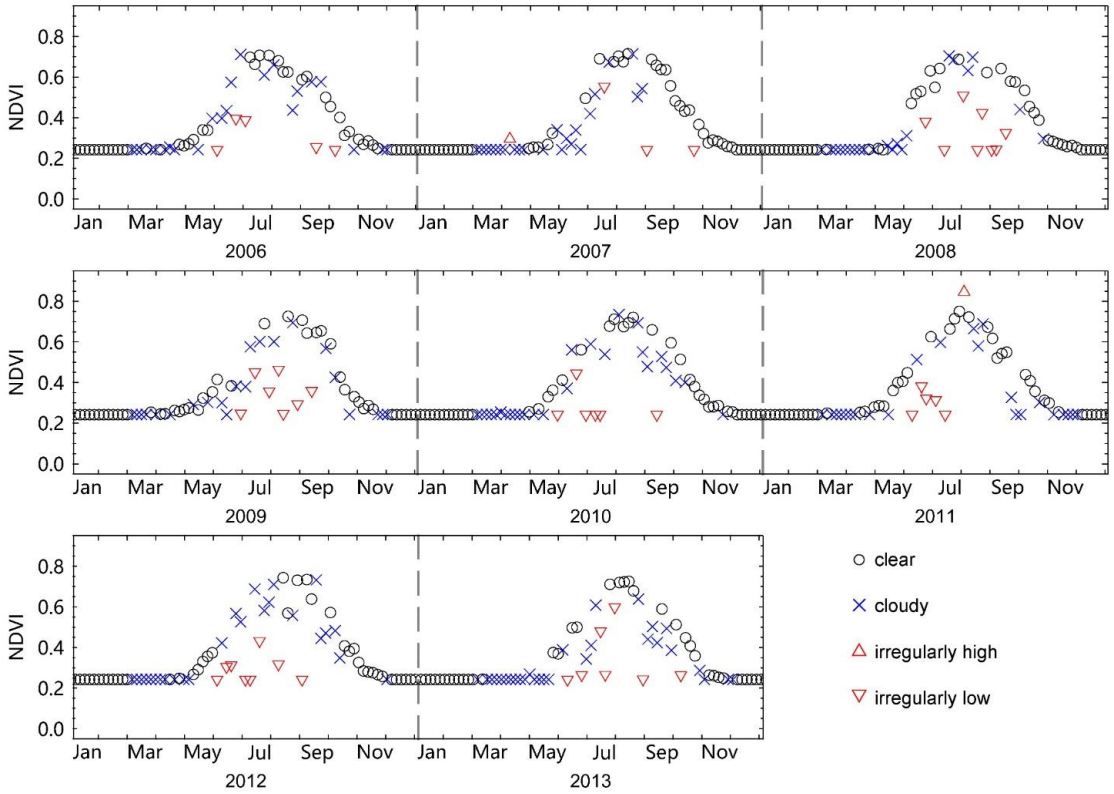

Figure SM3. An example showing irregularly high and low NDVI values identified in the 5-day composited NDVI time series.

6) Processing the NDVI values flagged as "cloudy". Because clouds are overestimated by the

cloud flag (Wilson, Parmentier, & Jetz, 2014), there were a considerable number of high NDVI values during March–November that were flagged as "cloudy" but that appeared to be reasonable in the seasonal NDVI profile. We detected these NDVI values and promoted their flags to be "uncertain" ("uncertain" indicates a quality higher than "cloudy" but lower than "clear", see Cao et al. (2018) for details). First, a pixel-year was excluded from our study if each of the NDVI values from May to September was either "cloudy" or "irregular". Second, for NDVI values lower than 90% of their annual range plus the background NDVI value, the NDVI at time *t*, *NDVI*(*t*), was flagged as "uncertain" if it satisfied the following,

$$NDVI(t) \geq \max\{NDVI(t-2), NDVI(t-1), NDVI(t), NDVI(t+1), NDVI(t+2)\},$$

where *NDVI*(*t*) had been flagged as "cloudy", and *NDVI*(*t*−2), *NDVI*(*t*−1), *NDVI*(*t*+1), and *NDVI*(*t*+2) had all been flagged as "cloudy" or "irregular".

Moreover,

$$NDVI(t) \geq 0.85 \times \max\{NDVI(t-12), NDVI(t-11), \ldots, NDVI(t-1)\}$$

for *NDVI*(*t*) in an ascending period (i.e., from early March to the time of annual maximum NDVI), and

$$NDVI(t) \geq 0.85 \times \max\{NDVI(t+1), NDVI(t+2), \ldots, NDVI(t+12)\}$$

for *NDVI*(*t*) in a descending period (i.e., from the time of annual maximum NDVI to late November). The figure SM4 gives an example of NDVI values that were promoted from "cloudy" to "uncertain".

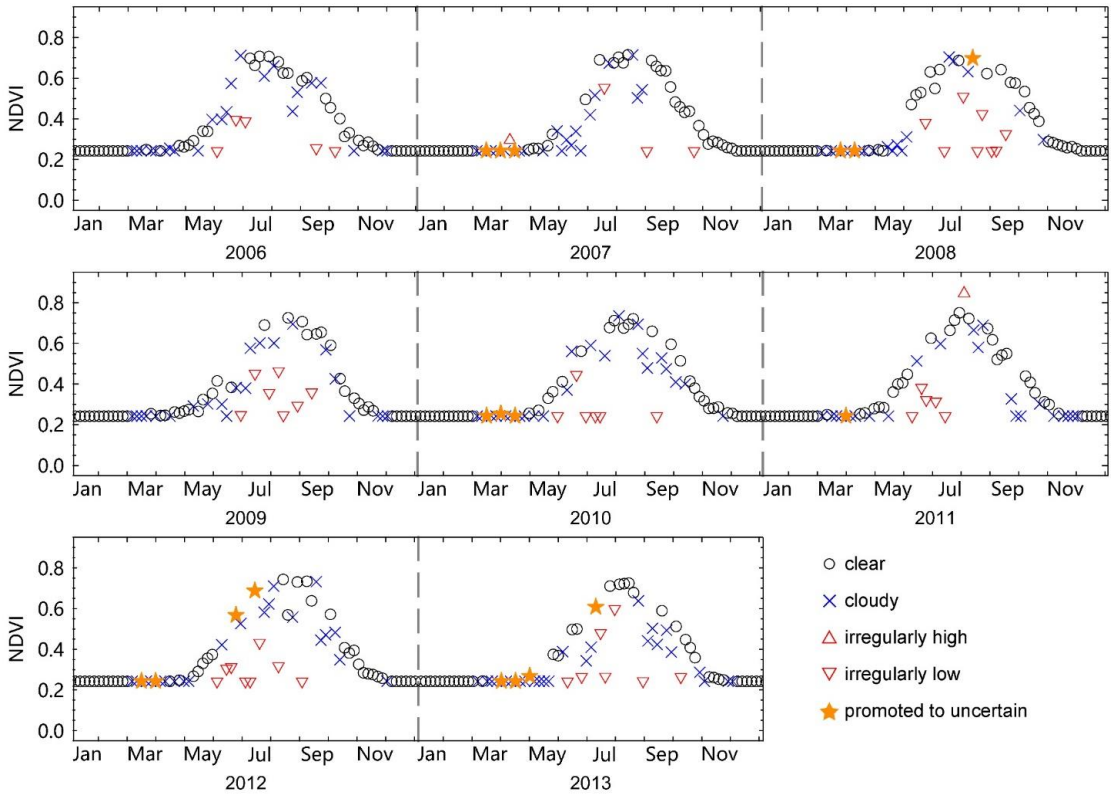

426

427 **Figure SM4.** An example showing NDVI values with flags promoted from "cloudy" to "uncertain".

428

429 7) Reconstructing 5-day continuous high-quality NDVI time series. Because clouds and poor
430 atmospheric conditions contaminate NDVI values, we applied a Savitzky-Golay filter to reconstruct a
431 high-quality NDVI time-series as described by Cao et al. (2018) and Shen et al. (2014). The source code
432 of Spatial-Temporal Savitzky-Golay (STSG) is available at https://github.com/cao-
433 sre/STSG_IDL_program (assessed on 19 December 2018). Before we applied the filter, the "irregular"
434 quality flags were merged to "cloudy". In our study, we used the same parameter setting as Cao et al.
435 (2018), except that the half width of the search window and the half width of the smoothing window
436 were both set to 5. The figure SM5 gives an example of the filtering.

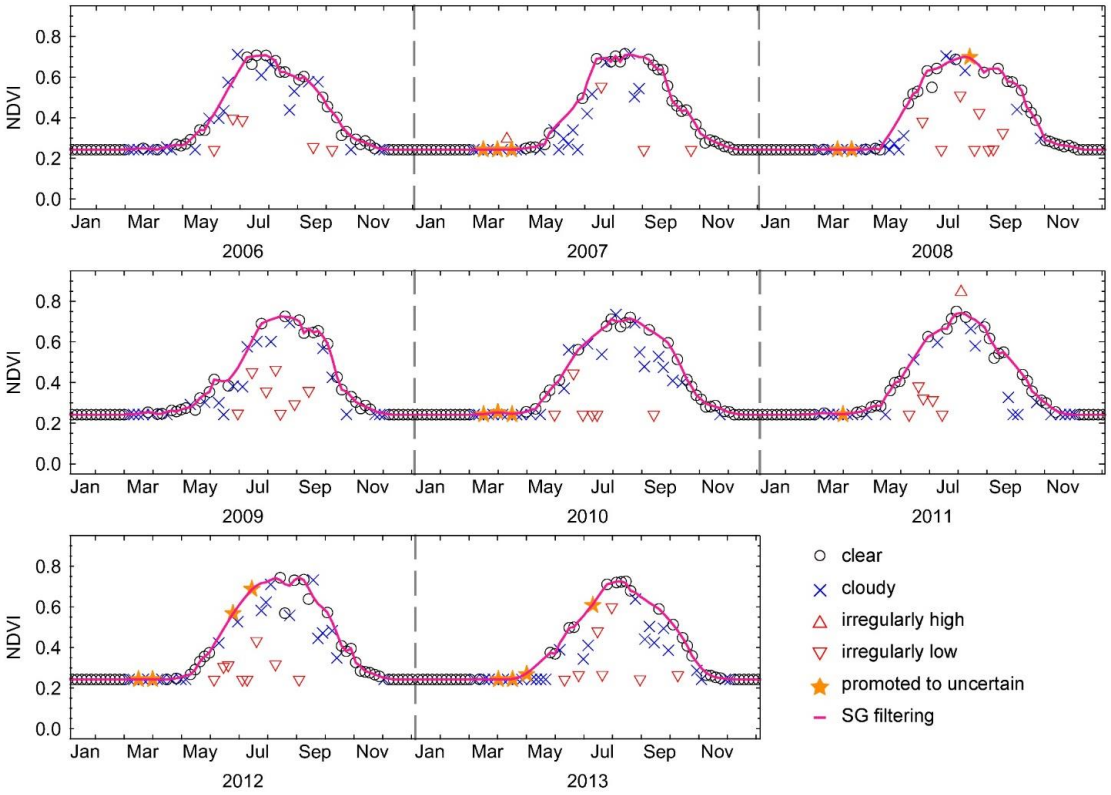

437

438 **Figure SM5.** An example showing the output of SG filtering.

439

440

441

2 Comparison between satellite D_{LCO} and D_{LCO} from PhenoCam dataset

To better match the PhenoCam images, we used the satellite MOD09A1 dataset (collection 6) which has a spatial resolution of 500 m and temporal resolution of 8 days. The dataset was downloaded from https://modis.ornl.gov/globalsubset/ on March 10, 2021. The PhenoCam dataset V2.0 was downloaded from https://daac.ornl.gov/cgi-bin/dsviewer.pl?ds_id=1674 on August 29, 2020. From the high-frequency (typically, 30 minute) imagery collected over several years, the GCC (green chromatic coordinate) time series of a region-of-interest (ROI) that delineates an area of specific vegetation type was provided by the PhenoCam dataset. The VCI (vegetation contrast index) time series was calculated as the ratio of the green to the sum of the red and blue bands (Zhang et al., 2018). For the comparison between satellite D_{LCO} and D_{LCO} from the PhenoCam dataset, processing steps are as follows:

Step 1, the sites for agricultural lands, urban areas, or heterogeneous landscape within the area of a 500 m × 500 m pixel were excluded by visually examining the images in Google Earth. Then, daily time series were created by calculating the 90th percentile of GCC or VCI for each day. After that, 5-day medium value filtering was used to smooth the short term fluctuations and noises.

Step 2, a time series was excluded if there was no data in any consecutive 30 days from annual maximum and to the end of year.

Step 3, the annual time series were fitted to a generalized sigmoid function (eq 7 in Klosterman et al (Klosterman et al., 2014)).

Step 4, in many of the sites, there was considerable mismatch between the annual NDVI and GCC (or VCI) trajectories. To remove some of those mismatched annual trajectories, we excluded the site-years for which the date of annual maximum NDVI differed by more than 30 days from that of GCC (or VCI) or the Pearson's correlation coefficient between NDVI and GCC (or VCI) lower than 0.75. In this step, the date of annual maximum NDVI (or GCC, VCI) was determined using 25-day smoothed times series of the fitted curves to eliminate short time variations. The Pearson's correlation coefficient was calculated between fitted daily NDVI and GCC (or VCI) for the period from the date of annual maximum greenness and the date when greenness dropped by 60%. The period for calculating correlation coefficient was determined using the earlier one of the dates of annual maximum NDVI and GCC (or VCI) and the later one of the dates when NDVI and GCC (or VCI) dropped by 60%. This criterion was not applied to deciduous broadleaf forest, because annual maximum of GCC or VCI usually occurred in late May or early June whereas annual maximum of NDVI was usually in late July or early August. After that, we excluded the annual NDVI time series for which the mean NDVI of the

31 days period with annual maximum NDVI in the 16th day was less than 1.15 times the mean NDVI of December.

The satellite D_{LCO} explained about 80% of the variations in PhenoCam derived D_{LCO} (Fig. 2 in the main text), although the mismatch between the annual NDVI and GCC trajectories leads to large D_{LCO} difference between NDVI and GCC (Figure SM6) or VCI (Figure SM7).

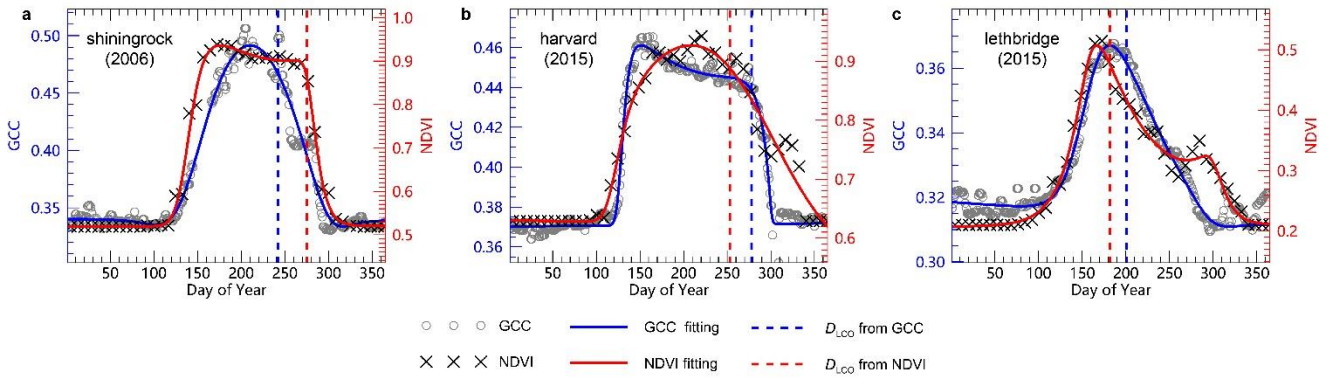

Figure SM6. Examples that mismatch between the annual NDVI and GCC trajectories leads to large D_{LCO} difference between NDVI and GCC.

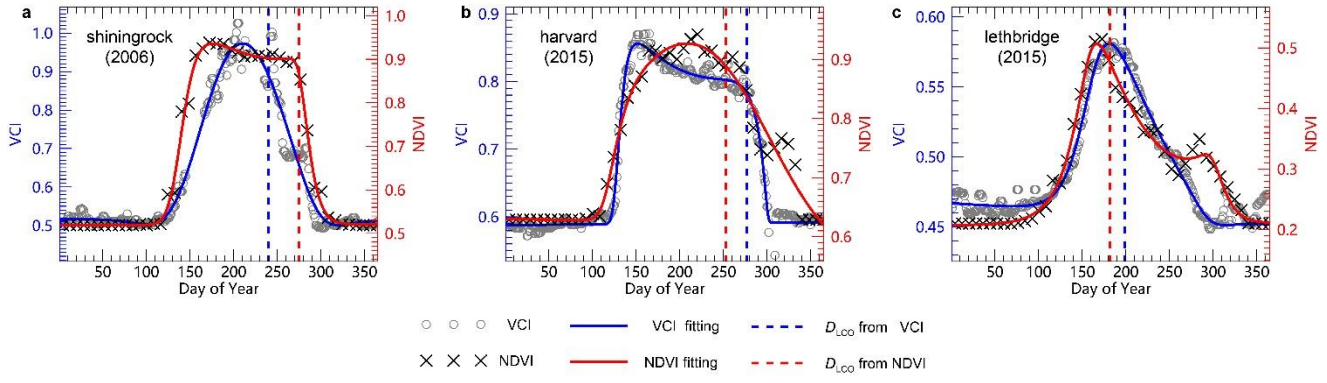

Figure SM7. Examples that mismatch between the annual NDVI and VCI trajectories leads to large D_{LCO} difference between NDVI and VCI.

Supplementary References

Aikio, S., Taulavuori, K., Hurskainen, S., Taulavuori, E., & Tuomi, J. (2019). Contributions of day length, temperature and individual variability on the rate and timing of leaf senescence in the common lilac Syringa vulgaris. *Tree Physiology, 39*(6), 961-970. doi:10.1093/treephys/tpz013

Amiro, B. (2016). FLUXNET2015 CA-Man Manitoba - Northern Old Black Spruce (former BOREAS Northern Study Area). In: FluxNet; University of Manitoba.

Arain, M. A. (2016a). FLUXNET2015 CA-TP3 Ontario - Turkey Point 1974 Plantation White Pine. In: FluxNet; McMaster University.

Arain, M. A. (2016b). FLUXNET2015 CA-TP4 Ontario - Turkey Point 1939 Plantation White Pine. In: FluxNet; McMaster University.

Aurela, M., Tuovinen, J.-P., Hatakka, J., Lohila, A., Mäkelä, T., Rainne, J., & Lauria, T. (2016). FLUXNET2015 FI-Sod Sodankyla. In: FluxNet; Finnish Meteorological Institute.

Beck, P. S. A., Atzberger, C., Høgda, K. A., Johansen, B., & Skidmore, A. K. (2006). Improved monitoring of vegetation dynamics at very high latitudes: A new method using MODIS NDVI. *Remote Sensing of Environment, 100*(3), 321-334. doi:10.1016/j.rse.2005.10.021

Bernhofer, C., Grünwald, T., Moderow, U., Hehn, M., Eichelmann, U., & Prasse, H. (2016a). FLUXNET2015 DE-Gri Grillenburg. In: FluxNet; TU Dresden.

Bernhofer, C., Grünwald, T., Moderow, U., Hehn, M., Eichelmann, U., & Prasse, H. (2016b). FLUXNET2015 DE-Tha Tharandt. In: FluxNet; TU Dresden.

Berveiller, D., Delpierre, N., Dufrêne, E., Pontailler, J.-Y., Vanbostal, L., Janvier, B., ... Cristinacce, K. (2016). FLUXNET2015 FR-Fon Fontainebleau-Barbeau. In: FluxNet; CNRS.

Black, T. A. (2016a). FLUXNET2015 CA-Oas Saskatchewan - Western Boreal, Mature Aspen. In: FluxNet; The University of British Columbia.

Black, T. A. (2016b). FLUXNET2015 CA-Obs Saskatchewan - Western Boreal, Mature Black Spruce. In: FluxNet; The University of British Columbia.

Blanken, P. (2016). FLUXNET2015 US-NR1 Niwot Ridge Forest (LTER NWT1). In: FluxNet; University of Colorado.

Böhlenius, H., Huang, T., Charbonnel-Campaa, L., Brunner, A. M., Jansson, S., Strauss, S. H., & Nilsson, O. (2006). CO/FT regulatory module controls timing of flowering and seasonal growth cessation in trees. *Science, 312*(5776), 1040-1043.

Cao, R., Chen, Y., Shen, M., Chen, J., Zhou, J., Wang, C., & Yang, W. (2018). A simple method to

519 improve the quality of NDVI time-series data by integrating spatiotemporal information with the
520 Savitzky-Golay filter. *Remote Sensing of Environment, 217*, 244-257.
521 doi:https://doi.org/10.1016/j.rse.2018.08.022
522 Chen, J. (2016). FLUXNET2015 US-Oho Oak Openings. In: FluxNet; University of Toledo / Michigan
523 State University.
524 Davidson, H. (1957). *Photoperiodic responses on selected woody ornamental shrubs.* Michigan State
525 University of Agriculture and Applied Science. Department of Horticulture,
526 De Ligne, A., Manise, T., Heinesch, B., Aubinet, M., & Vincke, C. (2016). FLUXNET2015 BE-Vie
527 Vielsalm. In: FluxNet; University of Liege - Gembloux Agro-Bio Tech; University catholic of
528 Louvain-la-Neuve.
529 Desai, A. (2016). FLUXNET2015 US-PFa Park Falls/WLEF. In: FluxNet; University of Wisconsin.
530 Dolman, H., Van Der Molen, M., Parmentier, F.-J., Marchesini, L. B., Dean, J., Van Huissteden, K., &
531 Maximov, T. (2016). FLUXNET2015 RU-Cok Chokurdakh. In: FluxNet; Vrije Universiteit
532 Amsterdam.
533 Downs, R. J., & Borthwick, H. A. (1956). Effects of photoperiod on growth of trees. *Botanical Gazette,*
534 *117*(4), 310-326.
535 Fennell, A., & Hoover, E. (1991). Photoperiod influences growth, bud dormancy, and cold acclimation
536 in Vitis labruscana and V. riparia. *Journal of the American Society for Horticultural Science.*
537 *American Society for Horticultural Science, 116*, 270-273. doi:10.21273/JASHS.116.2.270
538 Fracheboud, Y., Luquez, V., Björkén, L., Sjödin, A., Tuominen, H., & Jansson, S. (2009). The control of
539 autumn senescence in European aspen. *Plant Physiology, 149*(4), 1982-1991.
540 doi:10.1104/pp.108.133249
541 Gianelle, D., Cavagna, M., Zampedri, R., & Marcolla, B. (2016). FLUXNET2015 IT-MBo Monte
542 Bondone. In: FluxNet; Edmund Mach Foundation.
543 Gianelle, D., Zampedri, R., Cavagna, M., & Sottocornola, M. (2016). FLUXNET2015 IT-Lav Lavarone.
544 In: FluxNet; Edmund Mach Foundation.
545 Gough, C., Bohrer, G., & Curtis, P. (2016). FLUXNET2015 US-UMB Univ. of Mich. Biological
546 Station. In: FluxNet; Ohio State University; Virginia Commonwealth University.
547 Grubbs, F. E. (1950). Sample criteria for testing outlying observations. *Annals of Mathematical*
548 *Statistics, 21*(1), 27-58.
549 Hamilton, J. A., El, K. W., Hart, A. T., Runcie, D. E., Arango-Velez, A., & Cooke, J. E. (2016). The joint

influence of photoperiod and temperature during growth cessation and development of dormancy in white spruce (Picea glauca). *Tree Physiology, 36*(11), tpw061.

Heide, O. M. (1974). Growth and Dormancy in Norway Spruce Ecotypes (Picea abies) I. Interaction of Photoperiod and Temperature. *Physiologia Plantarum, 30*(1), 1-12. doi:10.1111/j.1399-3054.1974.tb04983.x

Heide, O. M. (2001). Photoperiodic control of dormancy in Sedum telephium and some other herbaceous perennial plants. *Physiologia Plantarum, 113*(3), 332-337.

Hörtnagl, L., Eugster, W., Buchmann, N., Paul-Limoges, E., Etzold, S., & Haeni, M. (2016). FLUXNET2015 CH-Lae Laegern. In: FluxNet; ETH Zurich.

Hörtnagl, L., Eugster, W., Merbold, L., Buchmann, N., Etzold, S., Haesler, R., & Haeni, M. (2016). FLUXNET2015 CH-Dav Davos. In: FluxNet; ETH Zurich.

Howe, G. T., Gardner GHackett, W. P., & Furnier, G. R. (1996). Phytochrome control of short-day-induced bud set in black cottonwood. *Physiologia Plantarum, 97*(1), 95-103.

Ibrom, A., & Pilegaard, K. (2016). FLUXNET2015 DK-Sor Soroe. In: FluxNet; Technical University of Denmark (DTU).

Janssens, I. (2016). FLUXNET2015 BE-Bra Brasschaat. In: FluxNet; University of Antwerp.

Junttila, O. (1980). Effect of photoperiod and temperature on apical growth cessation in two ecotypes of Salix and Betula. *Physiologia Plantarum, 48*(3), 347-352.

Keskitalo, J., Bergquist, G., Gardeström, P., & Jansson, S. (2005). A cellular timetable of autumn senescence. *Plant Physiol, 139*(4), 1635-1648. doi:10.1104/pp.105.066845

Klosterman, S. T., Hufkens, K., Gray, J. M., Melaas, E., Sonnentag, O., Lavine, I., ... Richardson, A. D. (2014). Evaluating remote sensing of deciduous forest phenology at multiple spatial scales using PhenoCam imagery. *Biogeosciences, 11*(16), 4305-4320. doi: https://doi.org/10.5194/bg-11-4305-2014

Knohl, A., Tiedemann, F., Kolle, O., Schulze, E.-D., Kutsch, W., Herbst, M., & Siebicke, L. (2016). FLUXNET2015 DE-Hai Hainich. In: FluxNet; University of Goettingen, Bioclimatology.

Kramer, P. J. (1936). Effect of variation in length of day on growth and dormancy of trees. *Plant Physiology, 11*(1), 127-137.

Law, B. (2016). FLUXNET2015 US-Me2 Metolius mature ponderosa pine. In: FluxNet; Oregon State University.

Lund, M., Jackowicz-Korczynski, M., & Abermann, J. (2016). FLUXNET2015 DK-ZaH Zackenberg

581 Heath. In: FluxNet; Aarhus University.
582 Mammarella, I., Vesala, T., Keronen, P., Kolari, P., Launiainen, S., Pumpanen, J., ... Pohja, T. (2016).
583 FLUXNET2015 FI-Hyy Hyytiala. In: FluxNet; University of Helsinki.
584 Massman, B. (2016). FLUXNET2015 US-GLE GLEES. In: FluxNet; USDA Forest Service.
585 Matteucci, G. (2016). FLUXNET2015 IT-Col Collelongo. In: FluxNet; Istituto di Ecologia e Idrologia
586 Forestale CNR.
587 McCaughey, H. (2016). FLUXNET2015 CA-Gro Ontario - Groundhog River, Boreal Mixedwood
588 Forest. In: FluxNet; Queen's University.
589 Minerbi, S., & Montagnani, L. (2016). FLUXNET2015 IT-Ren Renon. In: FluxNet; Autonomous
590 Province of Bolzano, Forest Services.
591 Misra, G., & Biswal, U. C. (1973). Factors Concerned in Leaf Senescence. I. Effects of Age, Chemicals,
592 Petiole, and Photoperiod on Senescence in Detached Leaves of Hibiscus rosa-sinensis L.
593 *Botanical Gazette, 134*(1), 5-11. doi:10.1086/336672
594 Moors, E., & Elbers, J. (2016). FLUXNET2015 NL-Loo Loobos. In: FluxNet; ALTERRA / Wageningen
595 Environmental Research.
596 Munger, J. W. (2016). FLUXNET2015 US-Ha1 Harvard Forest EMS Tower (HFR1). In: FluxNet;
597 Harvard University.
598 Novick, K., & Phillips, R. (2016). FLUXNET2015 US-MMS Morgan Monroe State Forest. In: FluxNet;
599 Indiana University.
600 Oleksyn, J., Tjoelker, M. G., & Reich, P. B. (1992). Growth and biomass partitioning of populations of
601 European Pinus sylvestris L. under simulated 50° and 60°N daylengths: evidence for
602 photoperiodic ecotypes. *New Phytologist, 120*(4), 561-574.
603 Olmsted, C. E. (1951). Experiments on Photoperiodism, Dormancy, and Leaf Age and Abscission in
604 Sugar Maple. *Botanical Gazette, 112*(4), 365-393.
605 Paus, E., Nilsen, J., & Junttila, O. (1986). Bud Dormancy and Vegetative Growth in Salix-Polaris as
606 Affected by Temperature and Photoperiod. *Polar Biology, 6*(2), 91-95.
607 Rinne, P., Saarelainen, A., & Junttila, O. (1994). Growth cessation and bud dormancy in relation to ABA
608 level in seedlings and coppice shoots of Betula pubescens as affected by a short photoperiod,
609 water stress and chilling. *Physiologia Plantarum, 90*(3), 451-458.
610 Scott, R. (2016a). FLUXNET2015 US-SRM Santa Rita Mesquite. In: FluxNet; United States
611 Department of Agriculture.

612 Scott, R. (2016b). FLUXNET2015 US-Wkg Walnut Gulch Kendall Grasslands. In: FluxNet; United
613 States Department of Agriculture.
614 Shen, M., Zhang, G., Cong, N., Wang, S., Kong, W., & Piao, S. (2014). Increasing altitudinal gradient of
615 spring vegetation phenology during the last decade on the Qinghai–Tibetan Plateau. *Agricultural*
616 *and Forest Meteorology, 189-190*, 71-80. doi:10.1016/j.agrformet.2014.01.003
617 Šigut, L., Havrankova, K., Jocher, G., Pavelka, M., & Janouš, D. (2016). FLUXNET2015 CZ-BK1 Bily
618 Kriz forest. In: FluxNet; Global Change Research Institute CAS.
619 Varlagin, A., Kurbatova, J., & Vygodskaya, N. (2016). FLUXNET2015 RU-Fyo Fyodorovskoye. In:
620 FluxNet; A.N. Severtsov Institute of Ecology and Evolution.
621 Vermote, E. F. (2015). MOD09CMG MODIS/Terra Surface Reflectance Daily L3 Global 0.05Deg CMG
622 V006. In *NASA EOSDIS Land Processes DAAC*.
623 Vermote, E. F., Roger, J. C., & Ray, J. P. (2015). MODIS Surface Reflectance User's Guide, Collection
624 6, Version 1.4. *MODIS Land Surface Reflectance Science Computing Facility*.
625 Wang, D. Y., Hu, S., Li, Q., Cui, K. M., & Zhu, Y. X. (2002). Photoperiod control of apical bud and leaf
626 senescence in pumpkin (Cucurbita pepo) strain 185. *Acta Botanica Sinica, 44*(1), 55-62.
627 Wilson, A. M., Parmentier, B., & Jetz, W. (2014). Systematic land cover bias in Collection 5 MODIS
628 cloud mask and derived products — A global overview. *Remote Sensing of Environment, 141*,
629 149-154. doi:https://doi.org/10.1016/j.rse.2013.10.025
630 Zhang, X. (2015). Reconstruction of a complete global time series of daily vegetation index trajectory
631 from long-term AVHRR data. *Remote Sensing of Environment, 156*, 457-472.
632 doi:10.1016/j.rse.2014.10.012
633 Zhang, X., Jayavelu, S., Liu, L., Friedl, M. A., Henebry, G. M., Liu, Y., ... Gray, J. (2018). Evaluation of
634 land surface phenology from VIIRS data using time series of PhenoCam imagery. *Agricultural*
635 *and Forest Meteorology, 256-257*, 137-149. doi:10.1016/j.agrformet.2018.03.003
636